CROSS-SECTIONS FOR TRANSIENT ANALYSES: DEVELOPMENT OF A GENETIC ALGORITHM FOR THE ENERGY MESHING

Zur Erlangung des akademischen Grades eines
DOKTORS DER INGENIEURWISSENSCHAFTEN (Dr.-Ing.)

bei der KIT-Fakultät für Maschinenbau des
Karlsruher Instituts für Technologie (KIT)
angenommene

DISSERTATION

von

Mattia Vincenzo Edoardo Massone

Tag der mündlichen Prüfung: 20. Februar 2018

Hauptreferent: Prof. Dr. Thomas Schulenberg
Korreferent: Prof. Dr. Piero Ravetto

ABSTRACT

The generation of multigroup cross-section libraries is a key point of multigroup transport calculations: a larger number of energy groups promotes the accuracy of the results, but hinders the time performance, which is a problem especially for 3D transient cases. Hence the need arises for multigroup deterministic transient calculations that, with a very limited amount of groups, can adequately represent the whole continuous energy space.

A new neutron cross-section collapsing tool has been implemented into the mechanistic codes SIMMER-III and SIMMER-IV, which introduces a cross-section condensation of the input multigroup libraries, which can then be provided with a finer structure than the one actually used by the transport solver. In this way the results are more accurate, as the nuclear data provided as input are closer to the original ones, but the computational time does not increase dramatically, as the transport solver will operate on a more limited number of energy groups.

A question, however, stays open: the determination of the energy discretization that best suits to the problem. This important issue, except for a few authors, has been considered mostly from the empirical point of view in the past, and required long tests to find out a reasonable energy structure, which is specific for the considered reactor and might be unsuitable for other systems.

This thesis proposes an automatic procedure, based on genetic algorithm optimization, aiming to choose the most appropriate energy structure for the considered system to collapse a fine multigroup library into a few-groups one. Such an innovative tool, used together with the cross-section condensation technique mentioned above, allows having specific libraries for each considered case, starting from a unique general library with fine energy discretization. The tests performed with different initial cross-section libraries and reactor systems show the strength of the technique in solving the energy meshing problem in many different conditions, returning structures which take into account the peculiar needs of each system. In addition, the analysis of the algorithm choices may reveal important information on neutron population physics, whose relevance during a manual cross-section library preparation can be easily underestimated. Tests show that the algorithm is able to find representative energy structures, providing accurate results on the multiplication factor, the reactivity feedback coefficients and the reaction rates. The results of each test are analysed, showing how different compositions, geometries and neutron spectra guide the algorithm choices and demonstrate the effectiveness of the method.

ZUSAMMENFASSUNG

Die Bereitstellung von Multigruppen-Wirkungsquerschnitts-Bibliotheken ist ein wesentlicher Schritt in Multigruppen-Neutronentransportrechnungen: eine größere Zahl von Energiegruppen verbessert die Genauigkeit der Ergebnisse, erhöht aber den Rechenaufwand deutlich. Dadurch wird die Durchführung deterministischer transienter Berechnungen erschwert, was sich insbesondere bei einer 3D-Modellierung der Reaktorgeometrie nachteilig auswirkt. Daraus ergibt sich für derartige Rechnungen die Notwendigkeit, die kontinuierliche Energieskala mit möglichst wenigen Energiegruppen zu repräsentieren.

Ein neuartiges Verfahren zur geeigneten Kondensation von Multigruppen-Wirkungsquerschnitten wurde in die mechanistischen Rechenprogramme SIMMER-III und SIMMER-IV implementiert, so dass in den auszuführenden Transportrechnungen eine geringere Auszahl von Gruppen benutzt werden kann, als die ursprünglichen Bibliotheken mit ihrer Feinstruktur der Energiegruppen enthalten. Damit sind genauere Ergebnisse zu erwarten, da die tatsächlich verwendeten Wirkungsquerschnitte eher den ursprünglichen nuklearen Daten entsprechen. Dies muß im Gegenzug nicht durch eine drastische Erhöhung der Rechenzeit erkauft werden, da der Löser der Transportgleichungen nur mit einer limitierten Anzahl von Energiegruppen belastet wird.

Bei diesem Verfahren hat die geschickte Auswahl der Grobgruppen-Strukur entscheidenden Einfluß auf die Qualität der Ergebnisse. In der Vergangenheit wurde die Auswahl in den meisten Fällen auf Basis empirischer Erfahrungswerte getroffen. Dies erforderte in der Regel umfangreiche Tests für den jeweils betrachteten Reaktortyp, wobei die spezifische Lösung nur eingeschränkt auf andere Systeme übertragen werden konnte.

In der vorliegenden Arbeit wird ein allgemeines Verfahren beschrieben, das für den jeweils betrachteten Anwendungsfall die bestmögliche Auswahl der Energiegruppen trifft, um später vorhandene Feingruppen-Bibliotheken in eine geeignete Grobstruktur zu überführen. Die Auswahl der Gruppen erfolgt automatisiert durch einen genetischen Optimierungs-Algorithmus. Mit diesem innovativen Verfahren lassen sich verfügbare allgemeine Feingruppen-Bibliotheken zu anwendungsspezifischen Grobstruktur-Wirkungsquerschnitten kondensieren. Durchgeführte Tests für unterschiedliche Reaktortypen und mit verschiedenen Feingruppen-Bibliotheken erbrachten den Nachweis der zuverlässigen Anwendbarkeit der entwickelten Methode, die

unter Berücksichtigung der Eigenheiten der betrachteten Anwendungsfälle geeignete Strukturen lieferte. Darüberhinaus gestattet das Verfahren zusätzliche Einblicke in das neutronische Verhalten des Reaktors, die bei der üblichen manuellen Vorgehensweise leicht übersehen werden können. Die Tests zeigen, dass der implementierte Algorithmus repräsentative Energiegruppen-Strukturen bereitstellt, die zuverlässige Ergebnisse für Reaktor-Kenngrößen wie Multiplikationsfaktor, Reaktivitäts-Rückwirkungs-Koeffizienten und Reaktionsraten liefern. Aus der Analyse der Testergebnisse geht hervor, wie unterschiedliche Reaktorparameter, wie Geometrie, Materialzusammensetzung und das daraus resultierende Neutronenspektrum, den Algorithmus bei der bestmöglichen Wahl der Energiestruktur steuern. Damit wird die Effektivität der entwickelten Methode nachdrücklich demonstriert.

ACKNOWLEDGEMENTS

Countless amazing people have helped me in achieving such an big accomplishment and they all share with me the merit for the success of this work. With its end, it is time to express my greatest gratitude to all those people, because without them none of this would have been possible.

My first thank goes to my supervisor Prof. Thomas Schulenberg for accepting me as his student, as without his availability this work would have never been finished. Since my arrival at KIT he has been a true mentor and always provided complete support in all my activities; with his wise advice he left indeed his mark on this thesis and on me.

There is no appropriate word to thank enough my second supervisor Prof. Piero Ravetto: my inspiration and counsellor since the first time I have met him, I treasure each conversation I had with him. He has been and is still my *rabbi*.

Special thanks go to the head of the TRANS group Dr. Andrei Rineiski: he granted me his confidence by welcoming me in his group and has constantly supported my studies. With his brilliant mind, he has always stimulated me with insightful and intriguing suggestions.

I cannot forget the precious advice by Dr. Werner Maschek: he exhorted me investigating the topic of this thesis when it was just an exotic idea; without his encouragement and full trust in me, the genetic algorithm would have never come to life.

I wish to offer a particular acknowledgement to Dr. Fabrizio Gabrielli, real friend and counsellor; with his patience, competence and unshakable enthusiasm, he has been the light in any setback: my guardian angel since my arrival in Karlsuhe, he can truly be considered the godfather of this work.

Dr. Edgar Kiefhaber deserves an important thank for his constant presence and rigorous revision work. He is a true fount of knowledge and an exemplar model to all scientists for his patience with the novices, passion in investigation and unrivalled experience.

My gratefulness goes also to each and every colleague, past and present, of the TRANS group: Simone, Barbara, Lena, Marco, Claudia, Rui, Max, Michael, Shisheng, Vladimir, Xue-Nong, Aleksandra, Eva, Liancheng. Thank you all for the good friendship, caring presence, valuable discussions, precious help, essential support, inspiring passion, radiant influence on my mood.

To all my friends, who for my luck are too many to be listed here: even though they are in Torino, Karlsruhe, Ortona, Ulm, Bilbao, Milano, Düsseldorf, Rome, München, Madrid, somewhere around the world, they are and have been always by my side. Each one of them deserves a special and personal thank: they are my light in the dark and my joy in the good times.

In the end, but not by importance, I wish to express my immense gratitude to my dear family for their constant support, invaluable example and unconditional love: thank you Dad, lodestar of my life; thank you Mum, safe harbour of refuge; thank you Sister, trusted companion of my journey, best gift I could receive from our parents. This work is dedicated to the three of you.

To all of you, including those who have not been named explicitly due to space limitations, whose help however shall not be forgotten, my greatest thank: you coming into my life has been a wonderful luck and the greatest blessing.

TABLE OF CONTENTS

ABBREVIATIONS

ASTRID ..... ADVANCED SODIUM TECHNOLOGICAL REACTOR FOR INDUSTRIAL DEMONSTRATION

CEA..... COMMISSARIAT À L'ÉNERGIE ATOMIQUE ET AUX ÉNERGIES ALTERNATIVES

CR ..... CONTROL ROD

ECCO ..... EUROPEAN CELL CODE

ESFR ..... EUROPEAN SODIUM FAST REACTOR

ESNII+..... EUROPEAN SUSTAINABLE NUCLEAR INDUSTRIAL INITIATIVE

GA ..... GENETIC ALGORITHM

KIT ..... KARLSRUHE INSTITUTE OF TECHNOLOGY

METIS ..... METAHEURISTIC ENERGY TIERS SEARCH

MSFR ..... MOLTEN SALT FAST REACTOR

SFR ..... SODIUM-COOLED FAST REACTOR

WH ..... WORKING HORSE

XS ..... CROSS-SECTION

SYMBOLS

$\boldsymbol{A}$	→	Absorption matrix
$\boldsymbol{L}$	→	Leakage matrix
$\boldsymbol{S}$	→	Fission source matrix
B^2	→	Buckling
C	→	Chromosome
C_G	→	G-th element of the chromosome C
D	→	Diffusion coefficient
E	→	Energy variable
E_g	→	Upper energy boundary of group g
F	→	Set of all legal chromosomes
FG	→	Number of groups in the few-groups library
F_V	→	Void feedback coefficient
$f_{\mathrm{k}}^{(I)}$	→	Fitness of individual I based on multiplication factor
$f_{\boldsymbol{\Phi}}^{(I)}$	→	Fitness of individual I based on flux vectors
$f_{\mathrm{comb}}^{(I)}$	→	Fitness of individual I based on combined formula
$f_n(\boldsymbol{r}, E' \to E)$	→	n-th moment of the scattering function
$f_{\mathrm{s}}(\boldsymbol{r}, E' \to E, \widehat{\boldsymbol{\Omega}}' \to \widehat{\boldsymbol{\Omega}})$	→	Scattering function
$f_{\mathrm{s}}(\boldsymbol{r}, E' \to E)$	→	Scattering function integrated over direction
h_n	→	n-th moment of the fission emission function
K_D	→	Doppler feedback coefficient
$\boldsymbol{J}(\boldsymbol{r}, E)$	→	Neutron current
$\boldsymbol{j}(\boldsymbol{r}, E, t)$	→	Direction component of the neutron current

k	→	Multiplication factor (direct eigenvalue)
$k^{\dagger}$	→	Adjoint eigenvalue
I	→	Generic individual
MG	→	Number of groups in the fine-groups library
m_{n}	→	Neutron mass
N_{T}	→	Number of tournaments in the tournament selection
$\mathrm{P}_n(x)$	→	n-th order Legendre polynomial
$P^{(G)}$	→	Population size at generation G
p	→	Probability parameter of the tournament selection
$R^{(I)}$	→	Ranking of individual I in the tournament selection
RR_x	→	Reaction rate of type x
$RR_{x,\boldsymbol{\Omega}}$	→	Reaction rate of type x with directional dependence
r	→	Proliferation rate
$\boldsymbol{r}$	→	Position vector
$S(\boldsymbol{r}, E, \widehat{\boldsymbol{\Omega}}, t)$	→	Source term
t	→	Time dependence
$\mathbf{u_x}, \mathbf{u_y}, \mathbf{u_z}$	→	Axes direction of a Cartesian coordinate system
$v(E)$	→	Neutron velocity
$\mathrm{Y}_n^{\beta}(\widehat{\boldsymbol{\Omega}})$	→	Spherical harmonic function of degree n and order β
$\Gamma(\boldsymbol{r}, E, t)$	→	Energy component of the neutron current
δ_{nm}	→	Kronecker delta function
$\zeta(\widehat{\boldsymbol{\Omega}})$	→	Directional component of the neutron flux
η, ϑ	→	Azimuthal and polar angles in a spherical coordinate system
μ	→	Cosine of the polar angle in a spherical coordinate system
μ_0	→	Cosine of the scattering angle
$\nu(\boldsymbol{r}, E)$	→	Average number of neutrons produced per fission

$\Xi_{I,c}$	→	Cosine of the angle between two group fluxes vectors
Σ	→	Macroscopic cross-section
$\Phi(\boldsymbol{r}, E, t)$	→	Scalar flux
$\phi(\boldsymbol{r})$	→	Space component of the neutron scalar flux
$\varphi(\boldsymbol{r}, E, \widehat{\boldsymbol{\Omega}}, t)$	→	Neutron angular flux
$\chi(\boldsymbol{r}, E)$	→	Fission spectrum
$\psi(E)$	→	Energy component of the scalar flux
$\tilde{\psi}(E)$	→	$\psi(E)$ normalized over fission source
$\widehat{\boldsymbol{\Omega}}$	→	Direction unit vector
$*^{(G)}$	→	Broad energy group g
$*^{(g)}$	→	Fine energy group g
$*_{\mathrm{a}}$	→	Absorption
$*_{\mathrm{f}}$	→	Fission
$*_{\mathrm{obj}}$	→	Objective value
$*_{\mathrm{s}}$	→	Scattering
$*_{\mathrm{t}}$	→	Total
$*_{\mathrm{tr}}$	→	Transport
$\forall g \in G$	→	All fine groups g within the energy interval of the broad group G

CHAPTER 1. INTRODUCTION

Accuracy and reliability of safety studies in the nuclear technology field is a growing need. The availability of codes coupling neutronics and thermal-hydraulics is very important: reactivity effects and feedback coefficients play a relevant role in neutron balance and so it is essential describing the correct relation between the different physics of the reactor. For some configurations, also, 2D representations could be insufficient and should be progressively substituted with 3D simulations.

Neutronics solver methods in transient coupled codes are usually of the deterministic type. In fact, although the stochastic Monte Carlo methods are able to provide highly reliable results, they usually require very high computational power (and therefore long calculation time), making them an inefficient choice when the core status has to be recomputed frequently. Hence, they are considered the reference for validation of deterministic codes, which are the preferred choice for transient calculations. The latter, on the contrary, are able to return results much faster, but with lower accuracy. The calculation paradigm is different: rather than testing the system to find a neutron distribution satisfying the problem equations, a deterministic code calculates the solution of particular approximations of the neutron transport equation; each of these approximations is characterized by different methods for discretizing the space, time, angle and energy dimensions and/or by the truncation of the solution expansions into function sets.

A very common approximation is the discretization of the energy space, assuming that all quantities (neutron flux, current, fission spectrum, cross-sections…) which are continuous in the energy space can be described by their average values on fixed energy domains, called energy groups: with this hypothesis, one obtains the multigroup neutron transport equation (Duderstadt and Hamilton, 1976; Stacey, 2001, pp. 106–112). This approximation is not required in stochastic codes, which can use directly the continuous nuclear data (with some limitations due to temperature dependence), or very fine-groups libraries.

In deterministic codes, hence, nuclear data pre-processing becomes a critical point of the procedure: the number of groups used for the calculation is in direct relation with the accuracy of the cross-section (XS) description, and so of the results. Nevertheless, a larger number of energy groups correspond to bigger XS libraries, larger amount of computer memory and longer

computational time, which is a problem especially when the number of spatial meshes is very high, as in 3D cases. Hence the need arises for multigroup deterministic transient calculations that, with a very limited amount of groups, can adequately represent the whole continuous energy space.

Good results can be obtained if the XS condensation is performed "on-the-run", i.e. based on the real conditions of the system; this allows having more precise estimates of the neutron flux and current, and so of the reaction rates, which must be kept constant during the condensation process not to alter the results. With this in mind, I implemented a new XS collapsing tool into the transient analysis coupled code SIMMER (Bohl and Luck, 1990; Kondo et al., 2000; Tobita et al., 2002; Yamano et al., 2008; Yamano et al., 2003). This introduces a XS condensation of the input multigroup libraries, which can then be provided with a finer structure than the one actually used by the transport solver. In this way the precision can be increased, as the nuclear data provided as input are closer to the original ones (less deteriorated), but the computational time does not increase dramatically, as the transport solver will operate on a much more limited number of energy groups. In other words, part of the condensation procedure is moved inside SIMMER, where it can be performed in a more precise way, as the composition and the geometry of the system is known (Massone et al., 2014).

A question, however, stays open: the determination of the energy discretization, or energy structure, that best suits to the problem. This represents a very difficult issue, but crucial: if the structure is inadequate in describing the fate of neutrons, i.e. their movement along the energy spectrum (scattering, fission, absorption), results can be significantly different from the real behavior. The corollary is that, as the neutronic behavior depends mainly on geometry and composition, the energy meshing is specific of the problem and, in general, it should not be used with systems for which it has not been conceived. Instead, a limited number of groups can be sufficient for a reliable reactor modeling, provided that the energy structure is adequately chosen.

Unfortunately, such an important choice is often delegated to the user, who does not always have the specific competences in reactor physics and XS theory required to make a correct assessment. The procedure to generate a plausible energy structure (Bell and Glasstone, 1970, p. 181; Duderstadt and Hamilton, 1976, pp. 368–369; Knott and Yamamoto, 2010, pp. 943–944) is also somehow indefinite, leaving space for subjective decisions and common sense; one should then compensate the indetermination with additional tests and benchmarks, making the XS library generation a laborious process. One could also rely on expert judgement (Knott and Yamamoto, 2010, pp. 943–952) for a good structure, but this adds even more subjective

opinions to the choice. The difficulty of the work then encourages the use of few-groups XS libraries designed to be nonspecific to the systems, a practice that, on the contrary, should be avoided as it can easily lead to mistakes or unreliable results.

The current work aims to address these problems, proposing a standard procedure for the energy structure determination accessible to all users; such an innovative tool, used together with the previously described XS collapsing tool, would allow having specific libraries for each considered case, starting from a unique general library with fine energy discretization (Massone et al., 2017a). Releasing the user from the responsibility of choosing the energy structure would also limit the need for discretionary decisions and reduce the chance of human errors affecting the calculations.

Nevertheless, the nature of the problem, which is strongly non-linear, makes particularly difficult the definition of a deterministic algorithm. This issue suggests employing different optimization schemes, requiring few assumptions on the solution space, such as a metaheuristic (Bianchi et al., 2009; Voß, 2001). A metaheuristic is, according to Osman and Laporte (1996), "an iterative generation process which guides a subordinate heuristic by combining intelligently different concepts for exploring and exploiting the search space, learning strategies are used to structure information in order to find efficiently near-optimal solutions". In this sense it perfectly reflects its name, which is composed by the Greek word εὑρίσκω (*heurisko*, to find) with the prefix μετά- (*meta-*, beyond, in an upper level) (Blum and Roli, 2003).

Among the metaheuristics class, I selected a population-based, naturally-inspired, evolution-driven procedure for the energy structure problem: the genetic algorithm (GA). In essence, this is a simulation of the evolution process guided by natural selection in a population composed by individuals, each one representative of a point in the solution space. Based on the natural selection theory, effective solutions are able to pass down their positive features which, recombined through simple genetic operators, lead, generation after generation, to better individuals, i.e. better energy meshing options. The formulation of this optimization technique, which is nowadays employed in many different fields, is mainly due to Holland (1975), but is based on the work on evolutionary systems due to many different authors in the previous two decades.

Similar studies approaching the energy meshing problem with metaheuristic optimization have been carried on in the past by Mosca et al. (Mosca et al., 2011a; Mosca et al., 2011b; Mosca, 2009; Mosca and Mounier, 2008) and by Yi and Sjoden (Yi and Sjoden, 2013). All these works have in common the use of the Particle Swarm Optimization algorithms, while different ones are the test cases, ranging from infinite homogeneous medium problems to single pin models, in fast and

thermal systems. Nevertheless, in all these cases the focus has been set on the optimization of the library meshing for pins or sets of cells. On the contrary, the current work aims to find the energy structure associated to whole reactor systems: in other words, the objective is the best compromise on the needs of all cells composing the system at the same time. In fact, a reactor system is not a simple database of cells, but a set of elements (the cells indeed) correlated and interacting with each other based on their characteristics and their spatial position. The algorithm proposed in this dissertation does consider this point: the suggested energy meshing, hence, is optimal for the input system, but not for the single cells composing it.

The tool delineated above, which looks for a suitable energy mesh for neutron transport problems using a GA optimization, is described in this work and developed for the transient coupled codes SIMMER-III (Kondo et al., 2000; Yamano et al., 2003) and SIMMER-IV (Yamano et al., 2008), reference tools for accidental transient analyses. The tests I performed with different initial XS libraries and reactor systems show the strength of the technique in solving the energy meshing problem in many different conditions, returning structures which take into account the peculiar needs of each system. In addition, the analysis of the GA choices may reveal important information on neutron population physics, whose relevance during a manual XS library preparation can be easily ignored and underestimated.

The Chapter 2 provides a short summary to the most important concepts employed in this work, along with an introduction to the SIMMER code and the state of the art regarding the energy meshing problem. Chapter 3 introduces the new SIMMER tool for XS collapsing and describes the steps that led me to the development of the GA; the latter is then described in detail, along with its features and to the choices that resulted in the current code. The results of the verification tests on different reactors systems and configurations, demonstrating that the algorithm is actually able to solve the energy structure problem, are shown in Chapter 4. Chapter 5 offers an application of the GA to the 3D transient simulation of the Phénix reactor, hence illustrating how an actual case can be now tackled with a detailed XS library in reasonable computational time and with better results compared with naïve energy structure choices. Finally Chapter 6 summarizes the conclusions and perspectives of the work.

CHAPTER 2. STATE OF THE ART

Most deterministic codes, including SIMMER, adopt the multigroup theory, which requires that the continuous energy space is divided into discrete intervals, denoted as groups, to be described. Equivalent multigroup cross-section libraries are defined to keep constant the neutron balance before and after the discretization. In order to adequately describe the reactor physics, and therefore obtain reliable results, an important step is the definition of the energy structure, i.e. the energy discretization. Despite the relevance, such choice, which must be tailored on the studied system, is still usually based on expert judgement and on criteria which are somehow arbitrary.

This chapter describes the background of the work, introducing the reader into the cross-section and the transport multigroup theory. The energy structure problem, which this thesis focuses on, is then presented, along with the strategies commonly adopted in literature. Finally, the SIMMER code, which is widely used during the thesis work, is introduced.

2.1 CROSS-SECTION TREATMENT

The neutron XSs are among the most important basic input data required for any neutronics analysis: the data, which are the results of a delicate balance of theoretical modelling and experimental benchmark (Bell and Glasstone, 1970, pp. 199–200), contain the information regarding the way neutrons interact with matter. More precisely, the XSs define the probability that a given type of interaction (fission, absorption, scattering…) has of occurring once a collision between a neutron and a certain isotope has happened, depending on the neutron energy. XS data may also include additional information: angular dependencies, number and energy of neutrons produced by fission…

The starting point is usually constituted by the continuous data for the isotopes composing the system. The accuracy of the data is different depending on the databases in use and on the considered isotope: more studies are usually devoted to substances which are more often encountered in applications (e.g. common structural, fuel or coolant materials), which therefore benefit of a better accuracy. Some of the most known general purpose nuclear data files are: ENDF/B, released by the U.S. Cross Section Evaluation Working Group (Chadwick et al., 2006); JEFF, developed by the Nuclear Energy Agency (Koning et al., 2006); JENDL, under responsibility

of the Japanese Atomic Energy Agency (Shibata et al., 2011). Once defined, the nuclear data are processed differently depending on the adopted solution method: stochastic or deterministic.

Stochastic (or Monte Carlo) methods rather than solving the equation describing the neutron distribution, i.e. the neutron transport equation, simulate the random walk of a very large number of particles; the result is based on the statistics of the simulated walks. As one knows precisely position and energy (along with direction) at each moment of the particle random walk, one can access directly the XS tables and obtain the interaction probability with each isotope at the correct energy: whether an interaction is occurring (and which one) or not then depends just on random sampling. Hence the continuous XS data can be directly used with little pre-processing.

On the contrary, with deterministic methods the particles parameters are not known exactly: the parameters (position, direction, energy and time) space is discretized and the neutron population is described in terms of number of neutrons with the same parameter configuration. From the XS point of view, this means that different XS values can be associated to a single (average) energy value. Hence, an averaging of the XS is also required, which constitute the basis of the so called “multigroup approximation”, explained in detail in the next section.

The averaging procedure is not easy to be performed as it requires knowing in advance the neutron flux distribution (i.e. the problem solution). In particular, one has to take into account the effect each isotope has on the neutron flux distribution, and so on the equivalent XS of all other isotopes: when in a specific energy interval one particular isotope has a resonance peak, the neutron flux is depressed in correspondence to the peak, lowering the weight of all XSs in the vicinity, including its own ones. This procedure is called resonance self-shielding (Knott and Yamamoto, 2010, pp. 972–973; Waltar and Reynolds, 1981, pp. 142–154) and different methods are in use to introduce such correction: SIMMER, in particular employs the Bondarenko method (Bondarenko, 1964; Kidman et al., 1972); a more advanced alternative, used in the European Cell Code (ECCO) (Rimpault, 1995; Rimpault and Grimstone, 1987), is the subgroup method (Knott and Yamamoto, 2010, pp. 1035–1046).

Further corrections to the averaging procedure are sometimes introduced to take into account the effects of heterogeneity. In fact, if the cell is not homogeneous, the flux experienced by each material could depend on the actual position of the component within the cell (as in Figure 2.1), and this should be considered when weighting the XS effects. Such effects are usually more relevant in thermal systems than in fast ones (Waltar and Reynolds, 1981, pp. 172–175).

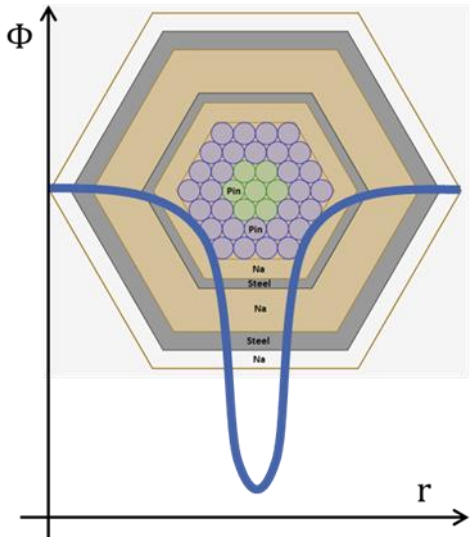

Figure 2.1: Example of heterogeneity effect on a control rod. Due to the absorption in the surrounding pins (in blue), the flux and so the effect of the central pins (in green) is lower, though the composition is the same.

2.2 MULTIGROUP TRANSPORT THEORY

As already mentioned, deterministic neutron transport solvers are based on the multigroup theory. The energy space is hence discretized in several energy ranges, denoted as energy groups; in each of these domains one assumes that XSs Σ and neutron fluxes φ can be approximated with their average value. Conventionally, the groups are numbered from the highest to the lowest energy.

The multigroup equation is derived from the neutron transport theory by defining the group neutron flux $\varphi^{(g)}$ as

$$\varphi^{(g)}(\boldsymbol{r},\hat{\boldsymbol{\Omega}},t) \triangleq \int_{E_{g-1}}^{E_g} \varphi(\boldsymbol{r},E,\hat{\boldsymbol{\Omega}},t)\,\mathrm{d}E \tag{2.1}$$

and the group scalar flux $\Phi^{(g)}$ as

$$\Phi^{(g)}(\boldsymbol{r},t) \triangleq \int_{E_{g-1}}^{E_g} \oint \varphi(\boldsymbol{r},E,\hat{\boldsymbol{\Omega}},t)\,\mathrm{d}\hat{\boldsymbol{\Omega}}\,\mathrm{d}E = \int_{E_{g-1}}^{E_g} \Phi(\boldsymbol{r},E,t)\,\mathrm{d}E = \oint \varphi^{(g)}(\boldsymbol{r},\hat{\boldsymbol{\Omega}},t)\,\mathrm{d}\hat{\boldsymbol{\Omega}}, \tag{2.2}$$

where E_g and E_{g-1} are the upper and lower energy boundaries of group g, respectively.

The multigroup XSs $\Sigma^{(g)}$ are defined starting from the transport equation, such that the reaction rates RR are preserved

$$RR_{x,\widehat{\boldsymbol{\Omega}}}^{(g)}\left(\boldsymbol{r},\widehat{\boldsymbol{\Omega}},t\right) \triangleq \int_{E_{g-1}}^{E_g} \Sigma_x(\boldsymbol{r},E)\varphi\left(\boldsymbol{r},E,\widehat{\boldsymbol{\Omega}},t\right)\mathrm{d}E = \Sigma_x^{(g)}\left(\boldsymbol{r},\widehat{\boldsymbol{\Omega}},t\right)\varphi^{(g)}\left(\boldsymbol{r},\widehat{\boldsymbol{\Omega}},t\right) \tag{2.3}$$

which, combined with eq. (2.2) gives

$$\Sigma_x^{(g)}\left(\boldsymbol{r},\widehat{\boldsymbol{\Omega}},t\right) = \frac{\int_{E_{g-1}}^{E_g} \Sigma_x(\boldsymbol{r},E)\varphi\left(\boldsymbol{r},E,\widehat{\boldsymbol{\Omega}},t\right)\mathrm{d}E}{\int_{E_{g-1}}^{E_g} \varphi\left(\boldsymbol{r},E,\widehat{\boldsymbol{\Omega}},t\right)\mathrm{d}E}. \tag{2.4}$$

Hence, from the transport equation (Duderstadt and Hamilton, 1976, p. 114)

$$\begin{aligned}\frac{1}{v(E)}\frac{\partial\varphi\left(\boldsymbol{r},E,\widehat{\boldsymbol{\Omega}},t\right)}{\partial t} + \widehat{\boldsymbol{\Omega}}\cdot\boldsymbol{\nabla}\varphi\left(\boldsymbol{r},E,\widehat{\boldsymbol{\Omega}},t\right) + \Sigma_{\mathrm{t}}(\boldsymbol{r},E)\varphi\left(\boldsymbol{r},E,\widehat{\boldsymbol{\Omega}},t\right) = \\ = \oint \mathrm{d}\widehat{\boldsymbol{\Omega}}' \int_0^{+\infty} \Sigma_{\mathrm{s}}(\boldsymbol{r},E')\varphi\left(\boldsymbol{r},E',\widehat{\boldsymbol{\Omega}}',t\right) f_{\mathrm{s}}\left(\boldsymbol{r},E'\to E,\widehat{\boldsymbol{\Omega}}'\to\widehat{\boldsymbol{\Omega}}\right)\mathrm{d}E' + \\ + \frac{\chi(\boldsymbol{r},E)}{4\pi}\oint\int_0^{+\infty} \nu(\boldsymbol{r},E')\Sigma_{\mathrm{f}}(\boldsymbol{r},E')\varphi\left(\boldsymbol{r},E',\widehat{\boldsymbol{\Omega}}',t\right)\mathrm{d}E'\,\mathrm{d}\widehat{\boldsymbol{\Omega}}' \\ + S\left(\boldsymbol{r},E,\widehat{\boldsymbol{\Omega}},t\right)\end{aligned} \tag{2.5}$$

one derives with eq. (2.2) and (2.3) the multigroup transport equation by integrating over the energy space

$$\begin{aligned}\frac{1}{v^{(g)}\left(\boldsymbol{r},\widehat{\boldsymbol{\Omega}},t\right)}\frac{\partial\varphi^{(g)}\left(\boldsymbol{r},\widehat{\boldsymbol{\Omega}},t\right)}{\partial t} + \widehat{\boldsymbol{\Omega}}\cdot\boldsymbol{\nabla}\varphi^{(g)}\left(\boldsymbol{r},\widehat{\boldsymbol{\Omega}},t\right) + \Sigma_{\mathrm{t}}^{(g)}\left(\boldsymbol{r},\widehat{\boldsymbol{\Omega}},t\right)\varphi^{(g)}\left(\boldsymbol{r},\widehat{\boldsymbol{\Omega}},t\right) = \\ = \oint \sum_{g'} \Sigma_{\mathrm{s}}^{(g'\to g)}\left(\boldsymbol{r},\widehat{\boldsymbol{\Omega}}'\to\widehat{\boldsymbol{\Omega}},t\right)\varphi^{(g')}\left(\boldsymbol{r},\widehat{\boldsymbol{\Omega}}',t\right)\mathrm{d}\widehat{\boldsymbol{\Omega}}' + \\ + \frac{\chi^{(g)}(\boldsymbol{r})}{4\pi}\oint\sum_{g'} \nu\Sigma_{\mathrm{f}}^{(g')}\left(\boldsymbol{r},\widehat{\boldsymbol{\Omega}},t\right)\varphi^{(g')}\left(\boldsymbol{r},\widehat{\boldsymbol{\Omega}}',t\right)\mathrm{d}\widehat{\boldsymbol{\Omega}}' + S^{(g)}\left(\boldsymbol{r},\widehat{\boldsymbol{\Omega}},t\right)\end{aligned} \tag{2.6}$$

Here the scattering cross-section $\Sigma_{\mathrm{s}}^{(g'\to g)}$ is averaged as

$$\Sigma_{\mathrm{s}}^{(g'\to g)}\left(\boldsymbol{r},\widehat{\boldsymbol{\Omega}}'\to\widehat{\boldsymbol{\Omega}},t\right) = \frac{\int_{E_{g'-1}}^{E_{g'}}\Sigma_{\mathrm{s}}(\boldsymbol{r},E')\varphi\left(\boldsymbol{r},E',\widehat{\boldsymbol{\Omega}}',t\right)\int_{E_{g-1}}^{E_g} f_{\mathrm{s}}\left(\boldsymbol{r},E'\to E,\widehat{\boldsymbol{\Omega}}'\to\widehat{\boldsymbol{\Omega}}\right)\mathrm{d}E\,\mathrm{d}E'}{\varphi^{(g')}\left(\boldsymbol{r},\widehat{\boldsymbol{\Omega}}',t\right)}; \quad \textbf{(2.7)}$$

the multigroup fission spectrum $\chi^{(g)}$ and the source term $S^{(g)}$ are the sum of the contribution of the whole group, as

$$\chi^{(g)}(\boldsymbol{r}) = \int_{E_{g-1}}^{E_g}\chi(\boldsymbol{r},E)\,\mathrm{d}E \quad \textbf{(2.8)}$$

$$S^{(g)}\left(\boldsymbol{r},\widehat{\boldsymbol{\Omega}},t\right) = \int_{E_{g-1}}^{E_g} S\left(\boldsymbol{r},E,\widehat{\boldsymbol{\Omega}},t\right)\mathrm{d}E\,; \quad \textbf{(2.9)}$$

the multigroup fission cross-section $\nu\Sigma_{\mathrm{f}}^{(g)}$ incorporates the contribution of the average number of neutrons produced per fission ν, as

$$\nu\Sigma_{\mathrm{f}}^{(g)}\left(\boldsymbol{r},\widehat{\boldsymbol{\Omega}},t\right) = \frac{\int_{E_{g-1}}^{E_g}\nu(\boldsymbol{r},E)\Sigma_{\mathrm{f}}(\boldsymbol{r},E)\varphi\left(\boldsymbol{r},E,\widehat{\boldsymbol{\Omega}},t\right)\mathrm{d}E}{\varphi^{(g)}\left(\boldsymbol{r},\widehat{\boldsymbol{\Omega}},t\right)}; \quad \textbf{(2.10)}$$

the group neutron velocity $v^{(g)}$ is averaged as

$$\frac{1}{v^{(g)}\left(\boldsymbol{r},\widehat{\boldsymbol{\Omega}},t\right)} = \frac{\int_{E_{g-1}}^{E_g}\frac{1}{v(E)}\varphi\left(\boldsymbol{r},E,\widehat{\boldsymbol{\Omega}},t\right)\mathrm{d}E}{\varphi^{(g)}\left(\boldsymbol{r},\widehat{\boldsymbol{\Omega}},t\right)}. \quad \textbf{(2.11)}$$

As a consequence of the link between neutron energy and flight direction, the averaging procedure makes the multigroup XSs directional- and time-dependent. A simplification is often employed, dropping the multigroup XSs directional dependence (Knott and Yamamoto, 2010, pp. 970–971). This however implies that:

- the energy spectrum of the neutron flux does not depend on the flux direction, i.e. the flux can be split in the direction contribution ζ and the scalar flux

$$\varphi\left(\boldsymbol{r},E,\widehat{\boldsymbol{\Omega}},t\right) \approx \zeta\left(\widehat{\boldsymbol{\Omega}}\right)\cdot\Phi(\boldsymbol{r},E,t); \quad \textbf{(2.12)}$$

- the directional reaction rate $RR_{x,\boldsymbol{\Omega}}^{(g)}$ in each cell is not kept constant, but only the total one $RR_x^{(g)}$ is, i.e.

$$RR_x^{(g)}(\boldsymbol{r},t) = \oint \int_{E_{g-1}}^{E_g} \Sigma_x(\boldsymbol{r},E)\varphi\left(\boldsymbol{r},E,\widehat{\boldsymbol{\Omega}},t\right) \mathrm{d}E\, \mathrm{d}\widehat{\boldsymbol{\Omega}} = \Sigma_x^{(g)}(\boldsymbol{r},t)\Phi^{(g)}(\boldsymbol{r},t) \tag{2.13}$$

$$RR_{x,\boldsymbol{\Omega}}^{(g)}\left(\boldsymbol{r},\widehat{\boldsymbol{\Omega}},t\right) = \int_{E_{g-1}}^{E_g} \Sigma_x(\boldsymbol{r},E)\varphi\left(\boldsymbol{r},E,\widehat{\boldsymbol{\Omega}},t\right) \mathrm{d}E \neq \Sigma_x^{(g)}(\boldsymbol{r},t)\varphi^{(g)}\left(\boldsymbol{r},\widehat{\boldsymbol{\Omega}},t\right) \tag{2.14}$$

Alternative formulations, not requiring the approximation (2.12)-(2.14), are possible: e.g. the "consistent P approximation" (Appendix B) is a P approximation obtained without imposing such condition. It is also possible to accept the direction dependence of the XSs and use them as they are, as described in literature, e.g. by Won and Cho (2011), Douglass and Rahnema (2012) and Larsen et al. (2017).

Based on eq. (2.13), the multigroup XSs are often defined as

$$\Sigma_{\mathrm{t}}^{(g)}(\boldsymbol{r},t) = \frac{\int_{E_{g-1}}^{E_g} \Sigma_{\mathrm{t}}(\boldsymbol{r},E)\Phi(\boldsymbol{r},E,t)\, \mathrm{d}E}{\Phi^{(g)}(\boldsymbol{r},t)}; \tag{2.15}$$

$$\nu\Sigma_{\mathrm{f}}^{(g)}(\boldsymbol{r},t) = \frac{\int_{E_{g-1}}^{E_g} \nu(\boldsymbol{r},E)\Sigma_{\mathrm{f}}(\boldsymbol{r},E)\Phi(\boldsymbol{r},E,t)\, \mathrm{d}E}{\Phi^{(g)}(\boldsymbol{r},t)}; \tag{2.16}$$

The hypothesis expressed in equation (2.12) should not be applied to the scattering (also denoted as transfer) XS, as the direction affects the scattering function (Bell and Glasstone, 1970, pp. 178–180). The more precise corrections required for this term are detailed later, in §2.2.1.

Concerning the group neutron velocity $v^{(g)}$, rather than having a time-dependent value different for each position and direction, it is preferred to recalculate it based on the average energy of the group as

$$v^{(g)} = \sqrt{\frac{2}{m_{\mathrm{n}}} \cdot \frac{E_{g-1}+E_g}{2}} \approx 9.8 \cdot 10^3 \sqrt{E_{g-1}+E_g}\ \mathrm{m\ s^{-1}\ eV^{-1/2}} \qquad [E] = \mathrm{eV}, \tag{2.17}$$

where m_{n} is the neutron mass.

It is important noticing that when the nuclear data are condensed into the multigroup XSs, the neutron flux is introduced as weighting function: hence, they are no more a property of the

considered material, but become problem-dependent. In other words, the same material could have different multigroup XSs in different reactors (or even in the same reactor at different positions). This constitutes an issue when the same few-groups XS libraries are applied to very different systems.

2.2.1 TRANSPORT CROSS-SECTION

As written, the directional component of the scattering term cannot be completely neglected: if one models the scattering as a collision it is evident that the energy lost in the event depends on the deviation angle. This effect is usually taken into account with the transport XS, whose definition is based on the P_1 approximation of the transport equation (Appendix A), which is composed by: the continuity equation

$$\begin{aligned}&\frac{1}{v(E)}\frac{\partial\Phi(\boldsymbol{r},E,t)}{\partial t}+\boldsymbol{\nabla}\cdot\boldsymbol{J}(\boldsymbol{r},E,t)+\Sigma_{\mathrm{t}}(\boldsymbol{r},E)\Phi(\boldsymbol{r},E,t)=\\&=\int_0^{+\infty}\Sigma_{\mathrm{s}}(\boldsymbol{r},E'\to E)\Phi(\boldsymbol{r},E',t)\,\mathrm{d}E'+\\&+\chi(\boldsymbol{r},E)\int_0^{+\infty}\nu(\boldsymbol{r},E')\Sigma_{\mathrm{f}}(\boldsymbol{r},E')\Phi(\boldsymbol{r},E,t)\mathrm{d}E'+\oint S\left(\boldsymbol{r},E,\widehat{\boldsymbol{\Omega}},t\right)\mathrm{d}\widehat{\boldsymbol{\Omega}}\end{aligned}\tag{2.18}$$

and the current equation

$$\begin{aligned}&\frac{1}{v(E)}\frac{\partial\boldsymbol{J}(\boldsymbol{r},E,t)}{\partial t}+\frac{1}{3}\boldsymbol{\nabla}\Phi(\boldsymbol{r},E,t)+\Sigma_{\mathrm{t}}(\boldsymbol{r},E)\boldsymbol{J}(\boldsymbol{r},E,t)=\\&=\int_0^{+\infty}\overline{\mu_0}(\boldsymbol{r},E'\to E)\Sigma_{\mathrm{s}}(\boldsymbol{r},E')\boldsymbol{J}(\boldsymbol{r},E',t)\,\mathrm{d}E'+\oint\widehat{\boldsymbol{\Omega}}\cdot S\left(\boldsymbol{r},E,\widehat{\boldsymbol{\Omega}},t\right)\mathrm{d}\widehat{\boldsymbol{\Omega}},\end{aligned}\tag{2.19}$$

linked together by the current $\boldsymbol{J}$ and the integral flux Φ.

Before proceeding with the multigroup theory, an additional approximation to the current equation is introduced (Bell and Glasstone, 1970, p. 180): after reformulating the dependency of the average scattering angle cosine $\overline{\mu_0}$

$$\overline{\mu_0}(\boldsymbol{r},E'\to E)=\overline{\mu_0}(\boldsymbol{r},E',E-E'),\tag{2.20}$$

one can make a Taylor expansion of the energy integral argument, retaining only the first term

$$\overline{\mu_0}(\boldsymbol{r},E',E-E')\Sigma_{\mathrm{s}}(\boldsymbol{r},E')\boldsymbol{J}(\boldsymbol{r},E',t)\approx\overline{\mu_0}(\boldsymbol{r},E,E-E')\Sigma_{\mathrm{s}}(\boldsymbol{r},E)\boldsymbol{J}(\boldsymbol{r},E,t).\tag{2.21}$$

Hence, after applying eq. (2.21), following the same procedure used to derive eq. (2.6), one obtains from eq. (2.18) and (2.19) the multigroup P_1 approximation of the transport equation: the continuity equation becomes

$$\frac{1}{v^{(g)}}\frac{\partial \Phi^{(g)}(\boldsymbol{r},t)}{\partial t} + \boldsymbol{\nabla}\cdot\boldsymbol{J}^{(g)}(\boldsymbol{r},t) + \Sigma_{\mathrm{t}}^{(g)}(\boldsymbol{r},t)\Phi^{(g)}(\boldsymbol{r},t) = \\ = \sum_{g'}\Sigma_{\mathrm{s}}^{(g'\to g)}(\boldsymbol{r},t)\Phi^{(g')}(\boldsymbol{r},t) + \chi^{(g)}(\boldsymbol{r})\sum_{g'}\nu\Sigma_{\mathrm{f}}^{(g')}(\boldsymbol{r},t)\Phi^{(g')}(\boldsymbol{r},t) + S^{(g)}(\boldsymbol{r},t) \tag{2.22}$$

and the current equation

$$\frac{1}{v^{(g)}}\frac{\partial \boldsymbol{J}^{(g)}(\boldsymbol{r},t)}{\partial t} + \frac{1}{3}\boldsymbol{\nabla}\Phi^{(g)}(\boldsymbol{r},t) + \Sigma_{\mathrm{tr}}^{(g)}(\boldsymbol{r},t)\boldsymbol{J}^{(g)}(\boldsymbol{r},t) = S_{P_1}^{(g)}(\boldsymbol{r},t), \tag{2.23}$$

where

$$S_{P_1}^{(g)}(\boldsymbol{r},t) \triangleq \oint \widehat{\boldsymbol{\Omega}}\cdot S^{(g)}\left(\boldsymbol{r},\widehat{\boldsymbol{\Omega}},t\right)\mathrm{d}\widehat{\boldsymbol{\Omega}} \tag{2.24}$$

$$\boldsymbol{J}^{(g)}(\boldsymbol{r},t) \triangleq \int_{E_{g-1}}^{E_g}\boldsymbol{J}(\boldsymbol{r},E,t)\,\mathrm{d}E \tag{2.25}$$

$$\Sigma_{\mathrm{tr}}(\boldsymbol{r},E) \triangleq \Sigma_{\mathrm{t}}(\boldsymbol{r},E) - \Sigma_{\mathrm{s,P_1}}(\boldsymbol{r},E) = \Sigma_{\mathrm{t}}(\boldsymbol{r},E) - \Sigma_{\mathrm{s}}(\boldsymbol{r},E)\int_0^{+\infty}\overline{\mu_0}(\boldsymbol{r},E,E-E')\,\mathrm{d}E' \tag{2.26}$$

$$\boldsymbol{\Sigma}_{\mathrm{tr}}^{(g)}(\boldsymbol{r},t) \triangleq \frac{\int_{E_{g-1}}^{E_g}\Sigma_{\mathrm{tr}}(\boldsymbol{r},E)\boldsymbol{J}(\boldsymbol{r},E,t)\,\mathrm{d}E}{\boldsymbol{J}^{(g)}(\boldsymbol{r},t)}, \tag{2.27}$$

with $\boldsymbol{\Sigma}_{\mathrm{tr}}^{(g)}$ being referred as *transport cross-section*. Though some studies (Larsen et al., 2017; Stacey, 2001, p. 392) have considered using a directional transport XS (or directional diffusion coefficient), this dependency, which appears only when the original XS is cast into multigroup theory, is often neglected. This implies that the current spectrum Γ does not depend on the direction (which is retained in the component $\boldsymbol{j}$), i.e.

$$\boldsymbol{J}(\boldsymbol{r},E,t) \approx \Gamma(\boldsymbol{r},E,t)\cdot\boldsymbol{j}(\boldsymbol{r},E,t), \tag{2.28}$$

Hence, from eq. (2.25) and (2.27),

$$\Sigma_{\mathrm{tr}}^{(g)}(\boldsymbol{r},t)=\frac{\int_{E_{g-1}}^{E_g}\Sigma_{\mathrm{tr}}(\boldsymbol{r},E)\Gamma(\boldsymbol{r},E,t)\,\mathrm{d}E}{\Gamma^{(g)}(\boldsymbol{r},t)}. \tag{2.29}$$

2.3 CROSS-SECTION CONDENSATION

It is a usual procedure in the nuclear reactor analysis solving the multigroup equation, transport or diffusion, with fine XS libraries algorithm for simplified systems, like homogeneous cells, to obtain a first approximation of the flux distribution in the reactor, to be used for a more precise collapsing of the XSs (Duderstadt and Hamilton, 1976). In this way one can obtain equivalent few-groups libraries, that can be applied to the real model, obtaining very precise results in reasonable computational time (Duderstadt and Hamilton, 1976, pp. 368–369; Stacey, 2001, pp. 390–391; Waltar and Reynolds, 1981, p. 175). This scheme is often applied in ERANOS (Doriath et al., 1993; Rimpault et al., 2002), using ECCO (Rimpault, 1995) to condense the built-in 1968 groups library into the few-groups library which is actually used by the transport solver.

The collapsed flux (with energy group index G) can be related to the fine-group flux (with index g) by breaking the integral in eq. (2.2)

$$\Phi^{(G)}(\boldsymbol{r},t)\triangleq\int_{E_{G-1}}^{E_G}\Phi(\boldsymbol{r},E,t)\,\mathrm{d}E=\sum_{\forall g\in G}\int_{E_{g-1}}^{E_g}\Phi(\boldsymbol{r},E,t)\,\mathrm{d}E=\sum_{\forall g\in G}\Phi^{(g)}(\boldsymbol{r},t). \tag{2.30}$$

In a similar way, one obtains the expressions for the collapsed XSs from eq. (2.13), demanding also in this case that the reaction rates stay unchanged

$$RR_x^{(G)}(\boldsymbol{r},t)=\sum_{\forall g\in G}RR_x^{(g)}(\boldsymbol{r},t)=\sum_{\forall g\in G}\Sigma_x^{(g)}(\boldsymbol{r},t)\Phi^{(g)}(\boldsymbol{r},t)=\Sigma_x^{(G)}(\boldsymbol{r},t)\Phi^{(G)}(\boldsymbol{r},t) \tag{2.31}$$

hence

$$\Sigma_x^{(G)}(\boldsymbol{r},t)=\frac{\sum_{\forall g\in G}\Sigma_x^{(g)}(\boldsymbol{r},t)\Phi^{(g)}(\boldsymbol{r},t)}{\sum_{\forall g\in G}\Phi^{(g)}(\boldsymbol{r},t)}. \tag{2.32}$$

For the transfer XS, one has to take into account both origin and destination groups, but the principle is the same

$$RR_{\mathrm{s}}^{(G'\to G)}(\boldsymbol{r},t)=\sum_{\forall g'\in G'}\sum_{\forall g\in G}RR_{\mathrm{s}}^{(g'\to g)}(\boldsymbol{r},t)=\Sigma_{\mathrm{s}}^{(G'\to G)}(\boldsymbol{r},t)\Phi^{(G')}(\boldsymbol{r},t) \tag{2.33}$$

$$\Sigma_{\mathrm{s}}^{(G'\to G)}(\boldsymbol{r},t)=\frac{\sum_{\forall g'\in G'}\Phi^{(g')}(\boldsymbol{r},t)\sum_{\forall g\in G}\Sigma_{\mathrm{s}}^{(g'\to g)}(\boldsymbol{r},t)}{\sum_{\forall g'\in G'}\Phi^{(g')}(\boldsymbol{r},t)}. \tag{2.34}$$

It is important noticing that, because of eq. (2.23) and the consequent (2.29), the reaction rate to be preserved in the case of the transport XS uses a neutron current weighting rather than a flux one

$$RR_{\mathrm{tr}}^{(G)}(\boldsymbol{r},t)=\sum_{\forall g\in G}RR_{\mathrm{tr}}^{(g)}(\boldsymbol{r},t)=\sum_{\forall g\in G}\Sigma_{\mathrm{tr}}^{(g)}(\boldsymbol{r},t)\Gamma^{(g)}(\boldsymbol{r},t)=\Sigma_{\mathrm{tr}}^{(G)}(\boldsymbol{r},t)\Gamma^{(G)}(\boldsymbol{r},t) \tag{2.35}$$

with, similarly to eq. (2.30),

$$\Gamma^{(G)}(\boldsymbol{r},t)=\sum_{\forall g\in G}\Gamma^{(g)}(\boldsymbol{r},t). \tag{2.36}$$

2.4 ENERGY STRUCTURE

The previous two sections described the multigroup approximation of the transport theory, i.e. the possibility to discretize the continuous energy variable into a finite number of groups, and the XS collapsing procedure, which allows reducing the number of groups while keeping the reaction rates constant. Nevertheless, one has completely ignored a critical point: the position of the energy groups boundaries, i.e. the energy structure, is not known and must be provided as input parameter.

This raises two important questions: whether results are affected by the chosen energy structure and, in case of affirmative answer, how can one choose it appropriately. The number of groups has a relevant effect on the precision of the results: the more the groups, the less discretized are the data; nevertheless, a larger number of groups means higher computational and memory resources requirements. However, the energy boundaries choice has also a great importance on the accuracy. In fact the energy meshing has to be adequate to correctly represent the neutrons histories: generation, slowing down, absorption, fission.

Despite the paramount role of the energy structure, the methods to define it are still vague, mainly based on arbitrary choices. Knott and Yamamoto (2010, p. 943) suggest, as a first step, to

divide the energy space into 3 regions: a fast one, dedicated to the neutrons generated by fission, a resonance range, mainly devoted to absorption and slowing-down interactions, and a thermal region, where slow neutrons can induce more fissions. Such fixed separation of the group roles can hold for thermal systems, while is less defined for fast systems, where fissions occur on the whole energy spectrum.

The regions should then be divided into groups, covering each one approximately the same lethargy interval, i.e. the same energy range in logarithmic terms. Different authors however point out that such method should be corrected to take into account "significant resonances from dominant nuclides" (Knott and Yamamoto, 2010, pp. 943–944) and "special circumstances" (Bell and Glasstone, 1970, p. 181); this means, for example, setting the energy boundaries where "the XSs undergo a marked change" (Bell and Glasstone, 1970, p. 181) or "such that different phenomena are isolated" (Duderstadt and Hamilton, 1976, pp. 368–369). At the same time, according to Duderstadt and Hamilton (1976, pp. 315–317), when setting the energy structure one cannot ignore the neutron flux distribution not only in energy, but also in space.

The parameters that literature stresses as important are indeed the most relevant ones that should be considered in order to get an effective meshing. Still, the procedures leave many choices to the user's discretion: the limits of the 3 regions; which resonance is "significant"; what nuclide is "dominant"; what constitutes a "marked change" in the XS; which XSs are the most important ones…

Many multigroup energy structures, with various groups numbers and oriented to different applications, are available: the 69-groups WIMS library (Askew et al., 1966); the 172-groups XMAS (Santamarina et al., 2004); the 281-groups SHEM library (Hébert and Santamarina, 2008; Hfaiedh and Santamarina, 2005); the 1968-groups ECCO library (Rimpault, 1995); other ultra-fine (~10000 groups) or even hyper-fine (>100000 groups) libraries.

When one has a group structure already available, one can use it as a starting point and refine it into a few-group one, comparing the results with available benchmark until an acceptable energy structure has been found (Kiefhaber, 2000; Kim et al., 2017). Such procedure however requires a large effort, people experienced in neutron physics and knowing in detail the specific reactor. In addition, given the number of parameters that one should consider to perform such work, there is no guarantee that the found structure is actually the best option available.

Moreover, the fact that each system has different composition and geometry, and so XSs and flux, suggests that each reactor system should have a different energy discretization, taking into account the peculiarities of the considered reactor. At the same time, the use of an inadequate

structure to correctly represent the physics of a system risks to undermine the reliability of the results; the problem is also insidious, as it lies in the input data rather than in the calculation itself and can be easily overlooked. Use of "general purpose" few-groups libraries should hence be discouraged in favour of system-specific libraries.

Some attempts have been undertaken in the past to devise automatic procedures for the determination of the energy structure to be used for specific problems. In particular, algorithms based on Particle Swarm Optimization have been proposed by Mosca et al. (2011a; 2011b; 2009; 2008), by Yi and Sjoden (2013) and by Akbari et al. (2012). In all listed studies attention is focused on the library optimization for single pin geometries or pin cells databases; the cell meshing can be homogeneous or heterogeneous, for thermal or fast spectrum reactors. As a consequence, the obtained energy structures are particularly suitable for modelling the neutron behavior in fuel cells, but may be completely inadequate for non-fuel cells. In other words, the produced meshings perform very well with the cells used as basis for the calculation, but may not be adequate for complex systems as they are not built as a compromise among the different cells composing the system itself; also, if the cells are used independently from each other, the optimization algorithm cannot process the information about the neutron passage between the cells, i.e. the spectrum spatial dependency, which according to Duderstadt and Hamilton (1976, p. 317) represents a condition that should be taken into account during the multigroup library generation.

The present work, hence focuses on the optimization of the energy structure, rather than on single cells, on the whole reactor systems: as a consequence the obtained energy meshings are the result of compromises on the needs of all cells at the same time, taking into account also their interactions and their spatial position.

2.5 THE SIMMER CODE

SIMMER is a multi-dimensional, multi-velocity-field, multiphase, multicomponent, Eulerian, fluid-dynamics code coupled with a space- and energy-dependent neutron kinetics module and a structure model (Bohl and Luck, 1990; Kondo et al., 2000; Tobita et al., 2002; Yamano et al., 2008; Yamano et al., 2003). Its primary objective is the study of core disruptive accident scenarios in liquid metal cooled fast reactors, but its flexibility allows employing it also for applications outside of its focus, such as light water reactors, general multiphase problems, steam-explosion problems (Kondo et al., 2000). The code is under continuous development by the Japan Nuclear Cycle Development Institute in collaboration with KIT (Karlsruhe Institute of Technology), CEA (Commissariat à l'énergie atomique et aux énergies alternatives), Institut de

radioprotection et de sûreté nucléaire and many other international research centers and Universities.

The SIMMER modules periodically exchange information, including power, material temperature and distribution (Figure 2.2). The thermal-hydraulics section periodically transfers to the neutronic module the system geometry, composition and temperature, required for the computation of the macroscopic XSs of the system and to perform the transport calculation; thus, the flux distribution is returned to the thermal-hydraulics module for the determination of the thermal power.

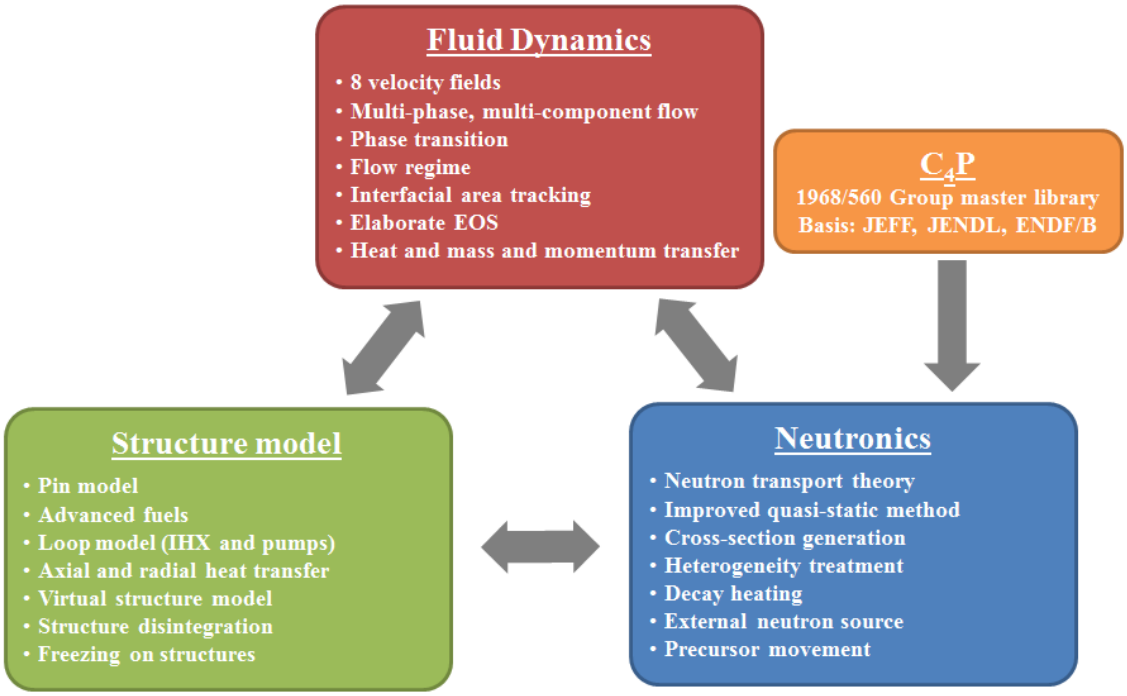

Figure 2.2: SIMMER scheme (after Maschek et al., 2008).

The macroscopic cross-sections are calculated separately for each mesh cell of the system, with the hypothesis that each one can be represented as a homogeneous mixture of its composing isotopes. The macroscopic XSs are obtained starting from the input isotope-wise microscopic XS libraries after application of the resonance self-shielding procedure, performed with the Bondarenko method (Bondarenko, 1964); hence, the Bondarenko f-factors (self-shielding factors) must be included in the input XS libraries and the materials temperatures are required parameters transferred by the thermal-hydraulics section.

The input microscopic cross-sections and f-factors libraries are created in advance using separate computer codes, such as C_4P (Rineiski et al., 2011) or ECCO (Rimpault, 1995), which generate the multigroup libraries starting from the fine-groups data via cell calculations. The user has to choose at this point the energy structure of the XS libraries, which is included in the

libraries and cannot be changed anymore. SIMMER neutronic calculation then follows the energy discretization of the input libraries, with no possible intervention. The next chapter describes an extension, developed in the framework of this study, which instead allows further modifications to the XS energy structure from within SIMMER.

CHAPTER 3. METHODOLOGY

A tool for the condensation of the multigroup XS libraries is suggested and implemented into SIMMER. For the determination of the energy structure to be used, the attempt with greedy algorithms proves unsatisfactory. On the contrary, excellent results can be obtained using genetic algorithms, which are search algorithms inspired by natural selection and evolution. Such algorithm, called METIS, is developed and coupled with the XS collapsing tool and with SIMMER; attention is devoted also on the acceleration of the calculation. Different chromosome (the representation of the possible problem solutions) structures and fitness functions are proposed.

This chapter explains the path that lead to the development of the genetic algorithm for the solution of the energy structure problem. Then, after introducing the genetic algorithm concept, the METIS code, its functioning and its features are detailed.

3.1 CROSS-SECTION COLLAPSING TOOL

The equations (2.32) and (2.35) show that for the generation of equivalent condensed XSs one needs the fine groups neutron flux and current. In other words, one needs in advance the solution of the problem, i.e. the transport equation, to solve it. The circle can be broken by accepting approximate condensed XSs coming out from eq. (2.32) and (2.35), as a consequence of providing approximate flux and current information. Hence one solves an approximated (simpler) formulation of the transport equation with the fine energy structure and then uses the so obtained information to condense the XS libraries, which in turn are employed for the actual transport calculation.

With this in mind, one assumes as weighting functions the neutron flux and current obtained by solving, at each time step and for each mesh cell, the steady state homogeneous medium P_1 approximation of the multigroup transport equation, which are obtained from eq. (2.22) and (2.23) after introducing the mentioned simplifications. The introduction of approximations (P_1, homogeneity, steady state, infinite medium) in the procedure aims at minimizing the time required for the calculation of a good enough weighting flux for each cell, an operation which must be performed at each time step. The continuity equation for the stationary source-free eigenvalue problem, hence, becomes

$$\boldsymbol{\nabla}\cdot\boldsymbol{J}^{(g)}(\boldsymbol{r})+\Sigma_{\mathrm{t}}^{(g)}\Phi^{(g)}(\boldsymbol{r})=\sum_{g'}\Sigma_{\mathrm{s}}^{(g'\to g)}\Phi^{(g')}(\boldsymbol{r})+\frac{1}{k}\chi^{(g)}\sum_{g'}\nu\Sigma_{\mathrm{f}}^{(g')}\Phi^{(g')}(\boldsymbol{r}) \tag{3.1}$$

and the current equation

$$\frac{1}{3}\boldsymbol{\nabla}\Phi^{(g)}(\boldsymbol{r})+\Sigma_{\mathrm{tr}}^{(g)}\boldsymbol{J}^{(g)}(\boldsymbol{r})=0. \tag{3.2}$$

Through eq. (3.2) and introducing the buckling B^2 and a diffusion coefficient D

$$\boldsymbol{\nabla}\cdot\boldsymbol{J}^{(g)}(\boldsymbol{r})=-\frac{1}{3\Sigma_{\mathrm{tr}}^{(g)}}\boldsymbol{\nabla}^2\Phi^{(g)}(\boldsymbol{r})=-D^{(g)}\boldsymbol{\nabla}^2\Phi^{(g)}(\boldsymbol{r})=D^{(g)}B^{2\,(g)}\Phi^{(g)}(\boldsymbol{r}) \tag{3.3}$$

and assuming the flux separability of space and energy components ϕ and ψ

$$\Phi^{(g)}(\boldsymbol{r})\approx\psi^{(g)}\cdot\phi(\boldsymbol{r}), \tag{3.4}$$

the eq. (3.1) can be rewritten as

$$\frac{B^{2\,(g)}}{3\Sigma_{\mathrm{tr}}^{(g)}}\psi^{(g)}+\Sigma_{\mathrm{t}}^{(g)}\psi^{(g)}-\sum_{g'}\Sigma_{\mathrm{s}}^{(g'\to g)}\psi^{(g')}=\frac{1}{k}\chi^{(g)}\sum_{g'}\nu\Sigma_{\mathrm{f}}^{(g')}\psi^{(g')}. \tag{3.5}$$

By substituting eq. (3.4) into (3.2) one obtains the current separability and the relation between current and flux spectra, required to complete the transport XS condensation:

$$\boldsymbol{J}^{(g)}(\boldsymbol{r})=-\frac{1}{3\Sigma_{\mathrm{tr}}^{(g)}}\boldsymbol{\nabla}\Phi^{(g)}(\boldsymbol{r})=-\frac{\psi^{(g)}}{3\Sigma_{\mathrm{tr}}^{(g)}}\cdot\boldsymbol{\nabla}\phi(\boldsymbol{r}). \tag{3.6}$$

The use as XS condensation weighting function is compatible with a convenient normalization, such that eq. (3.5) becomes

$$\left[\frac{B^{2\,(g)}}{3\Sigma_{\mathrm{tr}}^{(g)}}+\Sigma_{\mathrm{t}}^{(g)}\right]\tilde{\psi}^{(g)}-\sum_{g'}\Sigma_{\mathrm{s}}^{(g'\to g)}\tilde{\psi}^{(g')}=\chi^{(g)}, \tag{3.7}$$

more conveniently expressed in its matricial form:

$$\underbrace{\begin{pmatrix} \frac{B^{2(1)}}{3\Sigma_{\mathrm{tr}}^{(1)}} + \Sigma_{\mathrm{t}}^{(1)} & \cdots & 0 \\ \vdots & \ddots & \vdots \\ 0 & \cdots & \frac{B^{2(MG)}}{3\Sigma_{\mathrm{tr}}^{(MG)}} + \Sigma_{\mathrm{t}}^{(MG)} \end{pmatrix}}_{\boldsymbol{L+A}} |\tilde{\psi}\rangle - \underbrace{\begin{pmatrix} \Sigma_{\mathrm{s}}^{(1\to1)} & \cdots & \Sigma_{\mathrm{s}}^{(MG\to1)} \\ \vdots & \ddots & \vdots \\ \Sigma_{\mathrm{s}}^{(1\to MG)} & \cdots & \Sigma_{\mathrm{s}}^{(MG\to MG)} \end{pmatrix}}_{\boldsymbol{S}} |\tilde{\psi}\rangle = |\chi\rangle. \tag{3.8}$$

With the hypothesis of null buckling, the system to be solved becomes

$$(\boldsymbol{A} - \boldsymbol{S})|\tilde{\psi}\rangle = |\chi\rangle. \tag{3.9}$$

The problem (3.8), and so also the (3.9), can be solved by Gaussian elimination for any buckling; in addition, for physical reasons the problem matrix is always column diagonally dominant, so pivoting is not required.

Considering that the upscattering plays a role only for low-energy groups, the matrix is lower triangular for the most energetic groups and full only for the others (Figure 3.1). This observation yields an advantage in terms of computational effort: the triangular part of the matrix can be solved by direct substitution, leaving a much smaller full matrix to be processed with Gaussian elimination.

M	0	0	0	0	0	0	0	0	0
D	M	0	0	0	0	0	0	0	0
D	D	M	0	0	0	0	0	0	0
D	D	D	M	0	0	0	0	0	0
D	D	D	D	M	0	0	0	0	0
D	D	D	D	D	M	U	U	U	U
D	D	D	D	D	D	M	U	U	U
D	D	D	D	D	D	D	M	U	U
D	D	D	D	D	D	D	D	M	U
D	D	D	D	D	D	D	D	D	M

Figure 3.1: Typical matrix shape (D: downscattering, M: main diagonal, U: upscattering).

Yet, the method described above cannot be applied to non-multiplicative mesh cells, as in this case solving (3.9) would return an identically null spectrum. For such cells, the spectrum of a multiplicative cell, chosen as reference by the user, is used as weighting function.

The above described method has been implemented as an extension for SIMMER (Massone et al., 2014) and applied to different problems. One question however remains still open: the choice of the energy discretization for the condensation. As discussed in §2.4, this represents an important issue: finding the answer is complicated and incorrect choices can pose a serious

threat to the correctness of the results. From the attempts to address this point originated the work described in the next sections.

3.2 THE GREEDY APPROACH

As discussed in §2.4, the energy groups boundaries are usually chosen by observation of the energy spectrum, condensing adjacent groups with similar population magnitude and preserving at most spikes and holes in the neutron population.

An elementary approach to the automated search of the energy structure consists in the creation of an algorithm which follows the same criterion: the adjacent groups with the smallest difference in spectrum are condensed together, until the number of groups defined by the user is achieved. This is the essence of a *greedy algorithm*, i.e. an algorithm that "always makes the choice that looks best at the moment" (Cormen, 2001, p. 370; Voß, 2001).

This approach is well-known and employed in a number of fields for its implementation ease and because it ensures a solution with a limited number of steps (Cormen, 2001, p. 370). The drawback is that the solution found is the optimal one only for some classes of problems (better detailed later); most often the algorithm can find only a local optimum, while in special conditions the returned solution could even be the worst option (Bang-Jensen et al., 2004).

An algorithm like this is tested (Massone et al., 2017a) with different collapsing choice criteria:

- Least difference in neutron flux;
- Least difference in reaction rate;
- Least difference in neutron flux per lethargy unit.

Yet, none of the option is able to tackle efficiently the problem, yielding energy structures which cannot replicate correctly the multiplication factor and that are hardly able to describe the neutron physics.

Hence, the approach must be changed, focusing on the objective (in this case, the matching multiplication coefficient) rather than on the spectrum shape. The collapsing is performed progressively (Figure 3.2), one energy cut after the other, repeating the following steps until the desired number of groups is achieved:

I. Calculate the k of all $N-1$ possible solutions resulting from collapsing two adjacent groups;
II. Compare the results with the k of the uncollapsed solution, which is taken as objective, and pick the option with the lowest discrepancy;

III. Collapse the groups corresponding to the chosen solution and proceed with Step I, using the new $N-1$ library as starting point.

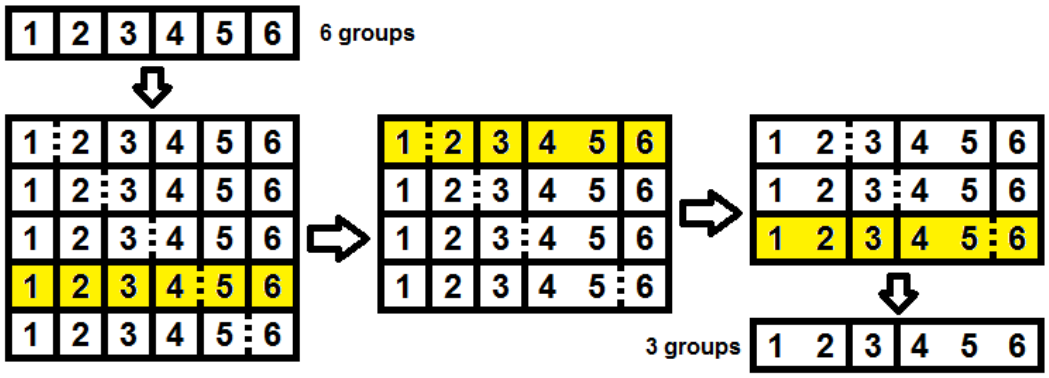

Figure 3.2: Example of progressive greedy collapsing from 6 to 3 groups.

Such an algorithm, however, has to perform many calculations with many energy groups (MG), which is computationally expensive and few tests with few groups (FG), which is cheaper: assuming a linear growth with the number of groups of the computational time required for a k calculation (one will see in §4.8 that this hypothesis is not too far from measured data), one would require a time

$$t \propto MG + \sum_{i=1}^{MG-FG} (MG-i)^2 = \frac{1}{3}(MG^3 - FG^3) - \frac{1}{2}(MG^2 - FG^2) + \frac{7}{6}MG - \frac{1}{6}FG. \quad \textbf{(3.10)}$$

Also, even if improved, it still follows the greedy paradigm, which has already proven unsuccessful with the energy structure question. Indeed, this problem hardly fits the conditions required for a greedy algorithm to converge to the optimal solution (Cormen, 2001, pp. 379–384): optimal substructure and greedy-choice property. Optimal substructure means that a problem solution contains any subproblem solution; in the energy meshing search case, this would mean that the energy cuts of the optimal energy structure with N groups are a subset of the optimal energy cuts with $M>N$ groups. A problem has greedy-choice property if the optimal solution can be reached by subsequent optimal choices; in this case, this property would imply that the best energy structure can be achieved by setting one energy cut after the other, choosing each time the most convenient option. None of the two prerequisites hold in the energy structure problem, as each cut strongly influences the other alternatives, making impossible proceeding step-by-step, especially if the past choices are never reconsidered, like with a greedy algorithm: the energy space has to be considered as a whole, judging each option only based on the final result.

Hence the decision of abandoning the greedy algorithm approach for an evolutionary algorithm that, at the expense of a larger number of tested energy structures (but with a small number of groups, which are computationally cheap), explores the solution space much more thoroughly and is able to converge to reasonable results regardless of the problem formulation.

3.3 GENETIC ALGORITHMS

Genetic Algorithms (GAs) are search algorithms belonging to the wider class of evolutionary algorithms (Bäck and Schwefel, 1993), which are nature-inspired population-based metaheuristics following the principles of the evolution theory based on natural selection (Goldberg, 1989, pp. 1–23).

The establishment of GAs dates from 1975, when John Holland publishes his book "Adaptation in natural and artificial systems" (Holland, 1975); the work however has its background in the studies on the simulation of natural genetic systems and evolutionary computation development (Siddique, pp. 137–178) occurred in previous decades, with the works of Turing (Turing, 1950), Fraser (Fraser and Burnell, 1970), Holland himself (Holland, 1962). Ever since GAs have been applied to a variety of different fields (Goldberg, 1989, pp. 125–142; Kramer, 2017, pp. 73–80), becoming one of the most popular optimization techniques.

The typical genetic algorithm structure considers a starting set of candidate solutions, with randomly generated properties which, based on the effectiveness in solving the posed problem, are selected and evolved until an optimal solution (global or local) is found. The "goodness" of the candidate solution is assessed based exclusively on the results it can provide, through a function called *fitness*. As the best-performing individuals have a higher chance of being used as bases for the construction of a new solution set, the selection process is the driving force of an "evolution" procedure. This justifies the expectation that the overall performance increases with the new solution set, similarly to Darwinian evolution.

As the parallel between artificial and natural genetic systems holds, the biology terminology is often used to denote objects and procedures in the evolutionary algorithms field (Figure 3.3): the candidate solutions are called *individuals* and sets of them are *populations*; each individual is characterized by a *chromosome*, which stores its properties, or *genes*, and by the fitness, which depends on the chromosome through the *fitness function*; the possible values each gene can assume are called *alleles*; the choice procedure is called *selection* and is used to identify the individuals to be used for the *breeding* of the next *generation*. As a consequence the chromosome constitutes the *genotype* of the individual, which is expressed into a *phenotype*, represented by the individual fitness.

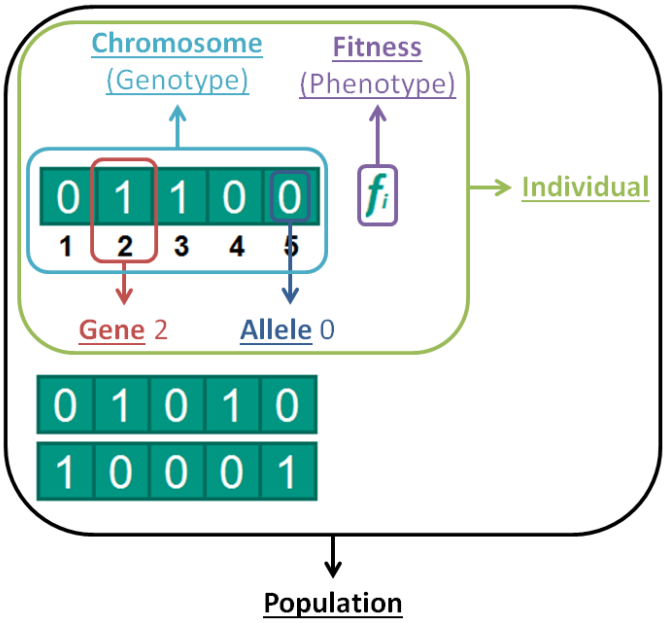

Figure 3.3: Nomenclature for a genetic algorithm.

In addition to the standard procedure, different advanced genetic operators (mutation, elitism, speciation, diploidy…) can be introduced with the objective of improving the solution space exploration capability of the GA, accelerating the convergence, preserving the genetic diversity…

What makes different GAs from analytical methods is that one does not care on how the system works: the system is a black box and the only important thing is the response it gives to different inputs. The objective is not finding a general solution to the problem, e.g. by inverting the system functional, but matching the combination of the input parameters which maximize the output.

Summarizing (Figure 3.4), the GA iterates on the following steps until the fitness converges to a predetermined value or it is stopped due to a different termination condition (elapsed calculation time, number of generation limit…):

I. Evaluate the fitness of each individual in the population;
II. Sort the individuals based on the fitness and select some of them based on such ranking;
III. Crossbreed the selected individuals to create the next generation;
IV. Introduce population corrections to alter convergence and diversity.

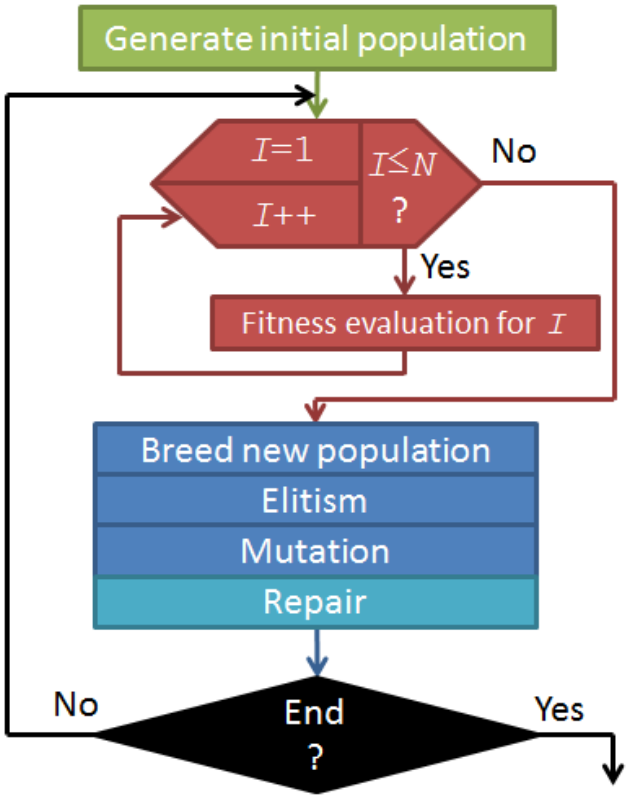

Figure 3.4: Typical GA flowchart (after Massone et al., 2017b). Repair block is specific for the current application (§3.4.1).

3.4 THE ALGORITHM "METIS"

A GA is proposed in substitution of the greedy algorithm for the energy structure search. This algorithm, described in the remainder of this chapter, is hereafter referred "Metaheuristic Energy TIers Search" (METIS). It has been implemented as an extension of SIMMER, together with the XS collapsing tool, and tested in this framework.

3.4.1 CHROMOSOME REPRESENTATION

One of the first issues one should address is the data structure definition, i.e. the way the information that characterizes each solution is stored and expressed. In order to do it, it is helpful identifying the constraints of the problem:

I. The energy cuts of the few-groups libraries constitute a subset of those belonging to the many-groups ones, which also implies that the number of energy cut positions eligible for the former is limited. The reason of this constraint lies in the fact that the loss of information due to XS data averaging during the input libraries generation is irreversible without additional data and, hence, any attempt of splitting an existent group would be based on arbitrary hypotheses.

II. Only solutions having a specific number of groups (*FG*), chosen by the user from the beginning, are considered as possible energy structures. This constraint aims to protect the most interesting solutions, which are those able to adequately represent the energy space with a limited number of groups, from the individuals with a better discretization capability (i.e. more groups), which are favored in the competition and would eventually drive the former solution group to extinction. Even if this constraint could be relaxed, e.g. by balancing the advantage deriving from the additional groups through a penalty method (Goldberg, 1989, pp. 85–86; Smith and Coit, 1997), it leaves the ultimate choice on the number of groups that the final libraries will have, and so on the precision and the computational time connected to the use of those data set, to the user, which then can choose based on his needs.

Based on the constraints, two options for the chromosome representation have been considered (Figure 3.5):

- binary, having chromosomes composed of one gene per energy cut in the many-groups libraries and the Boolean values as alleles;
- non-binary, having in the chromosomes one gene per each energy cut in the few-groups libraries, and alleles that indicate only the energy cuts from the many-groups libraries which are preserved.

In mathematical terms, the binary chromosome C_2 is an ordered tuple belonging to the collection F_2 which includes all sequences of truth values (true $\top$ and false $\bot$) with $MG-1$ elements and exactly $FG-1$ true values, i.e.

$$C_2 \in F_2 \triangleq (\{\top, \bot\}, \{(\top, FG-1), (\bot, MG-FG)\})^{MG-1}. \quad \textbf{(3.11)}$$

Contrary to the tuple C_2, the non-binary chromosome C is a set, meaning that all of its elements must be different, but their order is not relevant; C belongs to the class F, which groups all sets with cardinality $FG-1$ whose elements are natural numbers between 2 and MG (both included), in mathematical notation

$$C \in F \triangleq \{X: X \subseteq \{n \in \mathbb{N}: n \in [2, MG]\} \wedge \#X = FG-1\} \quad \textbf{(3.12)}$$

In both cases the length of the chromosome is equal to the number of groups (MG or FG) reduced by one because the upper and lower energy limits of the many-groups libraries are *per se* also the boundaries of the few-groups ones.

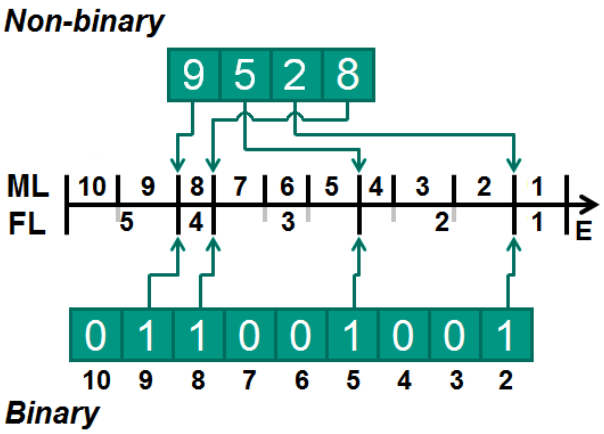

Figure 3.5: Possible chromosome representation for a 5-group solution.
ML and FL denote the many-groups and the few-groups libraries, respectively.

Both options are able to map all the possible solutions, which are

$$\#F = \#F_2 = \binom{MG-1}{FG-1} = \frac{(MG-1)!}{(FG-1)!\,(MG-FG)!}; \tag{3.13}$$

nevertheless the binary representation is more prone to violations of the constraint II (i.e. the number of cuts could not be constant) after chromosome crossing-over (§3.4.4) and mutations (§3.4.5), leading to a more frequent need of corrections, and so to a higher interference in the natural selection procedure. Hence, the non-binary representation has been chosen.

However, as this representation does not completely exclude allele duplications after mutation or crossing-over, a *repair* mechanism, which removes such nonconformities with (3.12), has to be envisioned. Hence all chromosomes included in the next generation are inspected for duplicated alleles; the genes presenting such errors undergo a mutation and the check is repeated until the individual is clear.

3.4.2 FITNESS FUNCTIONS

If one wants to build a natural selection system where the reproductive success depends on the phenotype, one has to define what makes an individual successful. In other words, one needs a systematic way to rank the individuals based on their effectiveness as problem solution.

Such a function is difficult to define: in principle a condensed library can be considered effective if, for the whole transient duration, it is able to produce as solution of the transport equation the same flux and reaction rate distribution as the original one. Nevertheless, one cannot run a whole transient for each candidate solution of each generation: the computational expense has to be considered in the fitness function establishment.

A first approximation for the fitness function can be the one used by Yi and Sjoden (Yi and Sjoden, 2013), based on the effective multiplication coefficient:

$$f_{\mathrm{k}}^{(I)} \triangleq \left| k^{(I)} - k^{\mathrm{obj}} \right| \cdot 10^5 \tag{3.14}$$

where the k^{obj} is obtained with an eigenvalue calculation using the uncollapsed many-groups libraries as input (Massone et al., 2017a).

Nevertheless, the k does give a measurement on how well the neutron flux is represented with the new energy structure only indirectly; it is an integral parameter and it could conceal the presence of compensation effects (Massone et al., 2017c). Hence, one can try to define a different fitness function based on the flux spectrum match.

The scalar flux for each fine group can be calculated in the same way of the, k^{obj} by an eigenvalue calculation. Recalling eq. (2.30)

$$\Phi_{\mathrm{obj}}^{(G,C)} = \sum_{\forall g \in G} \Phi_{\mathrm{obj}}^{(g)} = \sum_{g=C_{G-1}}^{C_G - 1} \Phi_{\mathrm{obj}}^{(g)}, \tag{3.15}$$

the ideal energy structure for the individual I would yield

$$\Phi_I^{(G)} = \Phi_{\mathrm{obj}}^{(G,C)} \quad \forall G \in [1, FG]. \tag{3.16}$$

A usual way to measure the difference between two vectors is the cosine of the angle within the two in the hyperspace with components $\widehat{\Phi}^{(G)}$, as in Figure 3.6:

$$\Xi_I \triangleq \cos \xi_I = \boldsymbol{\Phi}_I \cdot \boldsymbol{\Phi}_{\mathrm{obj}}^{(C)} = \frac{1}{\|\boldsymbol{\Phi}_I\| \cdot \left\|\boldsymbol{\Phi}_{\mathrm{obj}}^{(C)}\right\|} \sum_{G=1}^{MG} \left[\Phi_I^{(G)} \cdot \Phi_{\mathrm{obj}}^{(G,C)}\right]. \tag{3.17}$$

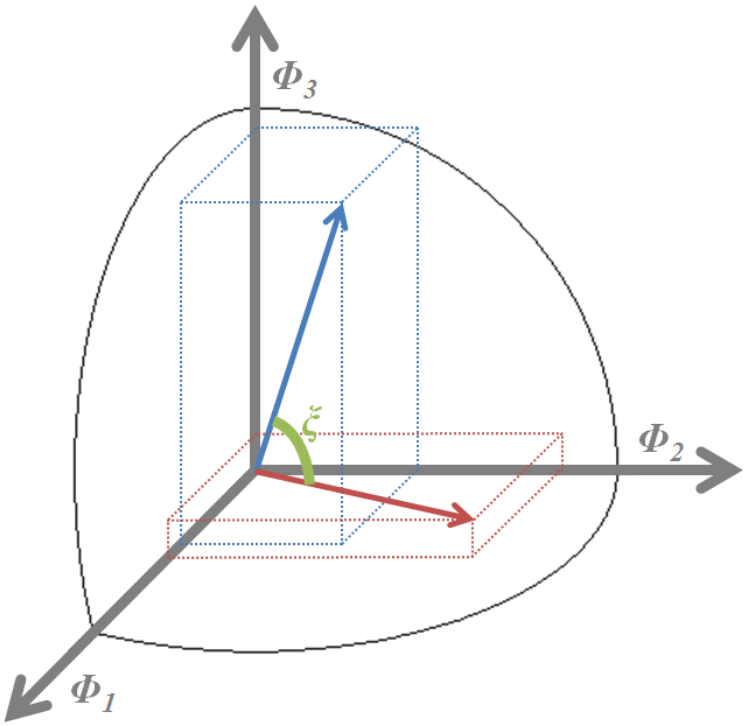

Figure 3.6: Multigroup neutron flux phase space with 3 groups (after Massone et al., 2017c).

As each mesh cell of the system has its own Ξ_I, the new flux-dependent fitness coefficient $f_{\boldsymbol{\Phi}}^{(I)}$ is based on the cosine average over all cells in the system:

$$f_{\boldsymbol{\Phi}}^{(I)} \triangleq \frac{1}{\pi}\arccos\left(\frac{1}{N_{\text{cells}}}\sum_{c=1}^{N_{\text{cells}}}\Xi_{I,c}\right). \tag{3.18}$$

As $\Xi_{I,c}$ is always positive (because $\boldsymbol{\Phi}$ cannot have negative components with physical meaning), $f_{\boldsymbol{\Phi}}^{(I)}$ can only assume values between 0 and 0.5.

A fitness function $f_{\text{comb}}^{(I)}$ combining the two described above can also be defined (Massone et al., 2017c). In order to weigh the two components, which have different metrics, a geometric mean rather than an arithmetic one should be used (Fleming and Wallace, 1986):

$$f_{\text{comb}}^{(I)} \triangleq \sqrt{f_{\text{k}}^{(I)} \cdot f_{\boldsymbol{\Phi}}^{(I)}} \tag{3.19}$$

Other fitness functions are of course viable options, which could be tested in future studies, alone or combined: adjoint eigenvalue and flux, reaction rate discrepancies, α-eigenvalues…

3.4.3 SELECTION

The selection is the procedure which picks some individuals from the population to build a *mating pool*, which is then used for establishing the next generation. The selection, in order to have a positive effect on the fitness, cannot be a simple random sampling, but has to take into account the phenotype of the individuals, preferring the fit over the unfit.

However, the correct setting of the selection pressure is a very delicate point. The work of Miller and Goldberg (1996) points out the risks of an incorrect setting: "if the selection pressure is too low, the convergence rate will be slow, and the GA will unnecessarily take longer to find the optimal solution. If the selection pressure is too high, there is an increased chance of the GA prematurely converging to an incorrect (sub-optimal) solution. In addition to providing selection pressure, selection schemes should also preserve population diversity, as this helps avoiding premature convergence."

Hence, the key is the balance between selection pressure, which promotes the use of good individuals over the others, and genetic diversity, which is required to avoid the evolution stopping.

Many different selection schemes exist (proportional, roulette, rank-based…), whose performance depends on the specific problem (Siddique, pp. 165–166), but in this case a tournament selection (Blickle and Thiele, 1996; Goldberg and Deb, 1991) of the stochastic type has been chosen, characterized by the easy maintainability (Miller and Goldberg, 1995).

After the fitness calculation, each individual I of the population is randomly assigned to one of the N_T "tournaments" (Figure 3.7), with the number of tournaments N_T fixed by the user. Separately for each tournament the participant individuals are sorted based on their fitness function. Each individual obtains a number of copies in the mating pool

$$N^{(I)} = p \cdot (1-p)^{R^{(I)}-1} \tag{3.20}$$

based on the ranking $R^{(I)}$ achieved in its own tournament and the probability parameter p.

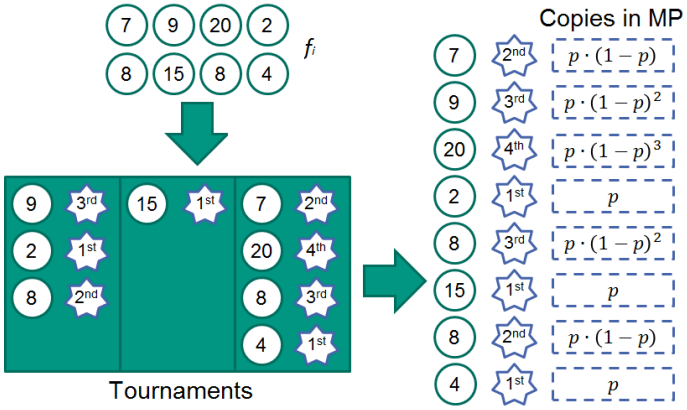

Figure 3.7: Example of stochastic tournament selection and mating pool (MP).

Other common selection schemes can be considered as special cases (based on the parameters N_T and p) of the tournament:

- Pure random sampling is obtained when p approaches 0 or N_T tends to infinity;
- Deterministic tournament selection, i.e. only the tournament winner enters the mating pool, corresponds to p=1;
- Rank-based sampling is the special case corresponding to N_T=1.

The so produced mating pool constitutes the basis for the breeding procedure. It is worth clarifying that the mating pool concept has to be intended as an assignment of a breeding probability (ranging from 0 to 1) to each population individual, and there is hence no obstacle to fractional number of copies.

3.4.4 BREEDING

The breeding is the procedure leading to the definition of a new generation. This is composed by individuals either coming directly from the previous generation or descendants from them.

The new generation G is composed by a number $P^{(G)}$ of individuals as

$$P^{(G)} = P^{(G-1)} \cdot r, \tag{3.21}$$

which depends on the proliferation rate r and on the population of the previous generation $P^{(G-1)}$.

A fraction of slots (defined by the user) is reserved for *elitist* choice, i.e. for the best solutions of the old generation which pass directly into the new one. Elitism avoids the loss of the best candidates, always possible due to random sampling mechanisms, but it can accelerate the reduction of genetic diversity; however "on balance it appears to improve GA performance" (Davis, 1991, p. 34).

The remaining places in the new generation are filled by the offspring of the old generation, produced by *crossing-over*. From the mating pool, one selects with uniform random sampling 2 chromosomes, which through one-point crossing-over (Goldberg, 1989, pp. 10–14) generate 2 new children chromosomes; this procedure is repeated until the new generation is complete.

In one-point crossing-over, the 2 parent chromosomes are split at a randomly chosen gene; the tails of the chromosomes are then switched, so creating 2 new solutions having the genes of the two parents. Duplicated alleles can be present in the offspring chromosomes, which have to be removed with the repair procedure.

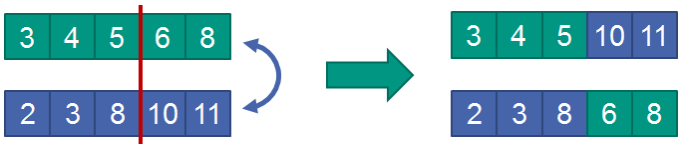

Figure 3.8: Example of crossing-over.

3.4.5 MUTATION AND REPAIR

As natural selection progresses, it is likely that the genetic diversity of the population reduces, with possible disappearance of alleles. As this hinders the discovery of new solutions, a mechanism that allows reintroduction of extinct alleles may help convergence. Through *mutation*, the genes of the new population's chromosomes have a slight chance of having their alleles changed with any other possible allele.

The essential function of the mutation is favouring the *exploitation* of the solution space (Siddique, pp. 161–162), i.e. investigating the solutions belonging to the neighbourhood of the chromosome undergoing mutation. The opposite movement on the solution space is the *exploration*, which aims to find new innovative solutions, radically different from the current options, and is mainly operated through crossing-over operations.

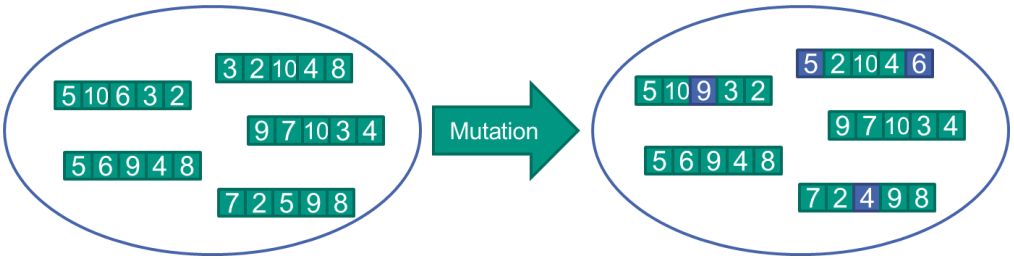

Figure 3.9: Example of mutation.

Mutation is also the mechanism used to solve allele duplication, originating from crossing-over or mutation itself. As such errors are incompatible with the chromosome description defined in §3.4.1, the last step in new generation breeding is a screening of all individuals; in case

duplications are observed, an additional mutation is triggered on one of the genes with duplicated allele. This operation, called *chromosome repair*, is repeated until all duplications have been removed. The new population is now final.

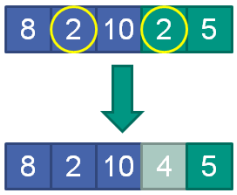

Figure 3.10: Example of repair.

Though mutation is a fundamental operator for solution improvement, the occurrence probability must not be too high; in fact, if the mutation process interferes too much, the natural selection could become a totally random walk. It is important that one takes into account this point when setting the mutation rate, also considering that repair operations can contribute to artificial increasing of the number of mutations.

3.5 GENES SORTING

In §3.4.1 the chromosome is defined in eq. (3.12) as a set of genes: this implies that two chromosomes bringing the same alleles in different genes describe the same physical solution, as it actually is. However, when one implements the chromosome into the computer code as arrays, the order of the genes can make a difference during the crossing-over procedure. This leads to the question on whether is better resorting the chromosomes based on the genes allele or limiting the interferences in the selection process.

Different reasons support the unsorted chromosome option:

a) Frequent chromosome resorting easily breaks established schemata;
b) When chromosomes are sorted, the crossing-over always separates their two ends, leading to an unequal treatment between external and central groups;
c) Corresponding genes in two sorted chromosome are likely to code for the same or a close allele, which limits alleles remixing;
d) Similarly to c), the movement of an energy cut along the energy spectrum (e.g. from the thermal to the fast region) is hindered by sorted chromosomes.

Tests have been run on two sodium-cooled fast reactors, ESNII+ ASTRID (described in §4.2.1) and ESFR (§4.2.2), about the ordering issue. The GA has been run twice with unsorted chromosomes and 3 times with sorted ones for each reactor system, and overall rankings of the solutions have been established. One observes (Figure 3.11) that, for both reactors, among the

best 30 solutions the number of solutions discovered by the unsorted chromosomes GA is much lower than the expectancy value.

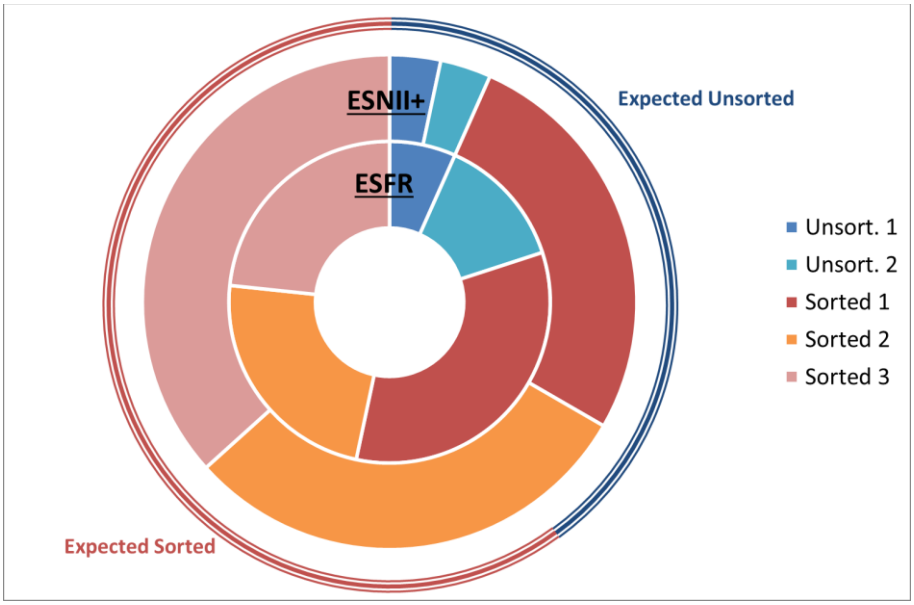

Figure 3.11: GA chromosome configuration of the 30 best solutions for ESNII+ ASTRID and ESFR cases (after Massone et al., 2017a).

These results are in disagreement with the initial hypothesis that unsorted chromosomes work better; hence one should reflect on the logic initially assumed.

Understanding the physics of the neutron movement over the energy space is the key to understanding the fallacies in the reasons listed: in particular, the central point is that the interconnection between groups is very strong if they are adjacent or close, while it is weak if they are apart on the energy space (neutrons exchange will be very rare in this case). On this basis, the reasons can be reexamined in favor of sorted chromosomes:

a) Once the chromosome has been sorted, neighboring genes denote neighboring groups which are indeed preserved during crossing-over; it is very likely that during such operation, only one group is broken. Thus, the preserved schemata have a clear counterpart in the neutron system;
b) Indeed the two ends of a chromosome are always separated, but this does not constitute a problem, as the connection between fast groups and low-energy ones is small;
c) The correspondence of genes in different chromosomes is beneficial, as it helps reducing the need for resorting of the offspring chromosomes, meaning that less adjacent group couples are disrupted during a crossing-over.

d) This difficulty in moving energy cuts along the energy space represents the downside of c). However, even if crossing-overs can provoke only slow progressive shifts, one can rely on mutations for rapid movements.

The conclusion is that, when sorted, the chromosomes have a closer counterpart to the physical problem and can better represent it. The drawback is that the shift of the energy cuts along the energy space is deterred and takes longer. In other words, "the convergence is less erratic, but the exploration of the solution space might benefit of an increased mutation rate" (Massone et al., 2017a).

The outcome is suggested by Figure 3.12 and Figure 3.13, which show, respectively, the fitness convergence trend and the percentage of original chromosomes (i.e. not tested in previous generations), based on the sorting choice. One observes that, for all reactor systems, the sorted chromosomes cases outperform the unsorted ones both in convergence speed and in stability of the decreasing trend. On the other hand Figure 3.13 shows that calculations with sorted chromosomes are more likely to reconsider already explored individuals; this suggests a lowered exploration capability, which should instead be promoted, e.g. by increasing the mutation rate, in particular in later generations (Shi et al., 1999; Siddique, pp. 161–165).

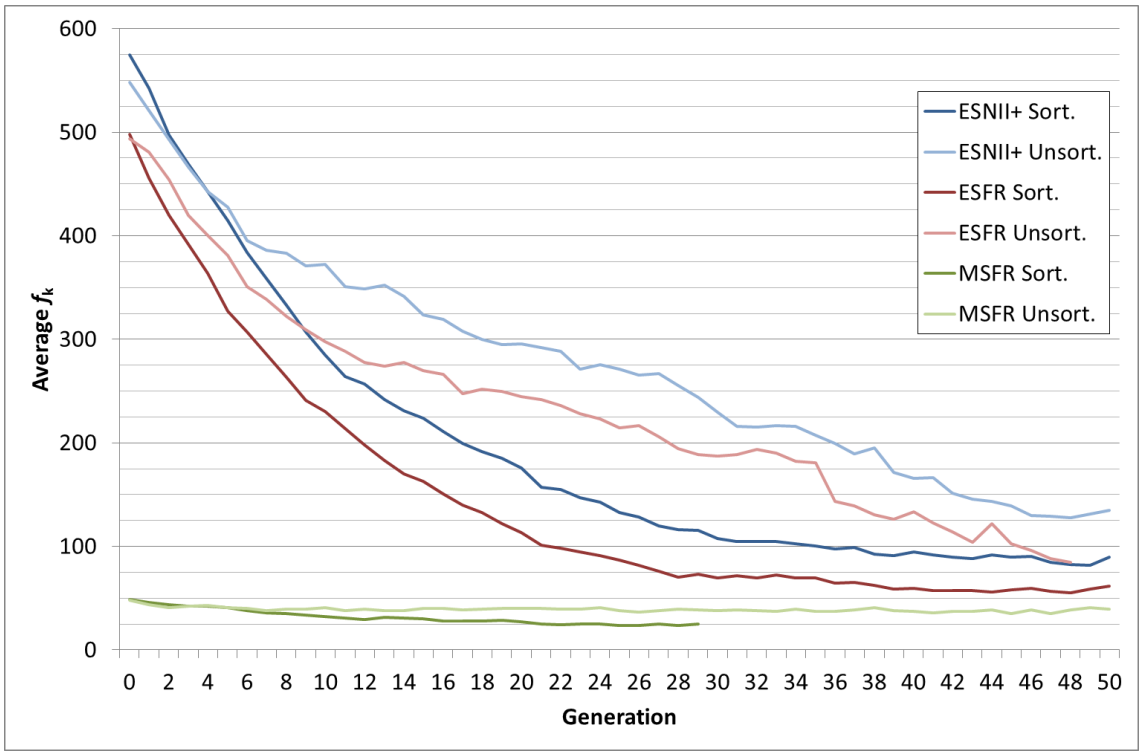

Figure 3.12: Average fitness convergence for ESNII+, ESFR and MSFR.

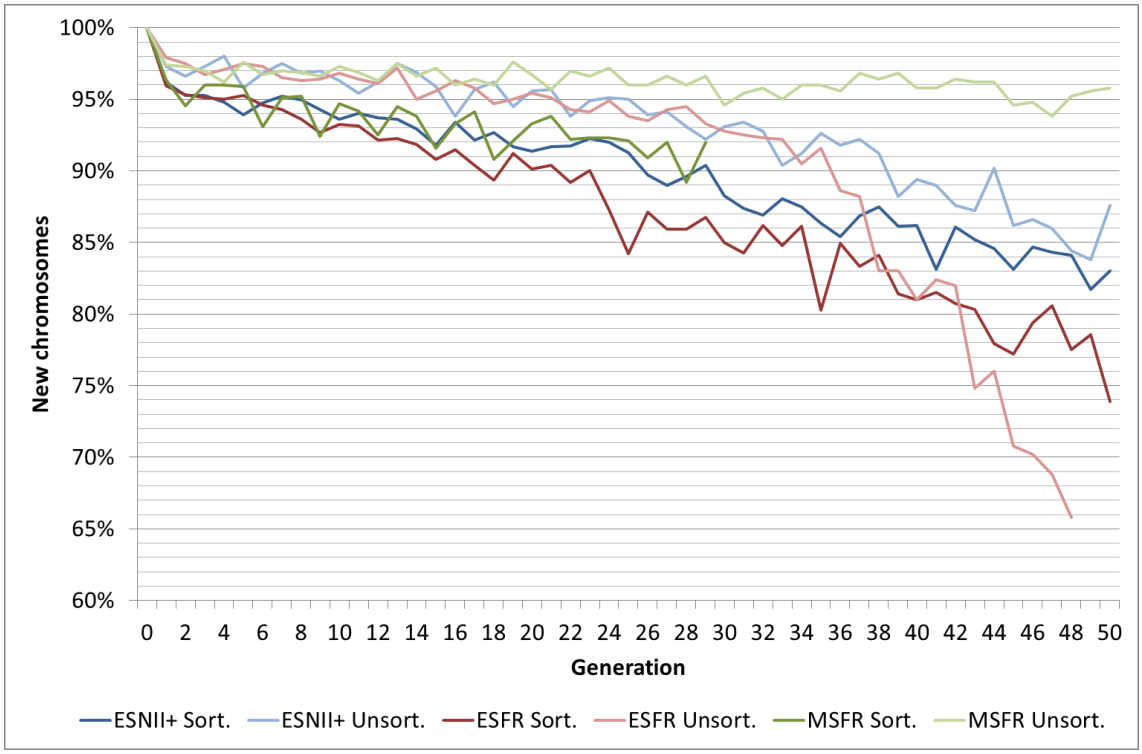

Figure 3.13: Share of original chromosomes in each generation for ESNII+, ESFR and MSFR.

3.6 ACCELERATION

One of the main goals of the XS collapsing procedure is the reduction of the calculation time without affecting the precision of the results (conversely, increasing the precision the computational effort being equal). The largest effort reduction is related to the transport solver which, dealing with a smaller number of groups, converges faster. Nevertheless, both the XS collapsing procedure and the genetic algorithm require additional steps, i.e. computational time. Hence, different techniques have been applied to limit the computational expense, and particular care has been given to the choice of the sorting and sampling algorithms.

Also, parallelization implementation is straightforward, as the study of each individual is independent from the others and can, hence, be performed at the same time.

3.6.1 FLUX EDUCATED GUESS

The evaluation of the fitness function constitutes by far the largest time expense of the GA run, as common with optimization problems. Thus, as this operation has to be repeated for a large number of individuals, it is important to reduce the required computational time.

One option is supporting the *k* calculation convergence by providing a better neutron flux initial guess than the default one. This can be calculated starting from the flux distribution assessed

with the many-groups libraries, which is a "by-product" of the objective k determination, using the flux collapsing formula (2.30).

The so obtained condensed (based on the chromosome under exam) flux constitutes a well educated guess, which helps the transport solver to converge to the required eigenvalue within few (typically 3 or 4) outer iterations.

The actual time reduction depends on the specific chromosome but it can be estimated that the computational effort is lowered by more than 30%; at the same time, the educated guess is obtained via simple sums, with negligible impact on the computational time.

3.6.2 FITNESS STORAGE

Being the genetic pool in this case finite, the probability that the same individual appears in more than one generation (or even more than once in the same generation) cannot be calculated by combination counting, as it would be largely underestimated; really, elitism option mandates that some individuals be repeated in the next generation.

In order not to perform twice the fitness calculation of the same individual, one keeps evidence of all considered candidate solutions along with their performance. A binary tree of the kind "left-child right-sibling" (Cormen, 2001, pp. 214–217) can efficiently be used to fulfil this task; the array and linked list options had to be excluded because they require, respectively, a too large space to be allocated and a too long access time.

With the storage option, before each fitness evaluation, one searches the tree for the considered chromosome: if it is present, the fitness of the individual has already been evaluated and the eigenvalue calculation can be avoided; otherwise, after the fitness is evaluated in the traditional way, a new branch is added to the tree with the new result for future reference.

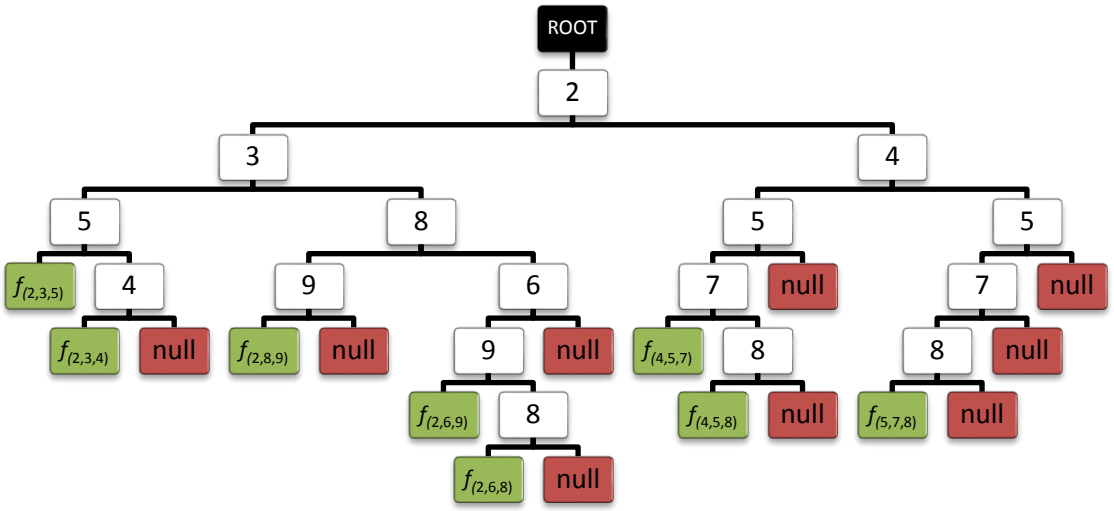

Figure 3.14: Binary tree example for a case with FG=3. Green leaves denote available fitness values, red leaves incomplete branches (cases not yet found).

The time reduction consequent to the avoided calculations is orders of magnitude larger that the effort required for allocating, updating and searching the storage.

3.6.3 SAMPLING ALGORITHM

For selection mechanisms, a random sampling method is required. The Alias Method (Walker, 1977) is in general efficient and works well in this case, as a large number of sampling has to be done with the same probability distribution. This allows reusing the same probability tables, whose creation is the most time consuming operation of the method.

The method is based on the construction of a probability table and an Alias table, which allow to model each random sampling with a fair-dice roll and a biased-coin flip; both operations are very easy from the computational point of view and do not require a search algorithm (which, on the contrary, can be computationally-expensive).

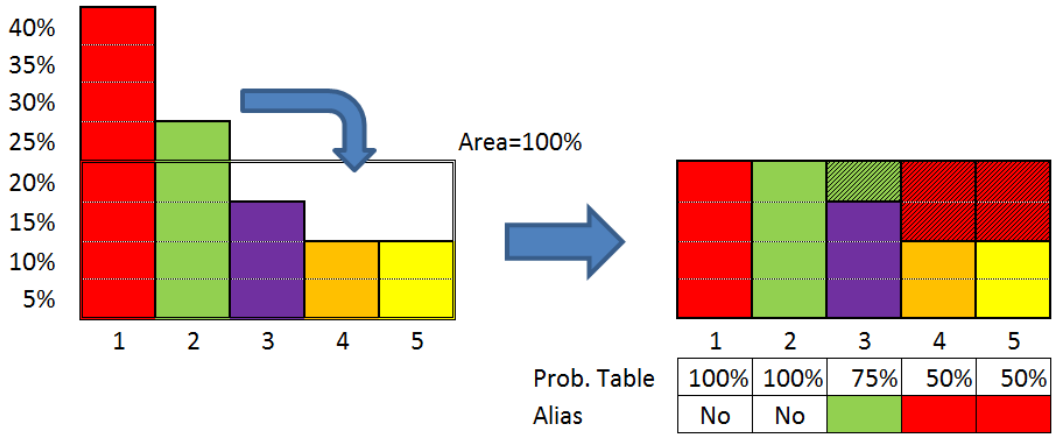

Figure 3.15: Example of alias method.

The time required for the creation of probability tables of length n (it is possible to demonstrate that it is always possible to do it) is $O(n)$, while each sampling is completed in $O(1)$ (Vose, 1991).

The asymptotic notation is commonly used in computer science to compare the efficiency of alternative algorithms (Cormen, 2001, pp. 41–50). The O-notation is used to denote functions which are asymptotically bounded from above by another function. Considering the computational time a function $f(n)$ of the variable n and $g(n)$ another function of n,

$$f(n) \in O\big(g(n)\big) \Leftrightarrow \exists c, n_0 \in \mathbb{R}, c > 0 : \forall n > n_0, f(n) \leq cg(n). \quad \textbf{(3.22)}$$

In other words, the computational time of an algorithm belonging to the set $O(n)$ grows at most linearly with n; with the set $O(1)$, the computational time is independent from n.

The Θ-notation, similarly to O-notation, binds asymptotically the function; in this case, however, the function is bounded from both above and below, i.e.:

$$f(n) \in \Theta\big(g(n)\big) \Leftrightarrow \exists c_1, c_2, n_0 \in \mathbb{R}, c_1, c_2 > 0 : \forall n > n_0, c_1 g(n) \leq f(n) \leq c_2 g(n). \quad \textbf{(3.23)}$$

From (3.22) and (3.23) immediately descends

$$\Theta\big(g(n)\big) \subseteq O\big(g(n)\big), \quad \textbf{(3.24)}$$

i.e. the Θ-notation is stronger than the O-notation.

3.6.4 SORTING ALGORITHM

A sorting algorithm is required both for providing the individuals as input of the XS collapsing tool (which requires the energy structure to be provided in ascending order) and for ranking the individuals according to their fitness.

The simplest algorithms, such as bubble (Knuth, 1997-2011, pp. 105–110, vol. 3) and insertion sort (Knuth, 1997-2011, pp. 80–84, vol. 3), are efficient with almost sorted arrays: their complexity is $O(n)$ only for the best case, while in both average and worst cases it is $O(n^2)$.

As the fitness ranking is rarely close to the best case, the merge sort (Knuth, 1997-2011, pp. 111–113, vol. 3; Sedgewick and Wayne, 2011, pp. 270–287) has been implemented. The chosen method belongs to the wider group of the Divide & Conquer algorithms and has a lower complexity, $\Theta(n \log n)$ (Cormen, 2001, pp. 27–37), besides being easy to code.

The algorithm divides the array into couples and sorts them; then merges the couples two by two into sorted quadruples, taking advantage of the fact that the couples are already sorted. The procedure continues with n-tuples merged into $2n$-tuples, until the whole array has been reconstructed.

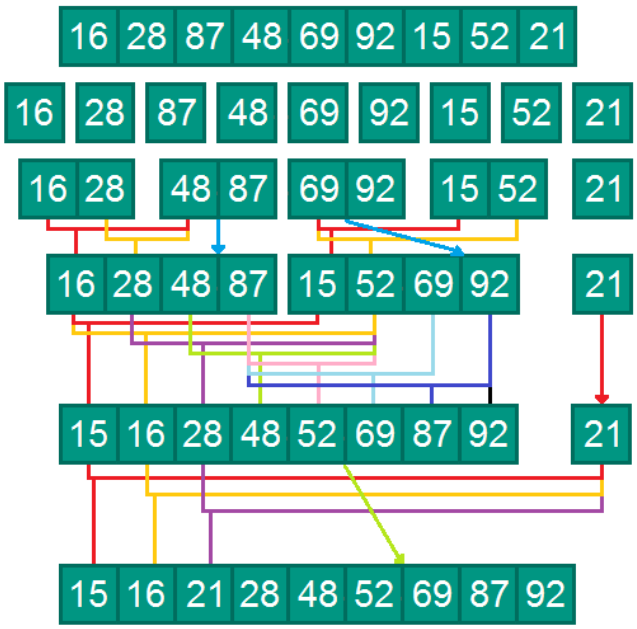

Figure 3.16: Merge sort procedure.

CHAPTER 4. VERIFICATION AND RESULTS

The METIS algorithm, proposed in the previous chapter, must be now tested to prove its correctness and effectiveness. Three test systems are considered: two sodium-cooled fast reactors and a molten salt reactor. The tests show that, generation after generation, the GA population usually converges to similar patterns, different for each reactor; these solutions prove able to replicate the multiplication factor, the void and Doppler feedback coefficients, and the reaction rates. Similar reactors have similar optimal energy structures. The study of the GA results suggests interesting considerations on the effects some features of the studied systems can have on the reactor physics. The combined use of the XS collapsing tool and METIS allows to reduce greatly the time required for the neutronic calculations, while ensuring that the chosen energy structure will not inadvertently affect the reliability of the results.

This chapter is devoted to the tests performed to demonstrate the effectiveness of the METIS algorithm. The results obtained are compared and analysed based on the reactor features and on the neutron physics. A short introduction is given regarding the algorithm configuration and the considered tests systems. Finally the computational time gained using the XS collapsing tool and required by METIS is assessed.

4.1 CONFIGURATION

The objectives of the verification tests will be the calculation of an 11-group structure which can correctly reproduce the reference results (k, reactivity, feedback effects,…), defined as those produced by the same code when using the original uncollapsed libraries, chosen as the 72-groups libraries used at KIT for SIMMER analyses (Rineiski et al., 2011). The choice of using 11 groups for the few-groups libraries is related to the fact that the most used libraries at KIT for deterministic calculations using SIMMER have that number of groups (Kiefhaber, 2000); moreover, such a discretization is expected to yield a good representation of the energy spectrum combined with a relevant computational time reduction. Nevertheless, both METIS and the XS collapsing tools are developed such that the choice of the number of groups used in the final libraries is always left to the user, who can arbitrarily choose any number of groups between 1 and MG.

The GA convergence objective have been explicitly set to a very challenging level in order to avoid premature interruption of the calculation after encountering a sub-optimal solution. The

latter, in fact, would be probably sufficient for most applications, but longer calculations are more useful in case the efficiency of the algorithm itself is studied. For the same reasons, the population size is much larger than usually required for common studies and the selection pressure is kept to a low level. Obviously, the computational effort associated to these choices strongly increases, raising the time required for convergence, typically a few hours for a sub-optimal (but still acceptable) solution, by one order of magnitude.

The adopted GA configuration is:

- Population: 500 individuals, constant size;
- Tournament selection: 100 tournaments, p=0.1;
- Mutation: 5% randomly chosen chromosomes undergo mutation;
- Elitism: 2% of the population;
- Termination condition: 50 completed generations, or 20 consecutive ones without improvement of the best solution.

As a consequence, the initial generation includes, in average,

$$\bar{n}_A = \frac{P^{(0)} \cdot (FG - 1)}{(MG - 1)} = \frac{500 \cdot 10}{71} \cong 70.4$$

copies of each allele A, a number which is large enough to limit the genetic drift (Mühlenbein, 1995, pp. 67–68), i.e. the tendency of the population to converge to a single individual, even without selection, as a consequence of the random sampling.

The parameters other than population size and termination conditions determine how the selection and breeding operators will work, and indirectly the algorithm performance. One should set the parameter to reach an equilibrium point: fit solutions should be promoted, without falling into premature convergence; chromosomes should mutate, but the GA should not degenerate into random search… The parameters optimization is a non-linear and complicated problem itself, which would require a number of trials to find the optimal values and has not been deeply investigated. The results obtained (and shown in this chapter) suggest that the proposed configuration is able to achieve the equilibrium required for the GA functioning. Nevertheless, one cannot exclude that improvements in the performance could be obtained with other configurations.

In addition, the stochastic effect on the results is limited by repeating the GA calculation for each case 5 times (2 for the cases with voided core).

4.1.1 ORIGINAL LIBRARY

The many-groups libraries used for testing is a 72-groups XS data set developed by Rineiski et al. (2011) and used at KIT for SIMMER analyses. Table 4.1 summarizes the energy boundaries of the input libraries.

Table 4.1: Energy groups boundaries of the used many-groups libraries (Rineiski et al., 2011).

g	Upper energy boundary (eV)	*g*	Upper energy boundary (eV)	*g*	Upper energy boundary (eV)	*g*	Upper energy boundary (eV)
1	2.000E+07	19	3.020E+05	37	2.029E+04	55	1.434E+03
2	6.703E+06	20	2.732E+05	38	1.662E+04	56	1.234E+03
3	3.679E+06	21	2.472E+05	39	1.503E+04	57	1.010E+03
4	3.012E+06	22	2.128E+05	40	1.273E+04	58	7.485E+02
5	2.466E+06	23	1.832E+05	41	1.114E+04	59	5.545E+02
6	2.019E+06	24	1.500E+05	42	9.119E+03	60	4.540E+02
7	1.653E+06	25	1.228E+05	43	7.466E+03	61	3.043E+02
8	1.353E+06	26	1.111E+05	44	6.320E+03	62	2.040E+02
9	1.108E+06	27	9.482E+04	45	5.531E+03	63	1.367E+02
10	9.072E+05	28	8.230E+04	46	5.005E+03	64	9.166E+01
11	8.209E+05	29	6.738E+04	47	4.166E+03	65	4.552E+01
12	7.065E+05	30	5.517E+04	48	3.527E+03	66	1.945E+01
13	6.081E+05	31	4.748E+04	49	3.355E+03	67	9.906E+00
14	5.502E+05	32	4.087E+04	50	2.747E+03	68	5.043E+00
15	4.979E+05	33	3.698E+04	51	2.249E+03	69	2.130E+00
16	4.505E+05	34	2.928E+04	52	2.035E+03	70	1.020E+00
17	4.076E+05	35	2.739E+04	53	1.722E+03	71	4.850E−01
18	3.508E+05	36	2.479E+04	54	1.507E+03	72	1.890E−01

The 72-groups library has been built for fast reactor systems, but it will be applied also to the Molten Salt Reactor concept, which belongs to the fast reactor category but is deeply different in term of neutron spectrum.

4.2 TEST SYSTEMS

The effectiveness of this new approach in solving the problem is tested for different nuclear reactor systems. Most of the tests are performed on the Advanced Sodium Technological Reactor

for Industrial Demonstration (ASTRID), developed in the framework of the European Sustainable Nuclear Industrial Initiative (ESNII+) (Bortot et al., 2015; Varaine et al., 2012). In addition, 2 other systems have been included for comparison, choosing both a similar system, i.e. the European Sodium Fast Reactor (ESFR) (Andriolo, 2015; Fiorini and Vasile, 2011; Vasile et al., 2011a), and a dissimilar one, the Molten Salt Fast Reactor (MSFR) (European Commission - CORDIS, 2017; EVOL project, 2011).

The tests are performed on SIMMER-III, the 2D version of the code. The GA approach is anyhow independent from the number of dimensions, and so can be easily transposed to the 3D application, as shown later in Chapter 5.

4.2.1 ESNII+ ASTRID

The ESNII+ ASTRID (Bortot et al., 2015; Varaine et al., 2012) is a Sodium-cooled Fast Reactor (SFR) system, characterized by two fuel zones (an internal and an external one) with different MOX and UO_2 content in the fuel, with a thermal power of 1.5 GW. Its design is based on the low-void effect core CFV (Krepel et al., 2015; Sciora et al., 2011), proposed by CEA for a SFR with a negative void feedback coefficient.

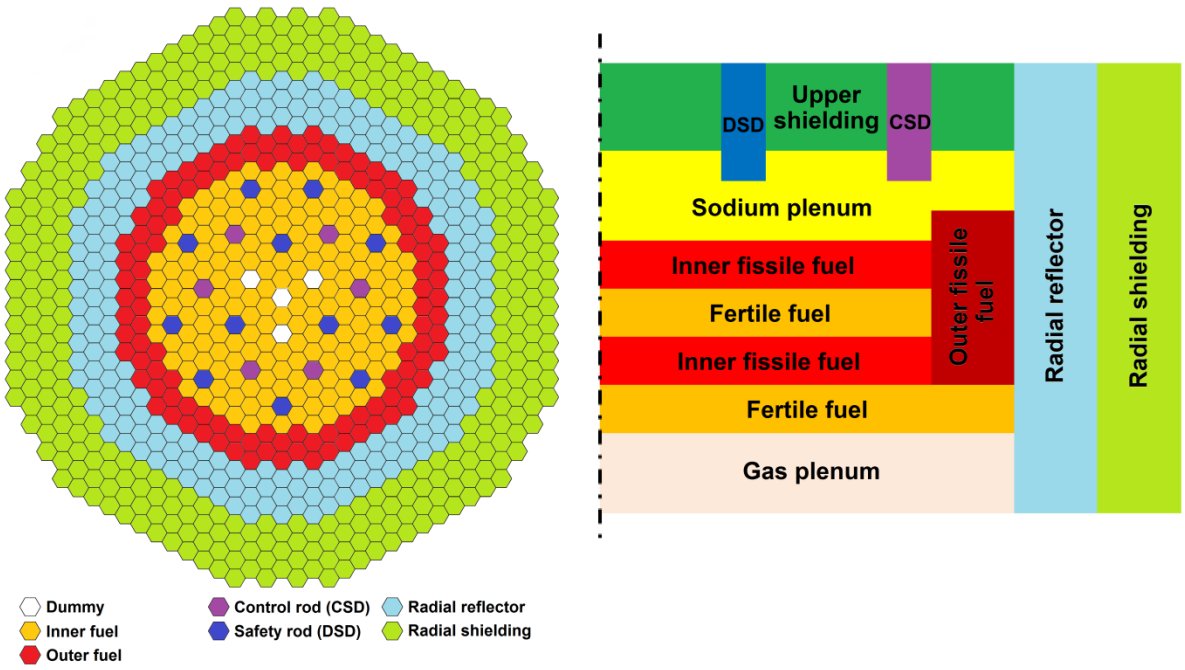

Figure 4.1: ESNII+ ASTRID core radial and axial layout (after Bortot et al., 2015).

The test case is the End of Cycle configuration which is studied at KIT in the framework of the ESNII+ project. The core voided configuration, required for calculating the feedback coefficient (§4.5), corresponds to the reference case with the coolant removed from all fuel zones and from the fertile plate zone; the sodium is not removed from the inter-subassembly gaps.

4.2.2 ESFR

When testing the system, it is interesting comparing the results of the main test case with a similar one, to observe how the system reacts to the small differences of the problem. Hence the choice of the second test case: the ESFR, in the configuration denoted as Working Horse (WH), studied at KIT in the framework of the EURATOM 7th Framework Programme within the CP-ESFR project (2009-2012) (Buiron et al., 2013; Monti, 2015).

As the ESNII+ ASTRID, the ESFR-WH is a SFR with two fuel zones with different enrichment of the MOX fuel (Andriolo, 2015). For the purpose of the study, it is important pointing out the main design differences, some of which might affect the optimal energy structure:

- The thermal power is much larger, being 3.6 GW;
- The inner and outer zones SAs share the same dimensions, the only difference being the fuel enrichment;
- The MOX fraction of the ESFR-WH is lower than in the ESNII+ ASTRID, possibly leading to a softer neutron spectrum;
- The active core is axially enclosed between two steel blankets, while the ESNII+ ASTRID has fertile blankets;
- The sodium plenum above the active zone is 15 cm long, much shorter than in the ESNII+ ASTRID design;
- The considered configuration is in Beginning of Life conditions.

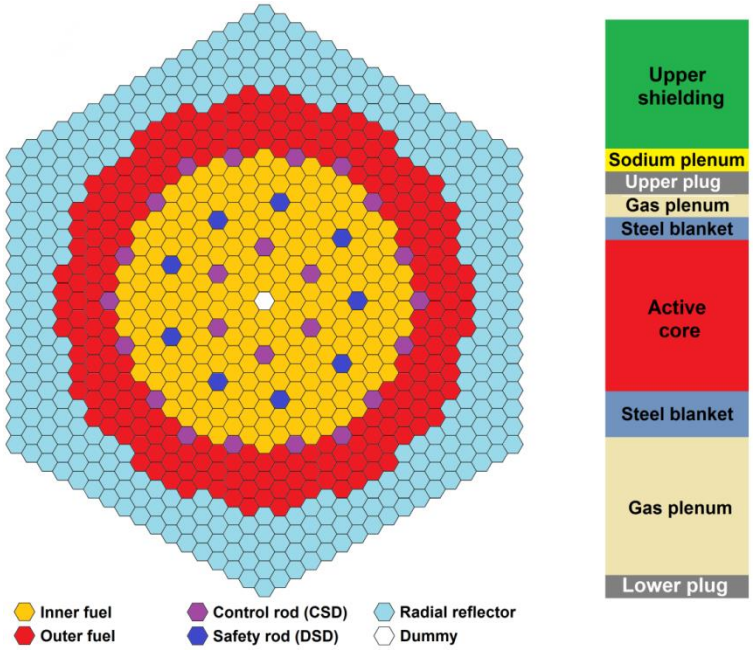

Figure 4.2: ESFR-WH core radial and axial layout (after Fiorini, 2009).

4.2.3 MSFR

The third system chosen for the verification tests is the MSFR, in the version used for the EVOL project (EVOL project, 2011), in the framework of the European Union funding programme FP7. The EVOL project has run between 2011 and 2014 and has been followed by the current project "Safety Assessment of the Molten Salt Fast Reactor" (European Commission - CORDIS, 2017), in the Horizon 2020 framework (European Commission, 2017).

The MSFR is a very peculiar concept, much different from both the ESNII+ ASTRID and the ESFR. The fuel is a eutectic system of LiF and actinide fluorides (AnF_4) in liquid phase which heats up due to fission while passing through an empty cavity (the active core) and is cooled down in the Intermediate Heat Exchangers; the molten salt hence combines both fuel and coolant functions. The core scheme is shown in Figure 4.3. A SIMMER extension has been developed by Wang et al. (2013; 2006) to allow SIMMER dealing with the liquid circulating fuel concept.

A distinctive feature of the MSFR is the thorium-based fuel cycle: the fissile fraction of the fuel salt is a mixture of actinides fluorides, mainly ^{232}Th and ^{233}U; an alternative composition, not considered in the present study, prescribes a mixture of transuranic isotopes as a substitute of the ^{233}U. The system also includes radial fertile blankets to improve the breeding gain, whose composition is the same as the fuel one except for the fissile isotopes, which are all substituted with ^{232}Th. An online reprocessing is envisioned to remove continuously the fission products and separate the bred ^{233}U; on the contrary, minor actinides produced with fission are not extracted and incinerated.

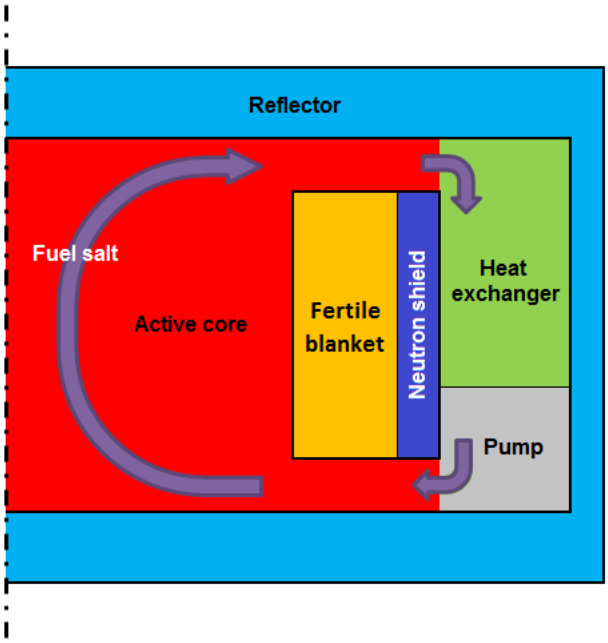

Figure 4.3: MSFR core scheme (after EVOL project, 2011).

The particular nature of the fuel leads to a strong interconnection between neutronics and fluid-dynamics. The fuel temperature, regulated through the pump and the Intermediate Heat Exchanger, can then be used to govern the reactor without control rods need.

4.3 SODIUM-COOLED REACTORS

The first tests of METIS are performed on the ESNII+ ASTRID core, using the *k*-based fitness function f_k. The best 30 solutions found in the 5 tests (2 with unsorted chromosomes and 3 with sorted ones) are depicted in Figure 4.4 and Figure 4.5, showing how groups are subdivided.

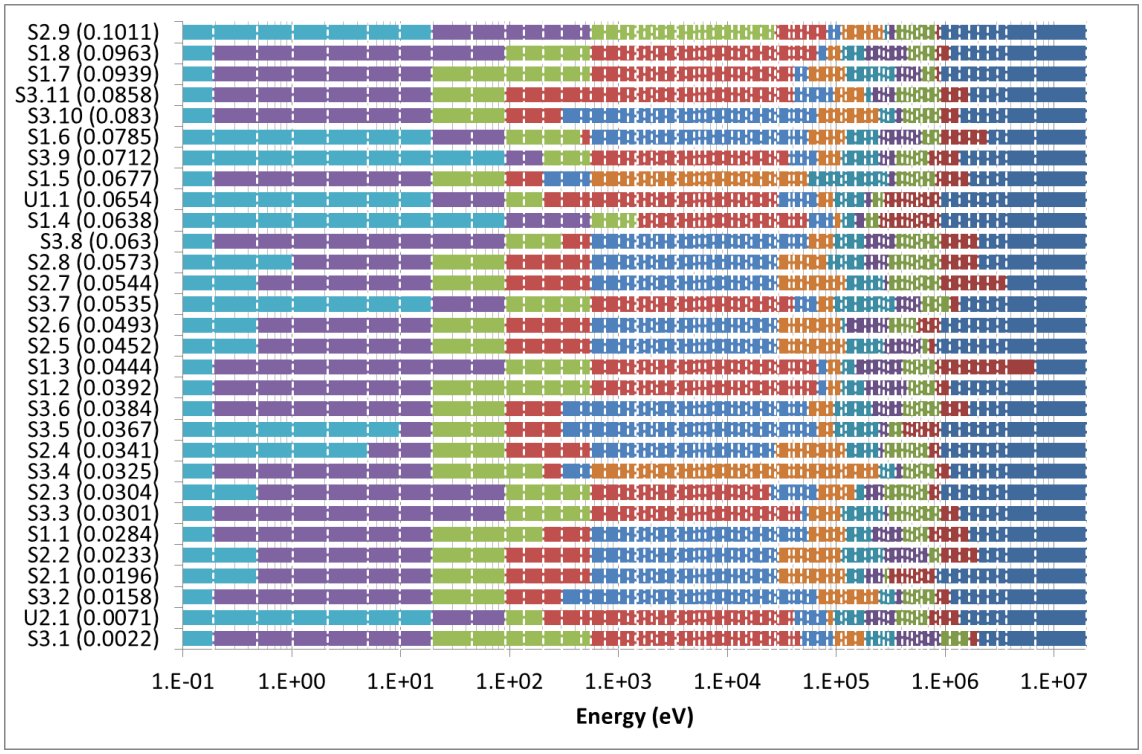

Figure 4.4: Best found energy structures for the ESNII+ ASTRID core associated with calculation run ("S" denotes sorted chromosomes, "U" unsorted ones) and fitness (*k*-based). Dotted lines indicate the energy groups boundaries of the initial libraries; new energy groups are denoted with the same colors.

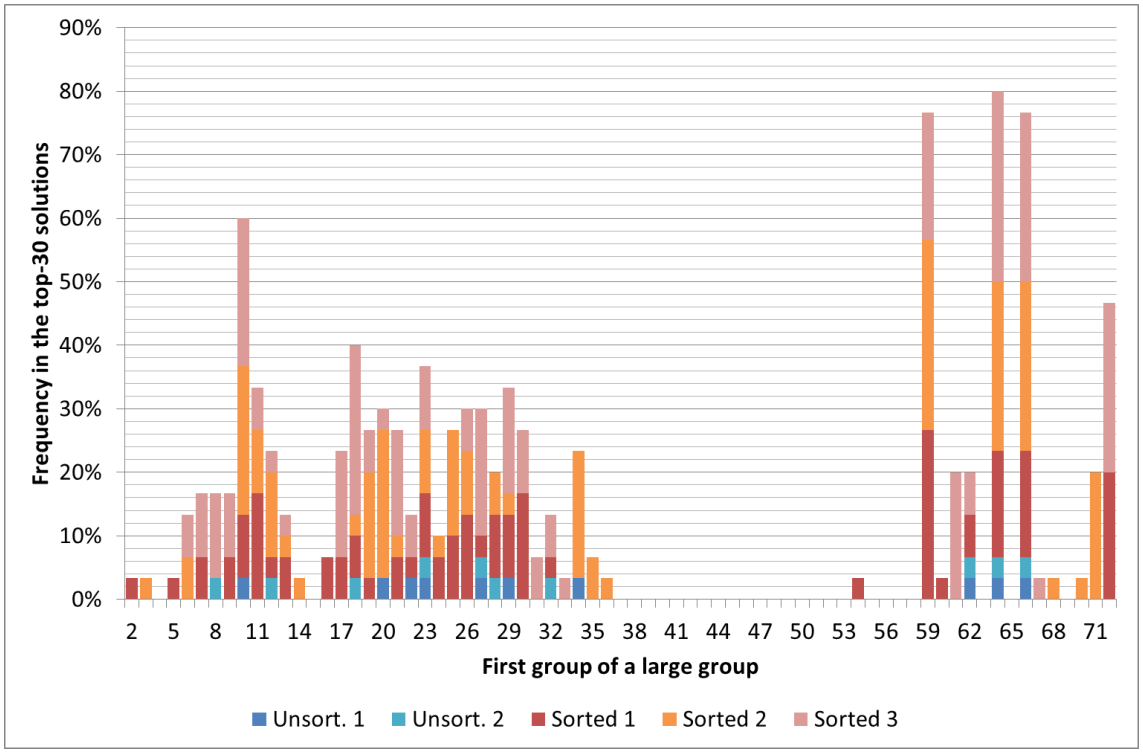

Figure 4.5: Frequency of the energy cuts in the 30 best found meshings for the ESNII+ ASTRID core.

The results show that the algorithm does find solution with a good fitness and that these all share similar patterns: a fast region until ~30 keV with a large number of groups; a zone between ~30 keV and 500 eV modelled with a single group, obtained condensing 25-30 groups; a low energy region with 3-4 groups, with cuts which are placed very frequently at ~550 eV, ~90 eV and ~20 eV. It is interesting comparing such pattern with the XSs profiles and with the neutron spectrum distribution to understand whether the reasons underlying the choices of METIS match with the criteria suggested in literature discussed in §2.4.

As expected, most of the groups are allocated for the energy regions where the neutron flux is high, i.e. in the fast region; this is reasonable as it suggests that solutions which "invest" groups (which are a limited resource for the GA) to describe energy regions with high neutron population (Figure 4.7) are rewarded in terms of fitness function. The starting point of the central region described by a single group corresponds with the first ^{238}U resonances and the group encloses also the whole large sodium absorption peak at 2.85 keV and the resonances of ^{240}Pu (Figure 4.6). The reason of the condensation lies in the fact that the region is largely homogeneous from the XS point of view, characterized by a high absorption, with a low neutron flux; a slight inhomogeneity can be constituted by the fissile isotope ^{239}Pu, whose resonances start from 2.5 keV, but its fission XS is, in the considered energy range, one order of magnitude lower than the absorption one.

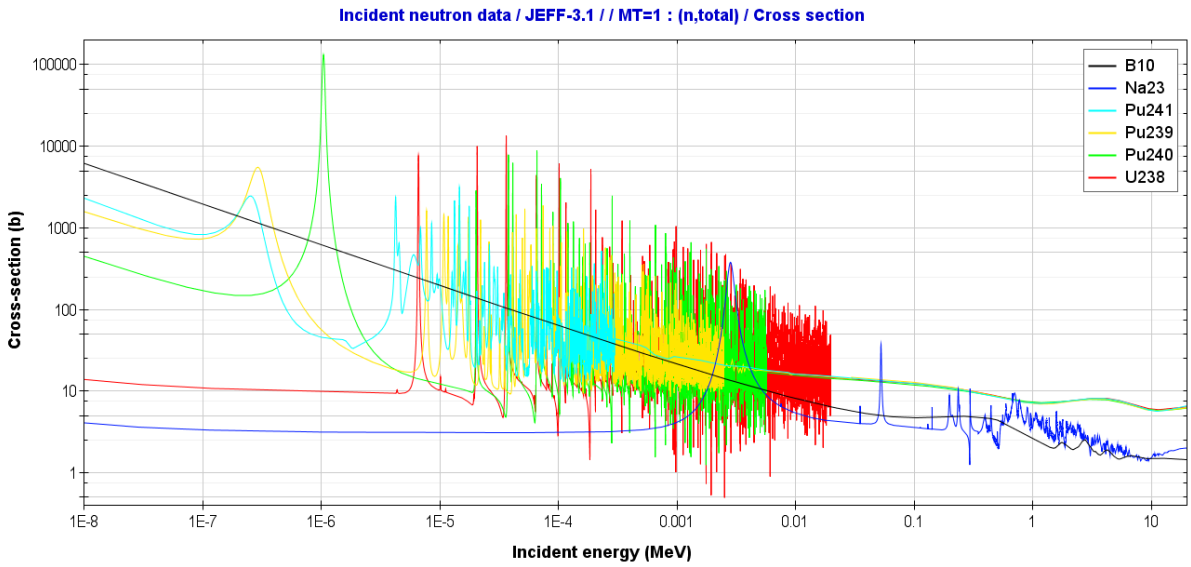

Figure 4.6: Total XSs of some relevant isotopes for the ESNII+ ASTRID core based on the JEFF 3.1 data library (Koning et al., 2006), from JANIS (Soppera et al., 2014).

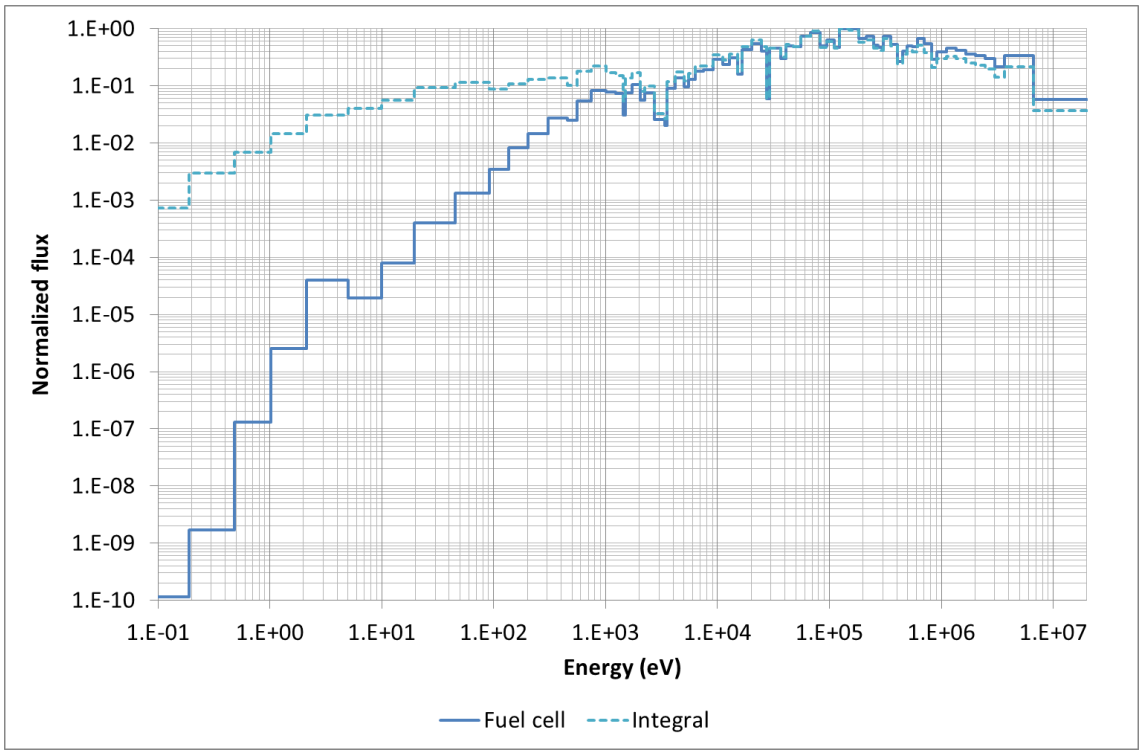

Figure 4.7: Normalized multigroup neutron flux in the ESNII+ ASTRID core calculated with the many-groups libraries.

The presence of a rather detailed energy discretization in the low energy region is more surprising for a fast reactor; however the hypothesis that it is an effect of the genetic drift is not supported by the results as such discretization arises with the same pattern in all performed runs, as shown in Figure 4.5. This suggests that a certain care should be devoted to the

description of the phenomena occurring in the low energy space, which indeed contains the resonances and the high fission XS tail, even with a low neutron population.

The comparison of the XSs corresponding to two of the best structures proposed by the algorithm with those associated with a poor solution, shown in Figures 4.8 and 4.9, also suggest that an appropriate meshing of the low energy region is a relevant point to take into account.

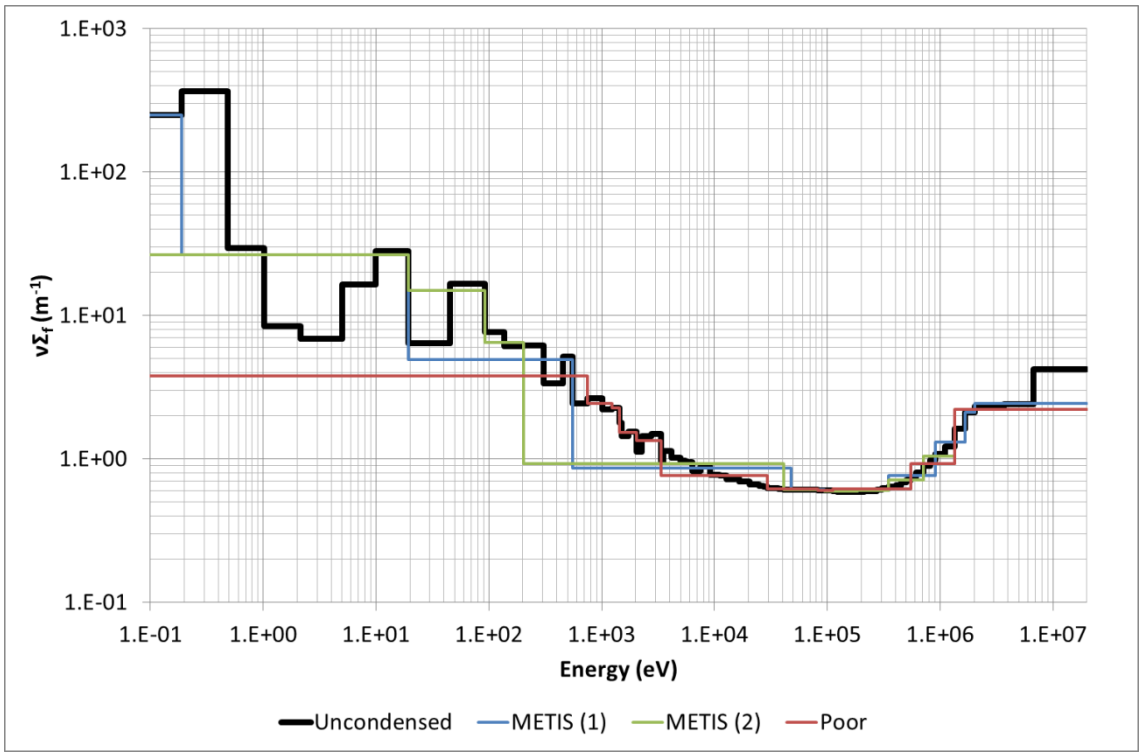

Figure 4.8: Multigroup fission XS (including the yield ν) in a representative fuel cell of ESNII+ ASTRID with both the original libraries and the condensed ones with different energy structures.

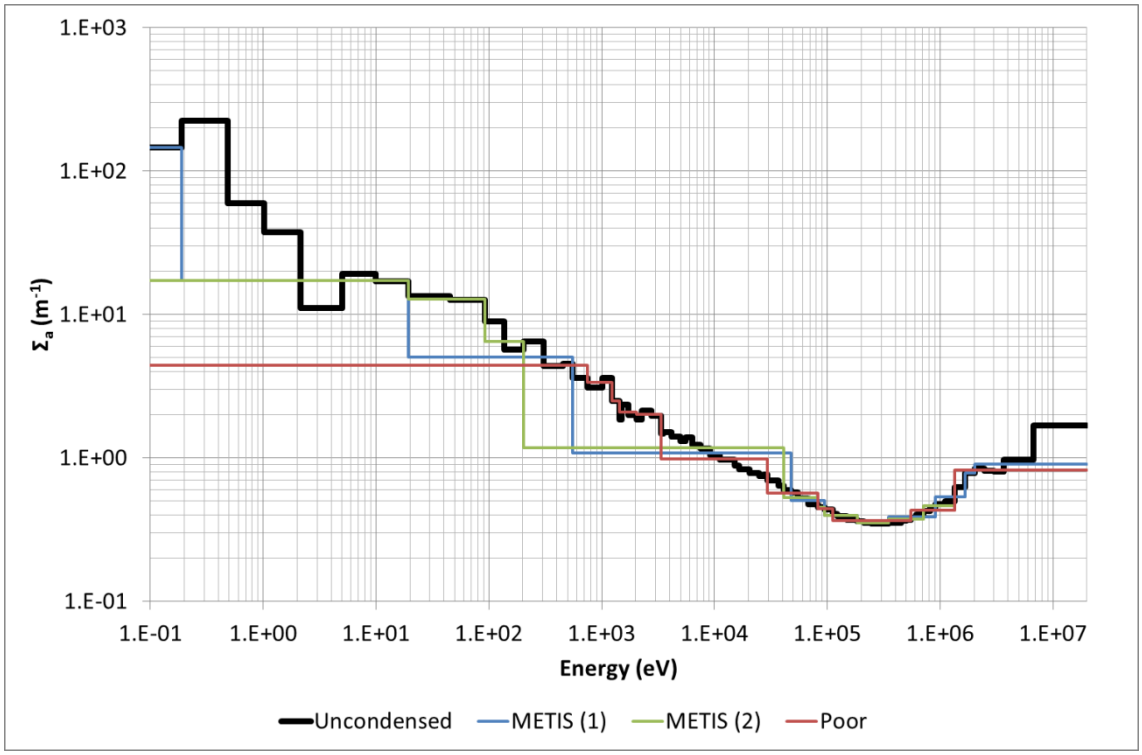

Figure 4.9: Multigroup absorption XS in a representative fuel cell of ESNII+ ASTRID with both the original libraries and the condensed ones with different energy structures.

4.3.1 ESFR

In the framework of the verification process, an effective test is constituted by the comparison of the results with a similar system, like the ESFR; similar results in the two cases would indicate consistency in the choices of the GA.

The neutron spectrum of the ESFR (Figure 4.10) is slightly softer than the ESNII+ ASTRID one; the composition (described in §4.2.2) justifies the difference, due to the lower enrichment of the ESFR fuel and the substitution of the fertile blankets with steel reflectors, much more effective in slowing down the neutrons.

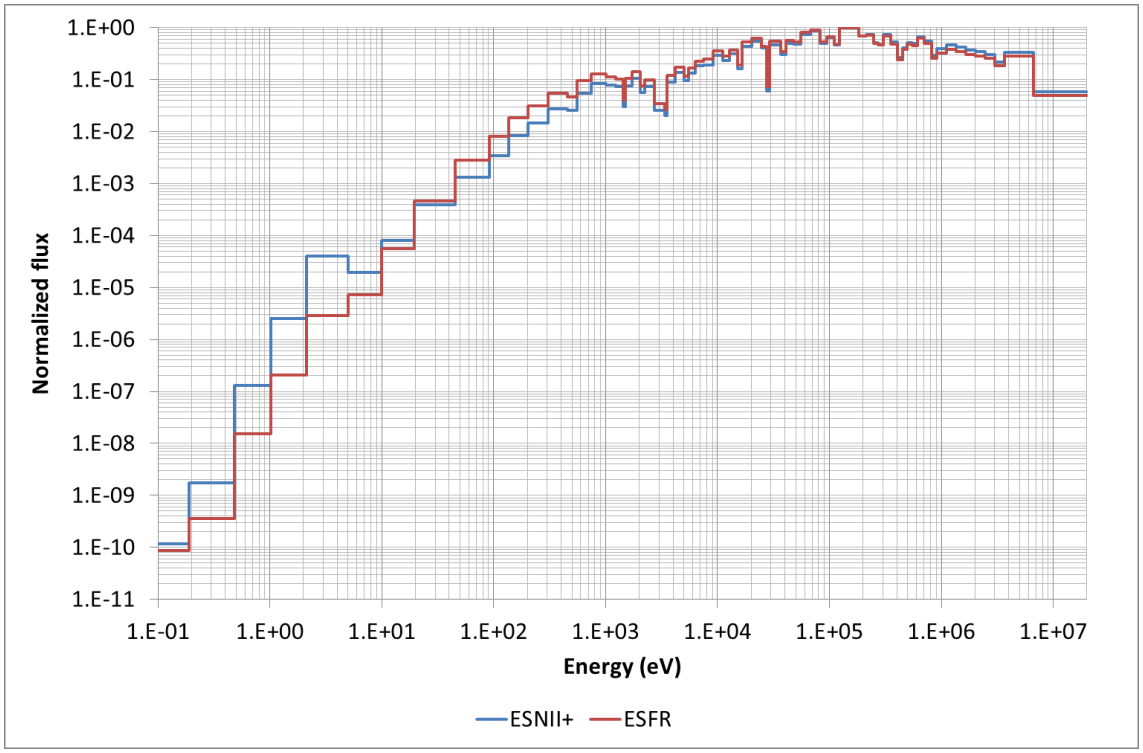

Figure 4.10: Normalized multigroup neutron spectrum in the ESNII+ ASTRID and ESFR cores calculated with the many-groups libraries in representative fuel cells.

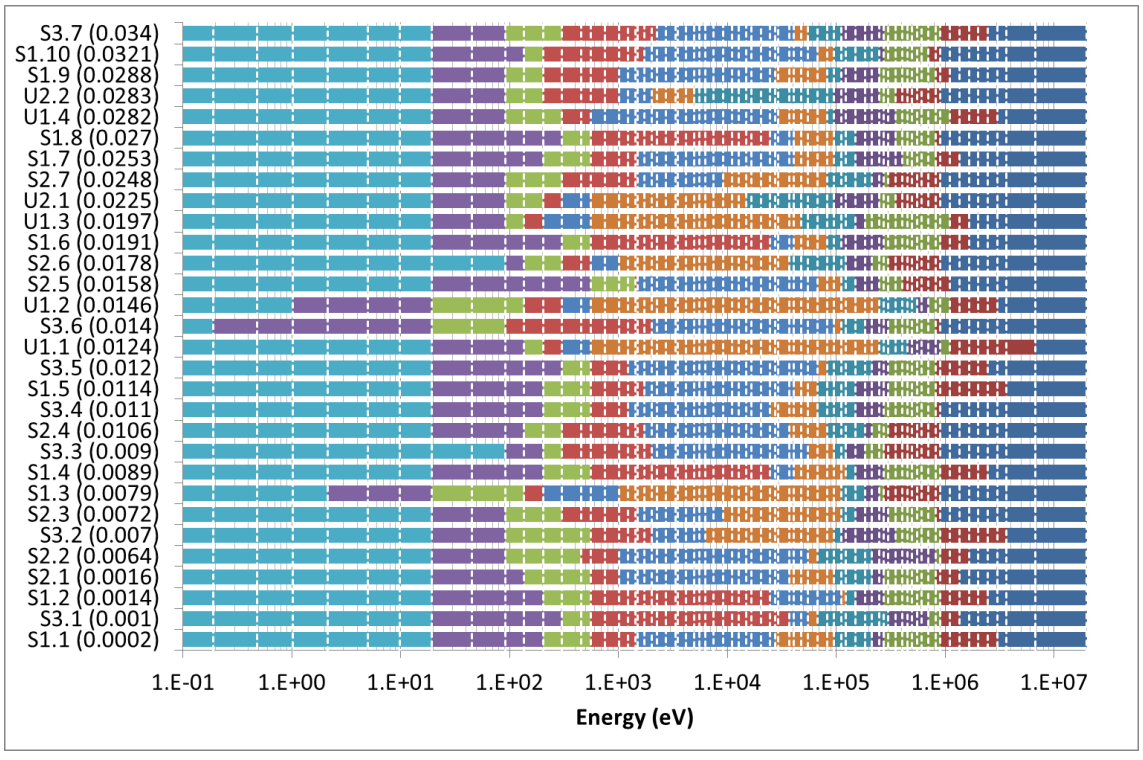

Figure 4.11: Best found energy structures for the ESFR core associated with calculation run ("S" denotes sorted chromosomes, "U" unsorted ones) and fitness (*k*-based). Dotted lines indicate the energy boundaries of the initial libraries; new energy groups are denoted with the same colors.

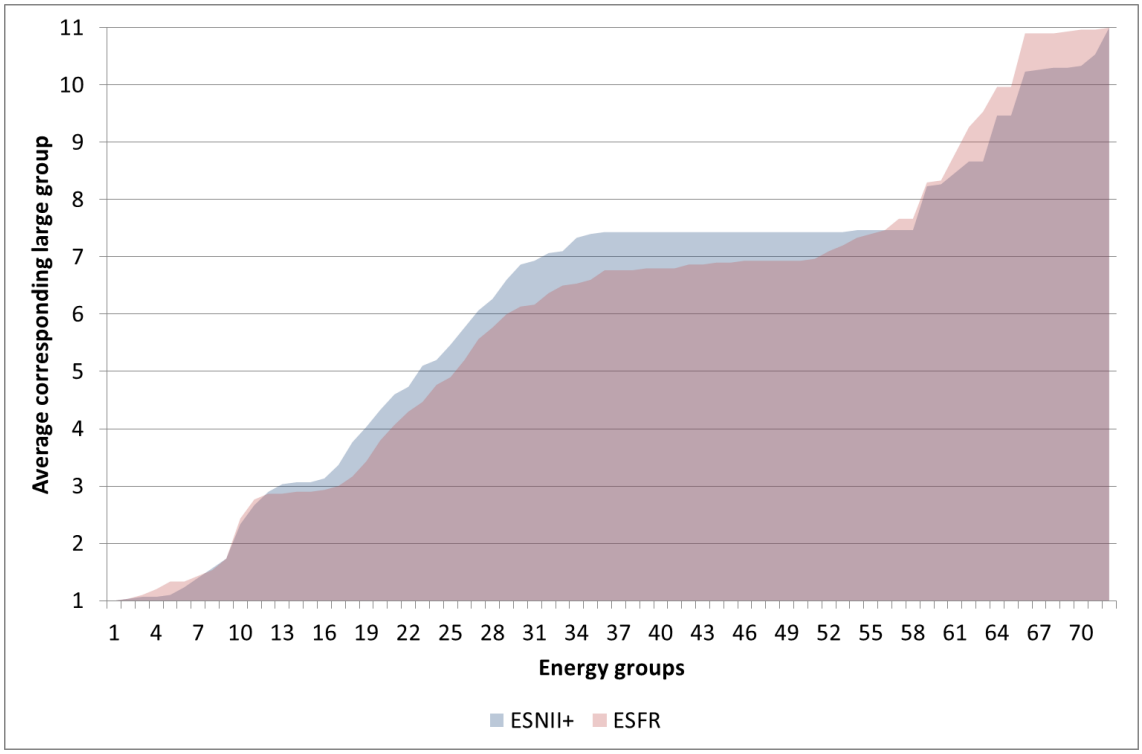

Figure 4.12: Average coarse group corresponding to each fine group for ESNII and ESFR cores (based on the 30 energy structures with the best fitness found).

As expected, ESNII+ (Figure 4.4) and ESFR (Figure 4.11) best energy structures display similar patterns, with a dense energy discretization in the fast region, a central large homogeneous group and a certain attention to the low energy region. From Figure 4.12, showing the coarse group corresponding in average to each fine group, one can draw similar conclusions, as the trends are very close. In addition, one observes that the GA allocates for the ESNII+ core a larger number of groups in the fast region, between the original groups 9 to 30, than for ESFR; for the latter, the spared groups are used for a better description of the low energy zone. This demonstrates the sensitivity of the system to the spectrum variation, with a softer core needing better discretization in the low energy region and vice versa.

4.4 THE MSFR CASE

After considering two SFRs, one would like to test the tool on a different system. The METIS algorithm is hence applied to the EVOL MSFR.

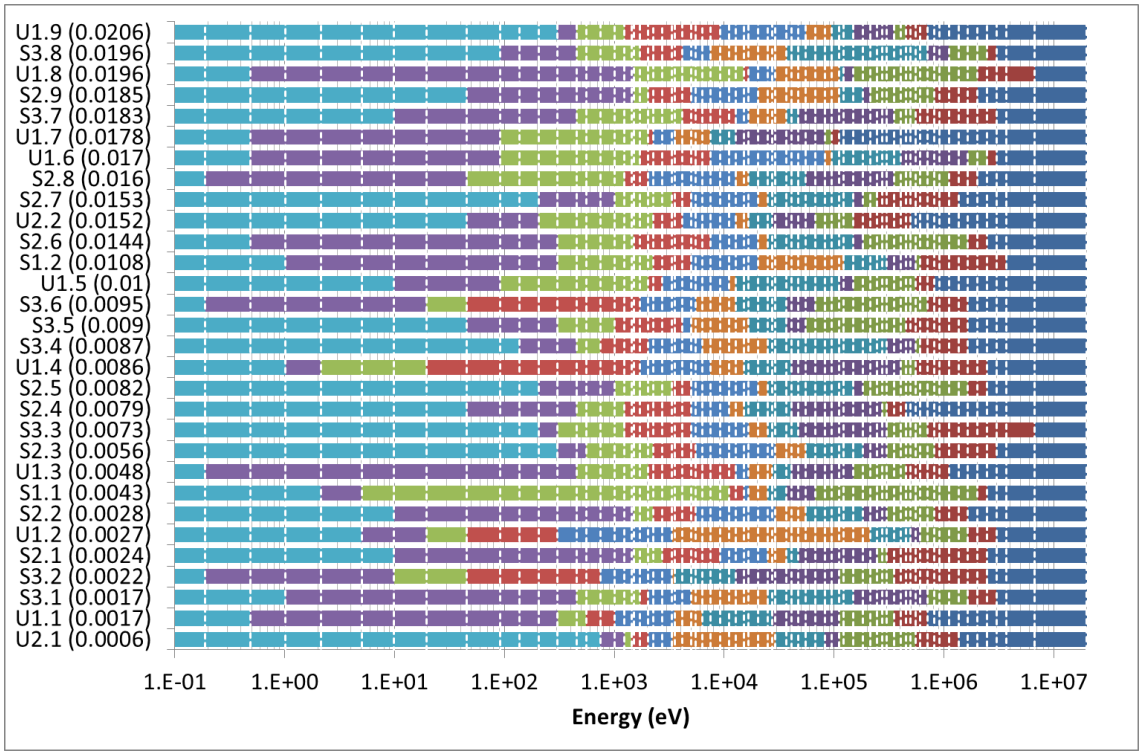

Figure 4.13: Best found energy structures for the MSFR core associated with calculation run ("S" denotes sorted chromosomes, "U" unsorted ones) and fitness (*k*-based). Dotted lines indicate the energy boundaries of the initial libraries; new energy groups are denoted with the same colors.

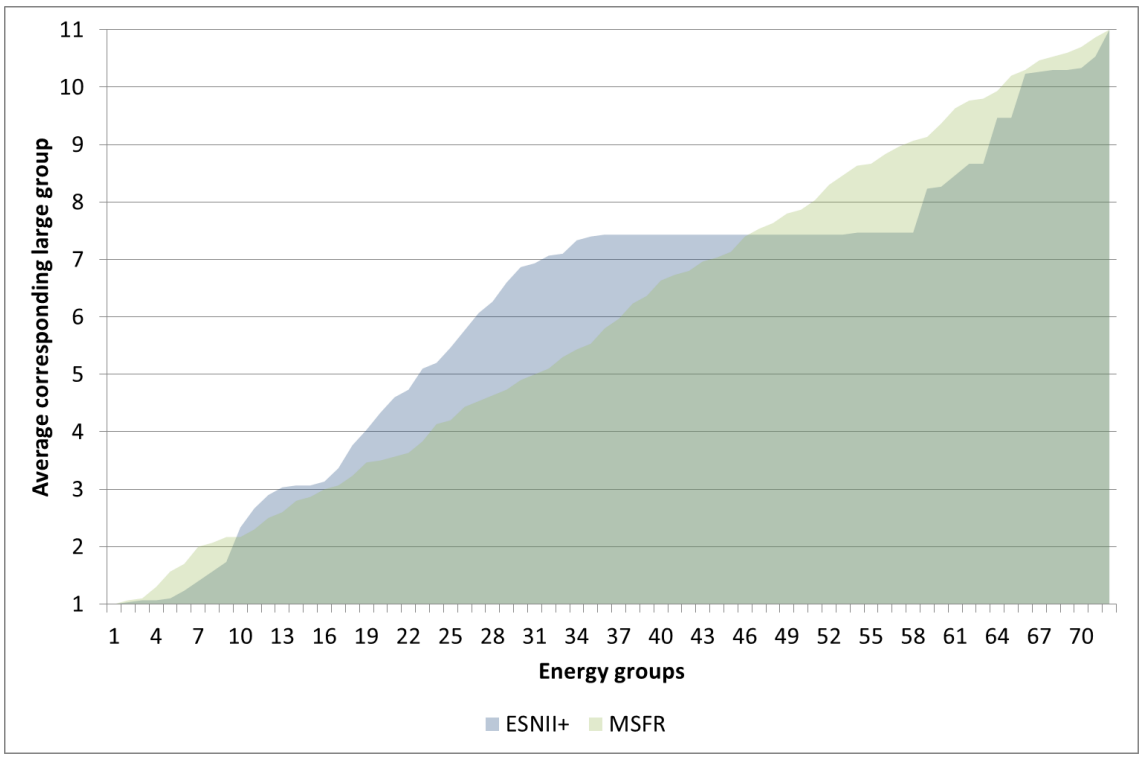

Figure 4.14: Average coarse group corresponding to each fine group for ESNII+ and MSFR cores (based on the 30 energy structures with the best fitness found).

The clear pattern visible in Figure 4.4 (ESNII+) and Figure 4.11 (ESFR) cannot be identified in this case (Figure 4.13 and Figure 4.14): all cuts seem to have the same relevance and the discretization effect on the *k* correctness appears to be small. Further support to the hypothesis that the influence of energy structures on the MSFR is limited is provided by the Figure 3.12 and Table 4.2.

Table 4.2: Average number of fine groups in each coarse group with standard deviation (on the 30 energy structures with the best fitness found) (Massone et al., 2017a).

	ESNII+ ASTRID	ESFR	MSFR
1	7.0 ± 2.2	6.4 ± 2.7	6.3 ± 5.0
2	3.9 ± 2.8	5.1 ± 3.0	5.8 ± 3.8
3	5.3 ± 2.5	6.3 ± 3.6	7.7 ± 5.9
4	3.9 ± 2.6	4.4 ± 2.5	6.5 ± 4.6
5	4.1 ± 2.3	4.9 ± 3.8	7.4 ± 4.7
6	6.8 ± 7.8	10.3 ± 11.1	5.5 ± 5.6
7	14.5 ± 12.8	14.0 ± 9.5	7.3 ± 3.7
8	14.2 ± 12.4	7.8 ± 7.8	6.3 ± 3.9
9	4.1 ± 4.1	2.6 ± 1.0	7.0 ± 5.5
10	5.1 ± 2.1	3.3 ± 1.4	6.2 ± 4.3
11	3.1 ± 2.8	6.7 ± 1.5	6.0 ± 4.1

The former shows that the average fitness of the initial population, i.e. a group of randomly initialized solutions, is already very low (in the order of 50) with respect to the SFR cases; in addition it improves slowly as the generations go on. On the other hand the low average fitness cannot be due to homogenization of the population, as it occurs from the beginning, so even a refinement of the input parameters or an adaptive scheme could not help.

Finally, Table 4.2 shows that all coarse groups in the MSFR case have a similar width with large standard deviation[1]; on the contrary, the SFRs display groups with different widths, justified by the problem physics, and small standard deviations, meaning that the group pattern of all best

[1] In this thesis standard deviation must be always considered as the corrected sample standard deviation:

$$\sigma = \sqrt{\frac{1}{N-1}\sum_{i=1}^{N}(x_i - \bar{x})^2}$$

solutions is very similar. Only for groups 6 to 8 the variance is large, but this is due to the fact that the large central group (see §4.3) does not always correspond to the same group.

4.4.1 THE MODIFIED ASTRID

Once ascertained the peculiar behaviour of the MSFR, which does not respond to energy structure variations, one should try to understand what feature is the cause. To do so, one performs tests on the ESNII+ core, on which the genetic algorithm has already been proven working, modifying it with the introduction of the biggest peculiarities of the MSFR: homogeneity and absence of control material. This results in 4 cases:

- The reference case, described in §4.3;
- A homogeneous case, composed by a homogeneous mixture of all materials in the core of the reference core;
- An "uncontrolled" core, heterogeneous as the reference but with all control material (boron carbide) removed;
- A homogeneous "uncontrolled" case, combining the previous two.

With the obvious exception of the reference, not all cases can achieve criticality, making the following tests pure speculation, however useful to understand some aspects of the GA convergence.

Analysing the neutron spectra of the modified ASTRID cores, shown in Figure 4.15, one can understand the effects of the changes, and better interpret the results in Figure 4.16.

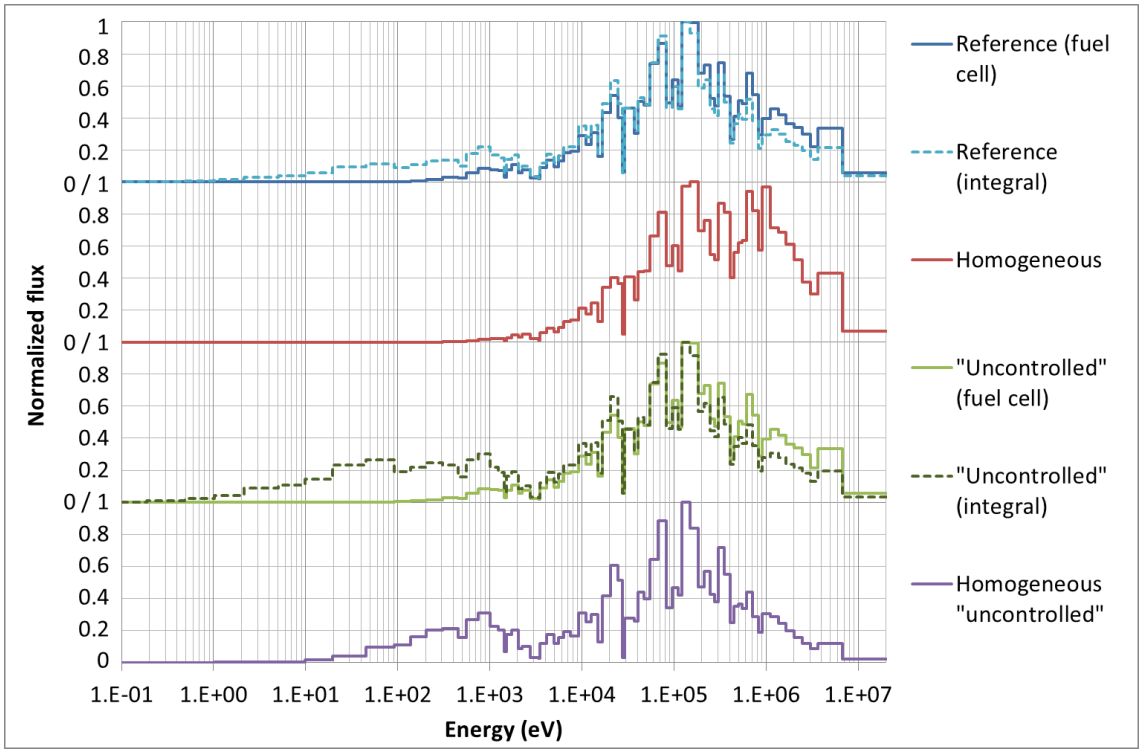

Figure 4.15: Neutron spectra of the modified ASTRID cores (after Massone et al., 2017a).

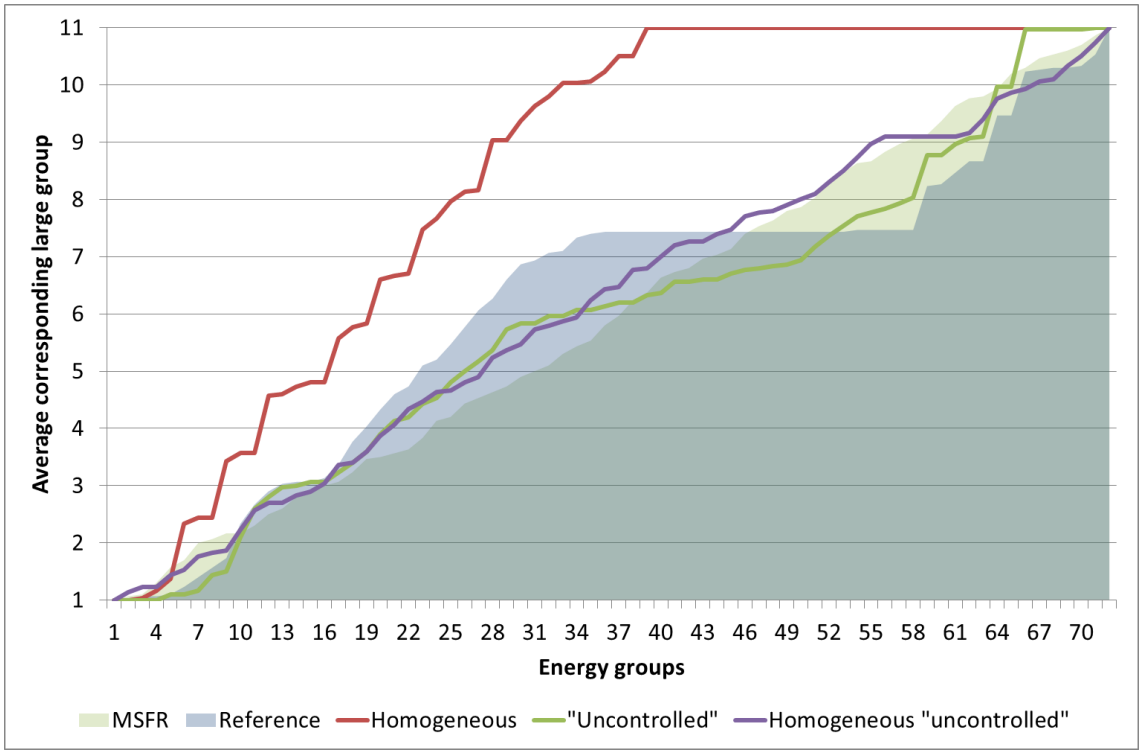

Figure 4.16: Average coarse group corresponding to each fine group for the modified ESNII+ cases (based on the 30 energy structures with the best fitness found).

The behavior of the GA in the homogeneous case could be easily predicted: the control material is mainly ^{10}B which is extremely effective with low energy neutrons but fairly transparent to fast

ones (Figure 4.6). As a consequence most of the neutrons whose energy falls below the ^{10}B effectiveness limit are quickly removed and the low energy tail of the neutron spectrum, which justified the use of some groups to detail that space, does not exist in this case. This explains why all best energy structures found focus on the first 40 groups, condensing all groups below 10 keV together: there is no gain in spending resources, i.e. groups, to describe energy regions which are almost empty.

The "uncontrolled" heterogeneous case is the one which better follows the reference one, showing similar behaviors and energy cuts in both fast and low-energy regions. On the contrary, the main differences appear in the intermediate zone, between 400 keV and 500 eV: with respect to the reference case, more groups have to be allocated to the low energy zone, which in this case has many neutrons (Figure 4.15) and so must be adequately described; as the number of groups to be set is fixed, less groups are used for the faster region. The reference case displayed a large plateau in Figure 4.16, indicating a strong tendency to condense all groups between 35 and 57 in a single one (as explained in §4.3); such an effect is less evident in the "uncontrolled" case, yet one can notice that the slope of the curve in Figure 4.16 is lower between groups 29 and 50, matching the energy region where both the neutron spectrum is depressed in both fuel and non-fuel cells.

The case combining the two modifications is the one which best matches with the MSFR trend, though the neutron spectrum is not very different from the reference configuration. The results follow very well the trend of the "uncontrolled" heterogeneous configuration in the region before the 24th group, where the neutron spectra are very similar; afterwards, the combined case can afford spending more groups than the heterogeneous one, which has to use them for the low-energy tail.

A very interesting effect can be observed in the trend of the average fitness along the generations, in Figure 4.17. One notices that the low initial fitness, already observed for the MSFR in Figure 3.12, is a feature common to all homogeneous systems. The absence of the control material has also an effect, as it raises the initial fitness, but it is minor with respect to homogeneity.

One can see that the initial fitness is a measure of the problem difficulty: if most of the initial randomly generated solutions have small fitness values, i.e. are good solutions of the problem, one can suppose that it is very likely to find acceptable energy structures in the solution space, or conversely that many of the possible meshings are acceptable as solutions. On the contrary, if the initial average fitness is large and acceptable solutions can be found only after many steps, one can presume that good options are rare in the energy structure space.

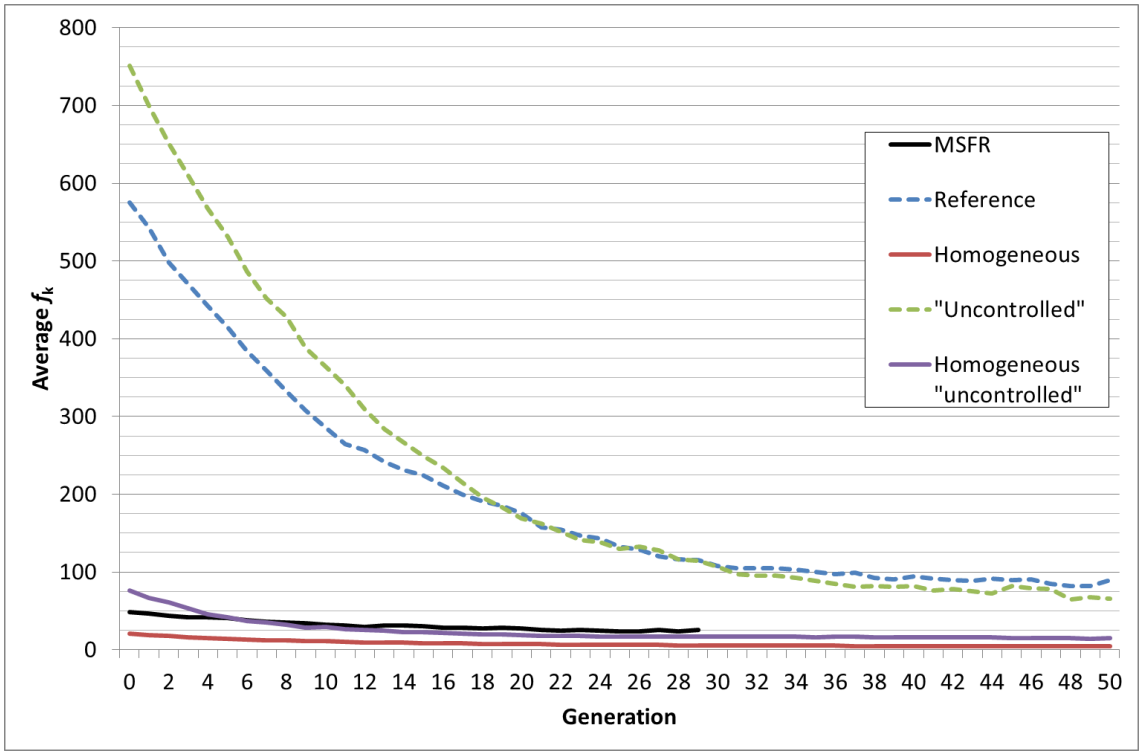

Figure 4.17: Average fitness convergence for MSFR and ESNII+ different configurations. Only sorted chromosomes are used. Dotted lines denote heterogeneous cores.

Clearly, satisfying the constraints of a heterogeneous system is much more demanding than for a homogeneous one; in fact, in the latter the phenomena occurring are the same everywhere, so one has to face optimization of the structure for a single cell. On the contrary, when the system is heterogeneous, the GA has to balance the issues of many different cells, each with its own XSs and neutron spectrum; doing this is much more challenging and even the optimal solution could be just a compromise among the cells needs.

The effect of the control material is similar: when the boron is removed, the span of the neutron spectrum is extended, as the absorption of the low energy neutrons is much reduced. This means that the GA has to fulfil additional requirements to obtain an acceptable energy meshing, i.e. the problem is more difficult. This explains the fact that "uncontrolled" configurations, both homogeneous and heterogeneous, have higher initial fitness values than their counterparts with boron.

The consequence of the good solution rarity is that the GA converges to one of them, when it finds it, without being "distracted" by other equally performing solutions (as they do not exist or are not found); hence resulting structures show clearly recognizable patterns. On the contrary, when finding good solutions is easy, i.e. the constraints are very relaxed, the GA retains different valid options, often very different from each other, without converging to any of them. This explains the absence of patterns when observing the best solutions.

4.5 FEEDBACK COEFFICIENTS

When dealing with safety analyses of nuclear reactors, the feedback coefficients are of paramount importance and it is essential for the correct representation of the transient that the few-groups libraries can correctly predict their values.

The void feedback coefficient F_v measures the reactivity variation in the event of core voiding, i.e. when the sodium coolant is removed, and can be expressed in pcm as

$$F_v \triangleq (\rho_{void} - \rho_{ref}) \cdot 10^5 = \frac{k_{void} - k_{ref}}{k_{void} \cdot k_{ref}} \cdot 10^5. \quad \textbf{(4.1)}$$

where k_{void} is the multiplication coefficient of the system with the coolant removed. This value, usually expressed in pcm, is usually negative in thermal reactors and positive in SFRs.

Similarly, the Doppler (or fuel temperature) feedback coefficient K_D (Waltar and Reynolds, 1981, pp. 196–203) describes the reactivity change in pcm relative to fuel temperature variation due to Doppler effect:

$$K_D = \frac{k_{T+1000\,K} - k_{ref}}{\ln \frac{T_{T+1000\,K}}{T_{ref}}} \cdot 10^5. \quad \textbf{(4.2)}$$

where the "T+1000 K" configuration is obtained from the reference system increasing the fuel temperature by 1000 K.

One could, in principle, modify the GA fitness function to find the energy structure with the best feedback coefficient match, but this would require two solutions of the eigenvalue problem for each tested individual and feedback coefficient, one for the reference condition and one for each modified configuration, with a consequent increase of the computational time. In addition, deep modifications to the SIMMER code would be required to allow support of more than one geometry at the same time. It is however interesting studying the reliability of the feedback coefficients calculated with the current fitness f_k.

The test system is the ESNII+ ASTRID core, already described in §4.2.1; the voided configuration is obtained by removing the cooling sodium from all fuel zones, excluding the lower fertile zone. Only the coolant inside the SA wrapper is removed, while the inter-SA sodium remains in place. As reference results are considered those calculated using the uncollapsed many-groups libraries, and they are compared in Table 4.3 with those obtained using the best energy structures found. Two structures are taken into account: they are optimized by METIS, one on

the reference system, the other on the voided geometry. In Table 4.4, instead, the best found meshings are those found with each of the 3 test system described before.

Table 4.3: ESNII+ feedback coefficients (Massone et al., 2017b).

	Uncollapsed libraries	**Best found energy structure (Reference config.)**		**Best found energy structure (Voided config.)**	
	k	***k***	**Δ (pcm)**	***k***	**Δ (pcm)**
Reference	*0.99919*	*0.99920*	+1	*0.99932*	+13
Void	*1.00995*	*1.00980*	−15	*1.00996*	+1
T+1000 K	*0.99633*	*0.99651*	+18	*0.99669*	+36
F_v (pcm)	+1066	+1051	−−−	+1054	−−−
K_D (pcm)	−560	−527	−−−	−515	−−−

Table 4.4: ESNII+ feedback coefficients with other reactors best structures (Massone et al., 2017a).

	Uncollapsed libraries	**Best found energy structure (ESNII+)**		**Best found energy structure (ESFR)**		**Best found energy structure (MSFR)**	
	k	***k***	**Δ (pcm)**	***k***	**Δ (pcm)**	***k***	**Δ (pcm)**
Reference	0.99919	0.99920	+1	0.99880	−39	0.99462	−460
Void	1.00995	1.00980	−15	1.00950	−44	1.00509	−479
T+1000 K	0.99633	0.99651	+18	0.99599	−34	0.99180	−458
F_v (pcm)	+1066	+1051	−−−	+1061	−−−	+1047	−−−
K_D (pcm)	−560	−527	−−−	−550	−−−	−552	−−−

Results in Table 4.3 show that, even if the fitness function is based on the multiplication coefficient, the feedback coefficients are fully in agreement with the reference values. This suggests that the transient calculation, even in accidental conditions, is expected to return reliable results. A *caveat* however comes from Table 4.4: the optimal energy structure does depend on the core geometry and composition, and its applicability deteriorates as one moves further from the original core configuration; that is why the best meshing for the ESFR, which is similar to ESNII+, performs well, while the MSFR structure is totally inadequate.

The reactor transient can be considered, in practice, as a sequence of similar reactors: the use of a single energy discretization is hence justified. Nevertheless, as the transient progresses (maybe with core disruption, if one is studying an accidental behaviour) the core conditions drift apart from the initial ones, based on which the energy structure has been determined; if the

distance becomes too large the calculated energy meshing could be no more adequate, and a new execution of the GA should be considered.

4.6 REACTION RATES

A possible way to verify the applicability of the energy structure is the comparison of the reaction rates obtained with the XS collapsing and the reference ones, calculated with the uncollapsed many-groups libraries.

As described in §2.3, the condensed XSs are calculated with the objective of keeping the reaction rates constant before and after the collapsing procedure. Yet, the perfect match cannot be assured: in fact one should know the correct transport equation solution in advance to obtain the correct XSs. As this is not an option, one had to introduce different approximations (detailed in §2.2) in the collapsing procedure, the most relevant being the fact that the weighting spectrum is not the correct flux but its approximation, solution of eq. (3.9).

Table 4.5 shows the comparison of the reaction rates in the ESNII+ core obtained with 3 different energy structures calculated by METIS, two based on the correct system and one on the MSFR, with the theoretically expected results

$$RR_{x,\mathrm{th}}^{(G)} = \sum_{\forall g \in G} RR_x^{(g)} \tag{4.3}$$

where $RR_x^{(g)}$ are those calculated with the uncollapsed many-groups libraries.

Table 4.5: ESNII+ fission and absorption reaction rates in a fuel cell with different energy structures (Massone et al., 2017a).

ESNII+ energy structure (1)			**ESNII+ energy structure (2)**			**MSFR energy structure**		
Δk = +1 pcm			Δk = +1 pcm			Δk = −460 pcm		
Upper energy (eV)	$RR_{x,th}$ **(m^{-3} s^{-1})**	$RR_{x,11g}$ **(m^{-3} s^{-1})**	**Upper energy (eV)**	$RR_{x,th}$ **(m^{-3} s^{-1})**	$RR_{x,11g}$ **(m^{-3} s^{-1})**	**Upper energy (eV)**	$RR_{x,th}$ **(m^{-3} s^{-1})**	$RR_{x,11g}$ **(m^{-3} s^{-1})**
Fission								
2.00E+07	4.17E+18	4.18E+18	*2.00E+07*	6.17E+18	6.18E+18	*2.00E+07*	6.17E+18	6.19E+18
2.02E+06	1.06E+18	1.07E+18	*1.35E+06*	2.43E+18	2.42E+18	*1.35E+06*	3.68E+18	3.63E+18
1.65E+06	2.31E+18	2.34E+18	*7.07E+05*	2.85E+18	2.89E+18	*5.50E+05*	6.25E+18	6.17E+18
9.07E+05	3.92E+18	3.93E+18	*3.51E+05*	2.64E+18	2.60E+18	*1.11E+05*	9.40E+17	9.64E+17
3.51E+05	2.64E+18	2.61E+18	*1.83E+05*	2.54E+18	2.54E+18	*8.23E+04*	2.84E+18	2.88E+18
1.83E+05	2.54E+18	2.55E+18	*9.48E+04*	4.11E+17	4.20E+17	*2.93E+04*	3.50E+18	3.60E+18
9.48E+04	2.17E+18	2.19E+18	*8.23E+04*	2.18E+18	2.19E+18	*3.35E+03*	3.03E+17	3.05E+17
4.75E+04	6.47E+18	6.47E+18	*4.09E+04*	6.62E+18	6.49E+18	*2.03E+03*	4.81E+17	4.89E+17
5.55E+02	8.34E+17	8.53E+17	*2.04E+02*	1.82E+17	2.17E+17	*1.43E+03*	2.53E+17	2.52E+17
1.95E+01	1.49E+16	3.41E+16	*9.17E+01*	7.29E+16	1.18E+17	*1.23E+03*	6.21E+17	6.33E+17
1.89E-01	6.38E+10	3.49E+10	*1.95E+01*	1.49E+16	2.95E+16	*7.49E+02*	1.07E+18	1.10E+18
Overall	2.61E+19	2.62E+19	**Overall**	2.61E+19	2.61E+19	**Overall**	2.61E+19	2.62E+19
Absorption								
2.00E+07	1.54E+18	1.55E+18	*2.00E+07*	2.30E+18	2.31E+18	*2.00E+07*	2.30E+18	2.31E+18
2.02E+06	3.96E+17	3.99E+17	*1.35E+06*	1.08E+18	1.07E+18	*1.35E+06*	1.71E+18	1.69E+18
1.65E+06	9.41E+17	9.53E+17	*7.07E+05*	1.49E+18	1.51E+18	*5.50E+05*	3.71E+18	3.67E+18
9.07E+05	1.99E+18	2.00E+18	*3.51E+05*	1.54E+18	1.52E+18	*1.11E+05*	6.89E+17	7.07E+17
3.51E+05	1.54E+18	1.53E+18	*1.83E+05*	1.70E+18	1.70E+18	*8.23E+04*	2.61E+18	2.65E+18
1.83E+05	1.70E+18	1.71E+18	*9.48E+04*	3.06E+17	3.12E+17	*2.93E+04*	4.51E+18	4.64E+18
9.48E+04	1.79E+18	1.81E+18	*8.23E+04*	1.90E+18	1.90E+18	*3.35E+03*	4.57E+17	4.60E+17
4.75E+04	8.20E+18	8.19E+18	*4.09E+04*	8.40E+18	8.27E+18	*2.03E+03*	6.56E+17	6.67E+17
5.55E+02	8.65E+17	8.83E+17	*2.04E+02*	1.85E+17	2.17E+17	*1.43E+03*	2.76E+17	2.75E+17
1.95E+01	1.24E+16	2.22E+16	*9.17E+01*	6.85E+16	1.00E+17	*1.23E+03*	8.49E+17	8.72E+17
1.89E−01	3.76E+10	2.06E+10	*1.95E+01*	1.24E+16	1.92E+16	*7.49E+02*	1.21E+18	1.28E+18
Overall	1.90E+19	1.90E+19	**Overall**	1.90E+19	1.89E+19	**Overall**	1.90E+19	1.92E+19

The results show that the XS collapsing tool does calculate the adequate collapsed XSs. In fact the reaction rates relative error in each group is generally small, with the exception of the lower energy groups, where the neutron flux, and so the reaction rates, is small in absolute value.

However, one notices that the relative error in each group does not represent a good measure of the energy structure adequacy: in fact, the best case under this point of view is the MSFR one, which however underestimates the multiplication coefficient by 460 pcm. This is due to the fact that the chosen meshing induces an overestimation of the total absorptions by 1.2%, which is not compensated by the fissions, which are just 0.3% more than expected; for comparison, the other two cases have, respectively, +0.3% (absorptions) with +0.4% (fissions) and -0.2%/-0.1%.

The balance between the reaction rates does not appear to be the only important issue. As one can see in Figure 4.18, the absolute value of the reaction rates discrepancy is particularly small for the ESNII+ cases, while it is very high with the MSFR structure, especially for the higher energy groups, which affect more the neutron balance in a fast reactor.

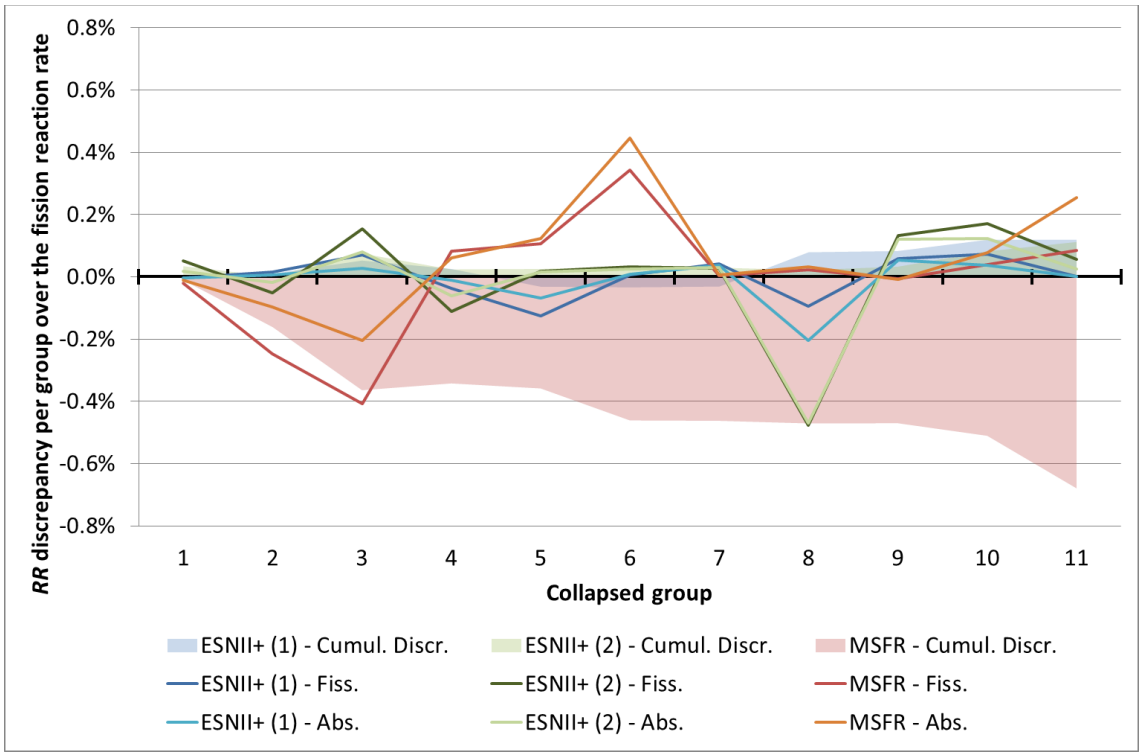

Figure 4.18: Reaction rate discrepancy per group with different energy structures and cumulated discrepancy in fission/absorption difference.

4.7 FITNESS FUNCTIONS

Up to this point, only one of the 3 fitness functions introduced in §3.4.2 has been tested. In order to check the applicability of the other 2 proposed fitness functions, METIS has been run 5 times on the ESNII+ ASTRID core with each function; all other options are the same for all cases. The

best energy structures are compared in terms of multiplication and feedback coefficients match; results are shown in Table 4.6 for each calculation and in average in Figure 4.19.

Table 4.6: ESNII+ feedback coefficients with different fitness functions (Massone et al., 2017c).

Case	Value			Δ		
	k	F_v (pcm)	K_D (pcm)	k (pcm)	F_v (pcm)	K_D (pcm)
Reference	0.99919	+1066	-560	---	---	---
f_k						
Test 1	0.99919	+1055	−523	0	−11	+37
Test 2	0.99918	+1039	−534	−1	−27	+25
Test 3	0.99918	+1039	−534	−1	−27	+25
Test 4	0.99919	+1057	−546	0	−9	+14
Test 5	0.99918	+1053	−534	−1	−14	+25
f_{comb}						
Test 6	0.99919	+1054	−552	0	-13	+8
Test 7	0.99920	+1072	−548	+1	+6	+12
Test 8	0.99920	+1072	−548	+1	+6	+12
Test 9	0.99919	+1053	−525	0	−14	+35
Test 10	0.99919	+1054	−525	0	−13	+35
f_Φ						
Test 11	0.99697	+1013	−468	−223	−53	+92
Test 12	0.99403	+1102	−507	−520	+36	+53
Test 13	0.99798	+1047	−550	−121	−19	+10
Test 14	0.99919	+1149	−534	0	+82	+25
Test 15	0.99734	+1014	−460	−186	−52	+100

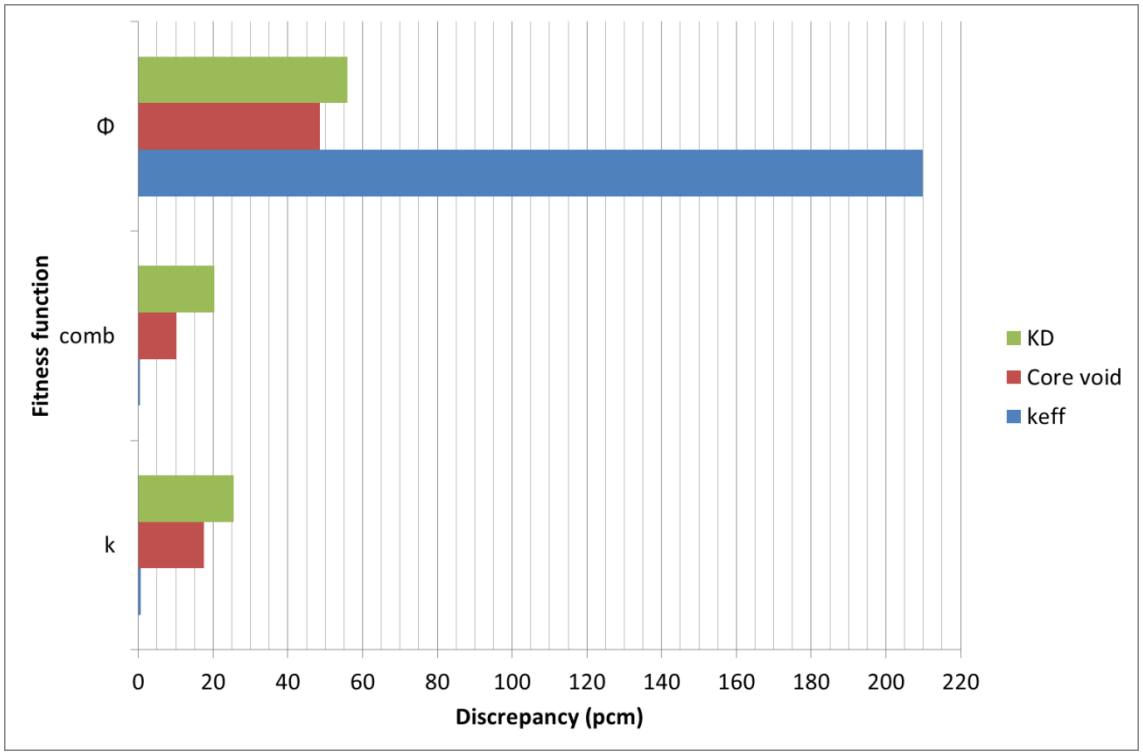

Figure 4.19: Average discrepancy on multiplication and feedback coefficients in ESNII+ core with different fitness functions (after Massone et al., 2017c).

Table 4.6 demonstrates that the combined fitness function predicts the values in the same range of the *k*-based one, all within acceptability limit: hence, the combined fitness function is safe to use, i.e. it is not expected to return structures unable to reproduce the correct coefficients, and so the correct transient. Moreover, Figure 4.19 shows that the *k*-based fitness function performs slightly better, in average, when it is combined with the flux-criterion.

The latter, on the contrary, is completely unreliable when it is applied alone: out of the 5 tests shown in Table 4.6 the multiplication coefficient could be correctly estimated only once, though with an overestimated void feedback coefficient. The most concerning issue, however, is the unreliability rather than the ineffectiveness: the correctness degree of the energy structure appears to be extremely volatile, with the discrepancy peaking to 500 pcm for the multiplication factor and 100 pcm for the Doppler constant, without any difference in the input parameters. Use of such fitness function, hence should be strongly discouraged.

4.8 COMPUTATIONAL TIME

Computational time consumption is an important issue for the purpose of this study: if XS collapsing has to support very long transient calculations, the additional time required for the energy structure determination had better to be much lower than the one spared.

4.8.1 CROSS-SECTION COLLAPSING

As first step one wants to evaluate the time reduction due to the XS collapsing. The test case is selected as a 10 s transient simulation with the ESNII+ core, which is calculated with different number of groups in the few-groups libraries; the many-groups ones are still the 72-groups libraries detailed in §4.1.1. In order to reduce time measurement uncertainty and possible special effects of the energy structure, the test is repeated 3 times for each number of groups, each one with a different energy meshing.

All time measurement are performed by means of the Intel® VTune™ Amplifier 2015 profiler on a node with exclusive access of the InstitutsCluster II (Steinbuch Centre for Computing, 2017b), equipped with processors Intel® Xeon® 5 (2.6 GHz), in serial mode.

The average CPU time consumption, split based on the program section, is shown in Figure 4.21.

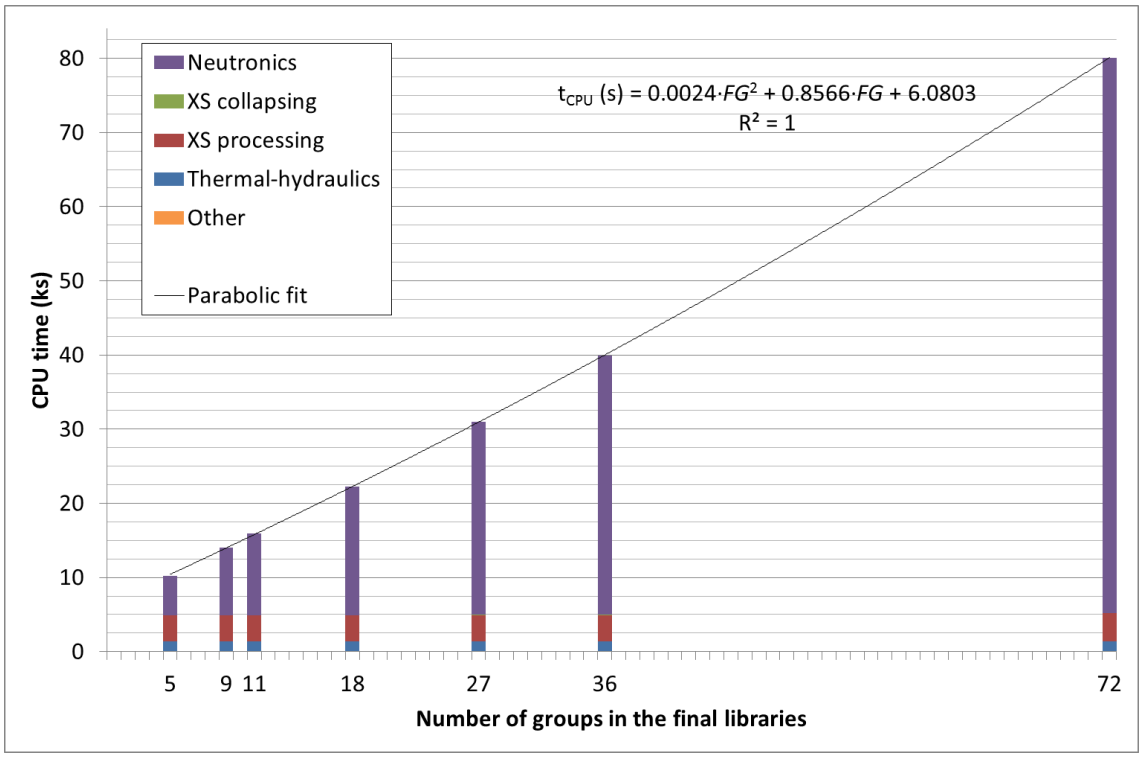

Figure 4.20: Computational time spent in each section of the program during a 10 s transient with different number of groups in the few-groups libraries.

For the uncollapsed XS case, the time spent in the neutronics solver constitutes the 93% of the total computational time, which is about 80 ks. The XS collapsing intervenes on this program section, making the transport solver operate on a problem with smaller dimension; on the contrary, it has no effect on the XS processing (whose time requirements stay constant), which is performed on the whole many-groups libraries, before the collapsing takes place. Thermal-hydraulics section is also completely unaffected. The condensation procedure, of course,

requires resources too, but their amount is in all considered cases between 30 and 40 s, less than 0.5‰ of the time in the uncollapsed case.

It is anyhow worth pointing out that between a simulation performed with fine library condensed to a given number of groups and another one with an input library with that number of groups, the former is expected to provide better results. In fact, it profits from the fact that the weighting spectrum used for the condensation is more precise, as it is estimated "at the moment". The cost for the additional precision is represented by the additional time for the condensation procedure and the larger memory required for storing the information.

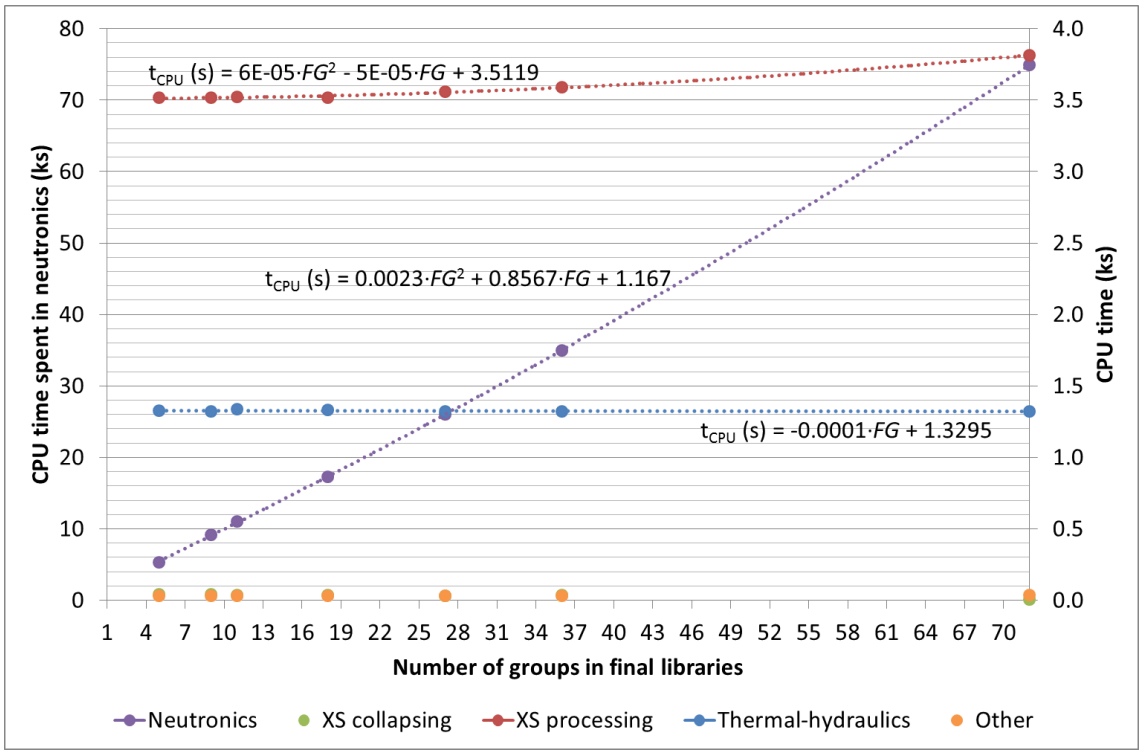

Figure 4.21: Detail of the CPU time components depending on *FG*.

A closer study of the CPU time components, shown in Figure 4.21, makes clear that the time reduction is mainly due to the transport solver, with a correlation which is almost linear. Actually a small quadratic term appears in both neutronics and XS processing section: the reason lies probably in the additional effort required to deal with the scattering matrix, whose dimension is FG^2. With the exception of this contribution, the XS processing time is constant with the number of groups, like the thermal-hydraulics part, which is completely independent from that parameter.

With concern to the 11-groups case, which is used after for comparison with the time required to run METIS, one can reduce the CPU time with XS collapsing by about 64 ks, corresponding to 80% of the 72-groups case.

4.8.2 *ENERGY STRUCTURE DETERMINATION*

Assessment of the time required by METIS to return a reliable result is not an easy task: the GA is a stochastic process, so like the convergence that cannot be assured, the computational time required cannot be fixed, but just estimated on average; in addition, the test of each individual takes a different time depending on the ease of the transport problem convergence associated with the specific energy structure.

Hence, the first step is assessing the time required by each section of METIS, taking into account the number of individuals considered. The GA is run 4 times with the same configuration: 6 generations, each considering a 50-individuals population, with the 72-groups initial libraries and 11-groups final ones. Nevertheless, one has to consider that, even if the total number of considered individuals is 300 for each test, the actual number of fitness function evaluations is lower, as some of them could have been examined previously and so retrieved from the storage tree (§3.6.2); hence, with the hypothesis that the tree search time is negligible with respect to the time required for the solution of the eigenvalue problem preparation and solution, the fitness function evaluation time has to be divided by the number of unique individuals. The hypothesis is justified by the fact that the time required for the whole GA, excluding the one spent in the transport solver, is too low to be measured in all test cases. It is worth pointing out that if one would average the fitness function evaluation time on the total number of individuals, the result would still be valid, but it could be comparable only when the new individuals share is comparable: i.e. its comparability would be restricted to the cases with the same mutation and elitism rates, same generations number, same population size.

Table 4.7 shows the CPU time measurements for each test and the average values, divided into the different sections:

1. SIMMER time: Start-up, input files reading and SIMMER initialisation;
2. Evaluation of the objective k using the uncollapsed many-groups libraries;
3. Fitness function evaluations of all population individuals;
4. Calculation of k and $k^{\dagger}$ (adjoint problem eigenvalue) with the best found energy structure (so using 11 groups);
5. SIMMER time: Execution termination, output file writing.

While the time spent by section 2 depends on the number of groups in the input libraries, points 3 and 4 depend only on the considered energy structure and its number of groups. It is expected that the time employed for point 4 is higher than the double of section 3, as for the final k and $k^{\dagger}$ calculation the flux acceleration (§3.6.1) is not used.

Table 4.7: METIS computational time in s (Massone et al., 2017c).

	Test 1	Test 2	Test 3	Test 4	Average
Unique individuals	262	249	250	259	255±6.5
Computational time (s)					
Objective *k*	58.0	57.8	58.0	56.4	57.5 ± 0.8
Fitness function evaluations	1899.2	1868.4	1837.3	1880.0	7.3 ± 0.1 (per unique individual)
Final *k* and *k*†	24.6	19.1	21.7	14.2	19.9 ± 4.4
SIMMER time	0.7	0.6	0.6	0.6	0.6 ± 0.03

With the data above one can predict the GA duration, once the number of individuals needed for convergence is known. This parameter, however, is also very variable and could be estimated with precision only by studying the implications of the different convergence parameters: population size and growth, selection pressure, mutation and elitism rate…

An approximate estimation is hereafter presented, based on the only population size parameter. Three tests of the GA are performed with the same settings, with the exception of the population size (the tournament size is adjusted too to keep the selection pressure constant), which is 50, 100 or 150 individuals; the objective is measuring the number of unique individuals calculated before convergence during the search of an energy structure for a 72→11 XS collapsing. Convergence is the attaining of a fitness below 1, corresponding to a discrepancy of the *k* in the order of 1 pcm, which is considered an acceptable precision for most transient calculations. Each test is repeated twice to reduce the stochastic effect.

Table 4.8: Number of individuals before METIS convergence (Massone et al., 2017c).

Population size	**50**		**100**		**150**	
Growth rate	1.0					
Mutation rate	5%					
Elitism rate	2%					
Number of tournaments	10		20		30	
Tournament parameter *p*	0.1					
Generations before convergence	16	40	39	35	20	18
Examined individuals	800	2000	3900	3500	3000	2700
Unique individuals	650	1553	3106	2985	2715	2434

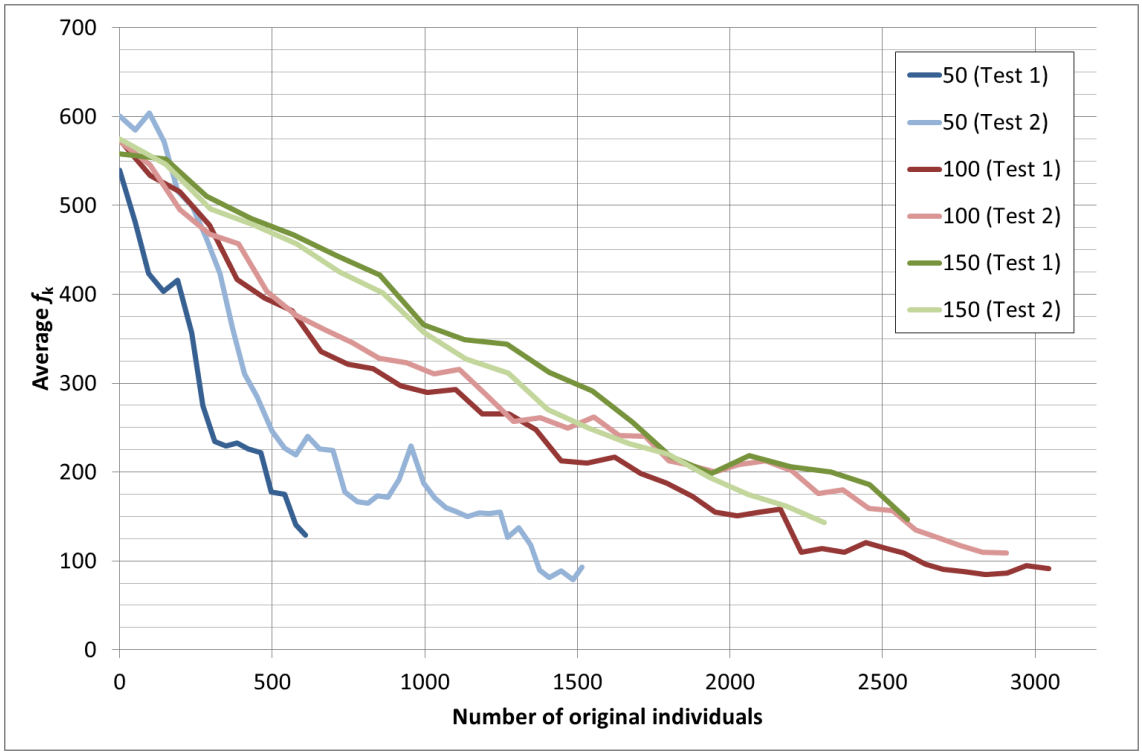

Figure 4.22: Average fitness convergence with different population sizes.

Table 4.8 shows that the tests using a 50-individuals population converge faster than the other cases; however, the trend of the average fitness in Figure 4.22 appears very steep and in some points erratic, suggesting a premature convergence of the GA. This means that the convergence is much influenced by luck and that the population tends to homogenize very quickly; this behavior represents a problem for the GA, as the capability to find new solutions is based on the variety of the population. The other cases, with populations composed by 100 or 150 individuals, take longer to converge, but the fitness trend looks more "healthy". The number of tests, however, is probably insufficient to derive valid conclusions about the best population size to be used.

The fact itself that the average fitness decreases (i.e. it get better) is a bad signal in case lower fitness is required, as the search capability of the GA could be compromised with a homogeneous population. Adaptive GAs (Mc Ginley et al., 2008; Shi et al., 1999) usually intervene on this point, tuning the GA parameters aiming to avoid premature convergence and to keep high the exploration capability of the population. At the same time, however, this should not interfere with the evolution of the population, avoiding the risk of random search.

By averaging the results in Table 4.8 one can estimate the average number of unique individuals to be examined before convergence as 2241±956. Due to the low number of tests, the variance is

very high; however, considering that optimization is still possible, the mean value increased by 2σ can be considered a still conservative estimate of the number of individuals required.

Combining conclusions of §4.8.1, i.e. that XS collapsing to 11 groups allows a CPU time reduction of 64 ks over a 10 s transient, with the results in Table 4.7, one estimates that the spared time is sufficient to evaluate more than 8500 unique solutions. Such number is more than double than 4153, the conservative amount of unique individuals required for convergence assessed above.

Hence, XS collapsing is computationally convenient even when associated to METIS. The spared time clearly depends on the length of the transients, which is usually much longer than 10 s, making the XS condensation + energy structure search operation even more convenient. Moreover, one should consider that the GA could be run only once for each reactor system, provided that the initial conditions do not change too much.

CHAPTER 5. THE PHÉNIX 3D TRANSIENT CASE

As discussed in the introduction, the need for a reliable multigroup transport calculation with few groups is particularly important for three-dimensional transient calculation. The METIS procedure, presented in the previous chapters, effectively addresses the problem of finding the energy structure that reproduces with fidelity the results obtained with the original data.

This chapter shows the application of the METIS approach to an actual 3D transient case referring to the Phénix reactor. After the case description, a suitable energy structure is assessed using the described GA; this is then used to calculate the transient reactivity trend.

5.1 CASE DESCRIPTION

In the introduction of this thesis, it has been suggested that condensed libraries can be very helpful for multigroup transient calculations for 3D cases. In this situation, in fact, one is forced to use a limited amount of energy groups in order to obtain results within acceptable computational time. The XS collapsing tool and the METIS, whose reliability has been proven in the previous chapter, are then applied to a 3D case to show the full potential of the tools.

The chosen case is the reference state of the Control Rod (CR) withdrawal experiments on the Phénix reactor (International Atomic Energy Agency, 2014; Vasile et al., 2011b), based on the KIT model developed by Kriventsev et al. (2014) for the studies with SIMMER-IV (Yamano et al., 2008). Phénix was a prototype SFR, built in France and shut down in 2009. The CR withdrawal tests have been performed among the End of Life Experiments, with a power of reference configuration of 335.4 MW_{th}.

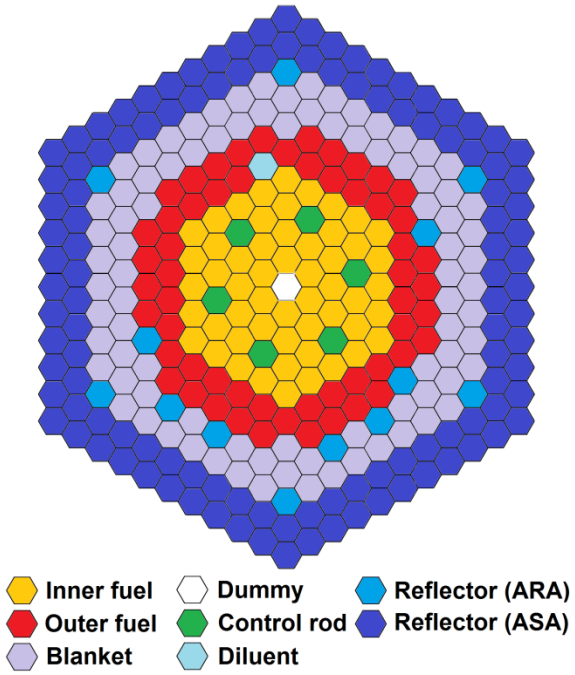

Figure 5.1: Phénix core layout (after International Atomic Energy Agency, 2014).

The model taken into consideration is an adaptation of the HEX-Z meshing into an XYZ structure (since the current version of SIMMER-IV is not capable of treating HEX-Z geometry), with composition described by the linear combination of two isotopic vectors (as usual in SIMMER) to match the composition in the different fuel zones (Kriventsev et al., 2014). The reference composition is characterized by having the six CRs (shown in Figure 5.1) inserted at the same position in the core. In order to obtain reliable estimates of the CRs worth, an effective ^{10}B concentration has been used in the CRs rather than the real one (Gabrielli et al., 2014), so taking into account the CR heterogeneity effect introduced in §2.1.

The transient calculation follows the evolution from the initial conditions to the steady state of the model for the first 30 s.

5.1.1 GENETIC ALGORITHM CONFIGURATION

The input libraries are the 72-group ones described in §4.1.1 and used for the code verification. In this case, however, in order to limit the computational time required for the transient, the final libraries will have only 8 groups.

Similarly, as the current calculation is just an application of the approach presented before, the input parameters of METIS can be relaxed: the aim, in fact, is not to carry out the results analysis anymore, which requires repeated calculations and high precision, but to obtain a reasonably good energy structure for a normal application. The adopted GA configuration is:

- Fitness function: f_{comb};
- Population: 50 individuals, constant size;
- Tournament selection: 10 tournaments, p=0.1;
- Mutation: 5% randomly chosen chromosomes undergo mutation;
- Elitism: 2% of the population;
- Termination condition (generations): 30 completed generations, or 15 consecutive ones without improvement of the best solution; achievement of a fitness lower than 0.01.

Considering the fitness function expression, a convergence limit of 0.1 should yield an energy structure with a Δk lower than 1 pcm and an average flux discrepancy angle $\bar{\xi}$ lower than $\pi/100$; in order to avoid unwanted balancing effects (very large Δk compensated by very small ξ, and vice versa), the limit has been further reduced by a factor of 10.

The observations made in §4.1 about the parameters configuration optimization are entirely valid also in this case. As a consequence, the selection and breeding parameters used for the verification, which proved to work well, have been entirely replicated in this case; it is worth observing that the tournament selection pressure does not depend on the number of tournaments, rather on the ratio between it and the population size.

5.2 ADOPTED ENERGY STRUCTURE

With the configuration specified above, METIS is run. The calculation terminates after the maximum number of generations is explored, without achieving the desired precision. During the 30 completed generations, 1285 unique configurations are explored, a number corresponding, based on (3.13), to 0.006% of all possible solutions, but sufficient to obtain a useful energy structure.

In fact, despite the required precision set for termination could not be obtained, the best solution found, which has a fitness of 0.058, matches the initial expectations, yielding:

- $\Delta k \cong 0.39$ pcm;
- $\bar{\xi} \cong \pi/115$.

Figure 5.2 and Figure 5.3 show the best solutions found during the METIS operation, of which the one with the best fitness is used to run the transient calculation with 8 groups. The boundaries of such energy meshing are given in Table 5.1

Table 5.1: METIS-generated energy structure for the Phénix transient calculation.

Group from input libraries	*1*	*6*	*8*	*9*
Upper energy boundary (eV)	2.000E+07	2.019E+06	1.353E+06	1.108E+06
Group from input libraries	*19*	*25*	*64*	*67*
Upper energy boundary (eV)	3.020E+05	1.228E+05	9.166E+01	9.906E+00

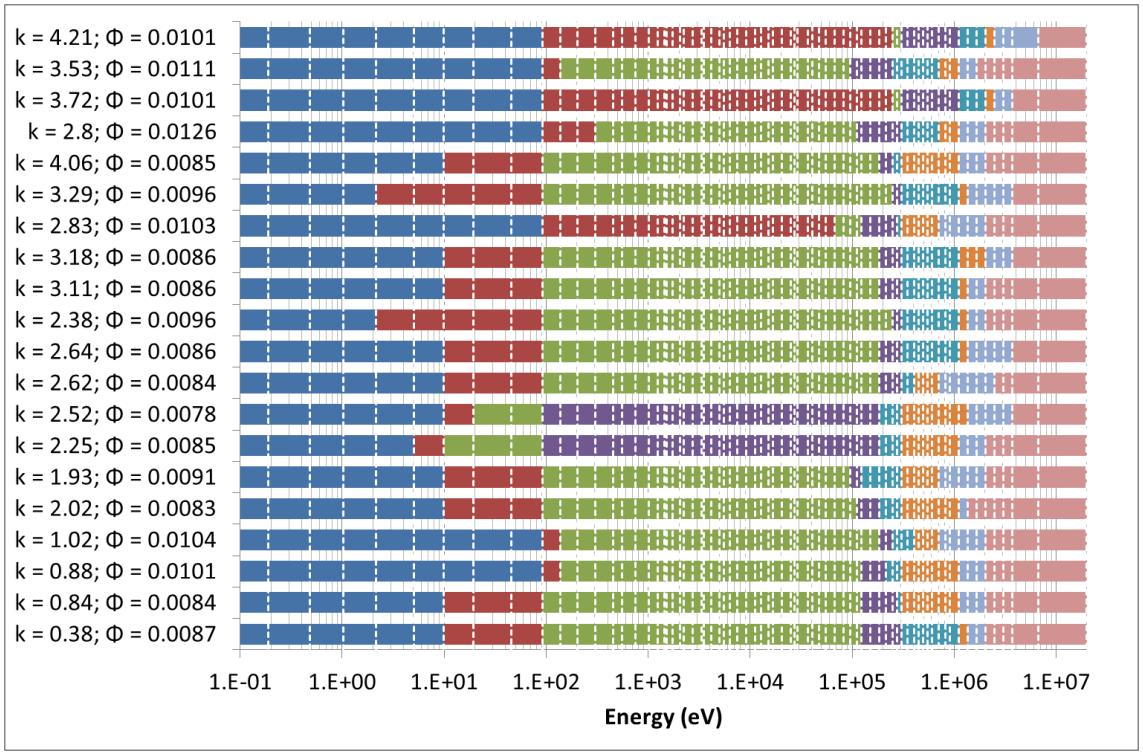

Figure 5.2: Best found energy structures for the Phénix core with the associated f_k and f_Φ, sorted based on f_{comb}. Dotted lines indicate the energy boundaries of the initial libraries; new energy groups are denoted with the same colors.

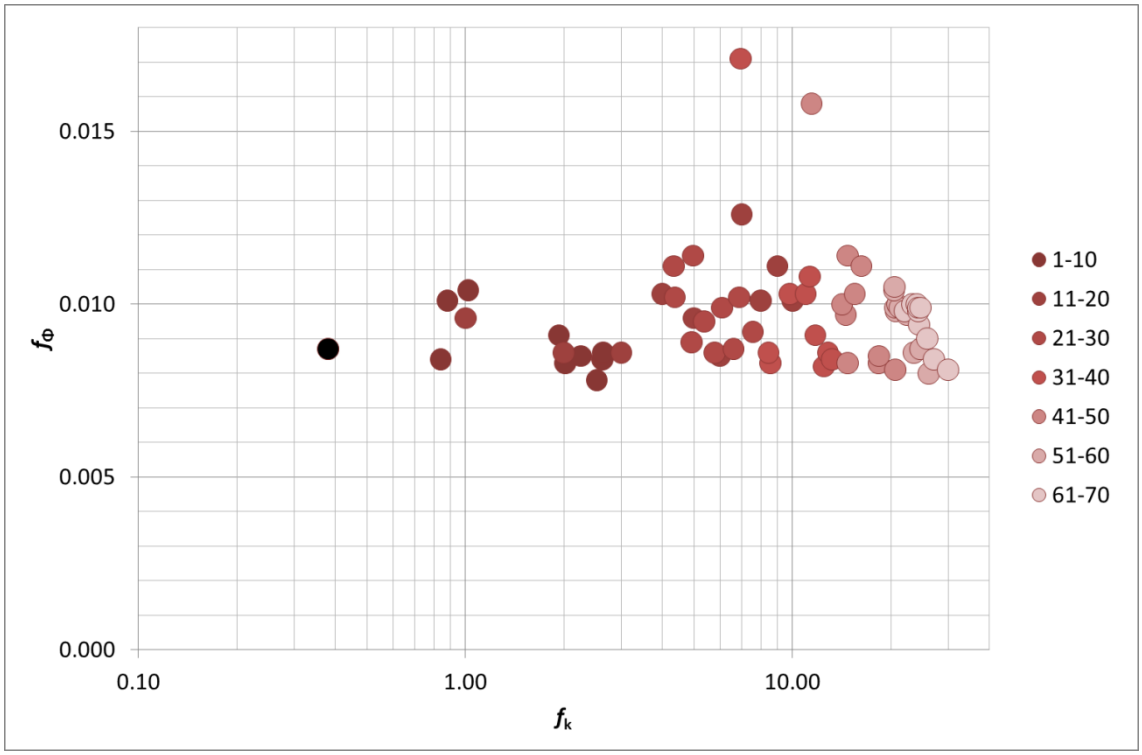

Figure 5.3: Best-70 found energy structures for the Phénix core coloured based on the ranking. The black dot denotes the chosen meshing.

It is interesting observing that the structures shown in Figure 5.2 resemble very much those of the ESNII+ ASTRID and ESFR cases, having a detailed discretization in the fast region, a large condensed group for most of the resonance zone, and some groups devoted to the low-energy region. This behaviour is somehow expected, as the Phénix is a SFR, as the two other ones; however, one can notice that, even if the number of groups is reduced from 11 to 8, the need for detail in the low-energy region is still important.

The convergence history (Figure 5.4) shows a very fast evolution in the first generations, leading to a stagnation in the solution improvement in the later phases, probably due to the limited variability in the genetic pool. The fact that 17% of the 1550 explored individuals is constituted by repeated chromosomes, considering that the elitism rate is set at 2%, is another signal that exploration/exploitation mechanisms can be improved.

Adaptive schemes, e.g. the one proposed by Mc Ginley et al. (2008), or speciation and niching mechanisms (Goldberg, 1989, pp. 185–197) could prove very useful in this case, helping avoiding the homogenization of the genetic pool and supporting the exploitation of the neighborhood of the best found solution, which in this case has been found during the 16th generation, but destroyed immediately after due to fortuitous mutations.

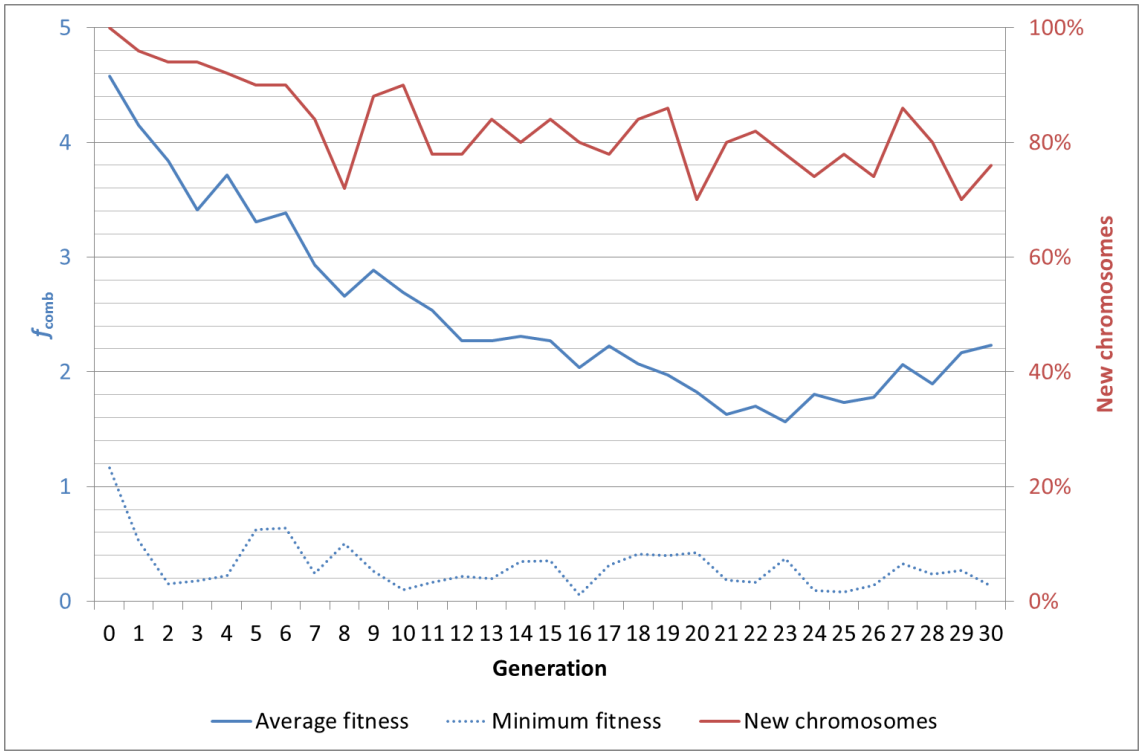

Figure 5.4: Evolution history in METIS for the Phénix case.

5.2.1 *COMPARISON WITH A UNIFORM ENERGY STRUCTURE*

As an additional test, the transient calculation has been repeated with an energy structure not calculated by METIS. The chosen benchmark is a 8-groups energy structure built such that the lethargy intervals covered by the groups are as uniform as possible.

Table 5.2 lists the boundaries of this energy meshing.

Table 5.2: Uniform energy structure for the Phénix transient calculation.

Group from input libraries	*1*	*8*	*27*	*43*
Upper energy boundary (eV)	2.000E+07	1.353E+06	9.482E+04	7.466E+03
Group from input libraries	*59*	*65*	*69*	*72*
Upper energy boundary (eV)	5.545E+02	4.552E+01	2.130E+00	1.890E−01

5.3 TRANSIENT

The transient calculation is then run with the XS collapsing tool, based on the energy structures described in the previous section. The calculations are performed on the ForHLR I

computational system (Steinbuch Centre for Computing, 2017a), using 32 parallel processors, 16 devoted to the neutronic solver and 16 to the SIMMER code.

The employed SIMMER code includes an extension, developed at KIT in the past by Marchetti et al. (2014), which substitutes the DANTSYS (Alcouffe et al., 1995) 3D neutronic solver with PARTISN (Alcouffe and Baker, 2009), which can benefit of the modern parallelization capabilities. Such modification has been already tested (Vezzoni et al., 2016b; Vezzoni et al., 2016a), and it is currently used at KIT for different cases.

The activation of the XS condensation is immediately clear from the time required for the multiplication factor assessment (Table 5.3): while the reference calculation, performed with the many-groups libraries, needs more than 70 s to solve both the direct and the adjoint problems, when 8-groups XS libraries are used 9 s are enough. Such result is in line with the linear trends observed in §4.8.1.

Table 5.3: Multiplication factors for the Phénix case.

	Eigenvalue		**CPU time (s)**	
	k	***k*†**	***k***	***k*†**
Reference (72 groups)	0.99501	0.99498	33.2	39.5
METIS (8 groups)	0.99504	0.99488	3.1	5.8
Uniform (8 groups)	0.99020	0.99017	3.3	5.1

Table 5.3 clearly shows that the uniform energy meshing does not predict the correct multiplication factor, underestimating it by 483 pcm. On the contrary, the energy structure proposed by METIS yields a value of k which is just 3 pcm off the reference value, a discrepancy acceptable for most applications. The discrepancy obtained is higher than the 0.39 pcm obtained during the METIS operation (§5.2), but it is compatible with convergence precision set for the eigenvalue calculations.

The difference between the calculated k and $k^{\dagger}$, which should be equal based on the transport theory, is normal and can be explained with the convergence criteria. It is interesting observing that the solution of the adjoint problem is, in all cases, more computationally expensive than the direct one: this is a known behaviour, probably related with the different groups coupling of the adjoint problem (Dulla, 2017).

Figure 5.5 shows a comparison among the reactivity trends in the SIMMER simulations with the two different energy structures and the reference calculation. The latter one is extremely

expensive from the computational point of view making feasible only the simulation of the first 5 seconds of the transient. Both simulations with condensed XS libraries match very well with the reference calculation, with differences lower than 3 pcm for the METIS case and 2 pcm for the uniform one.

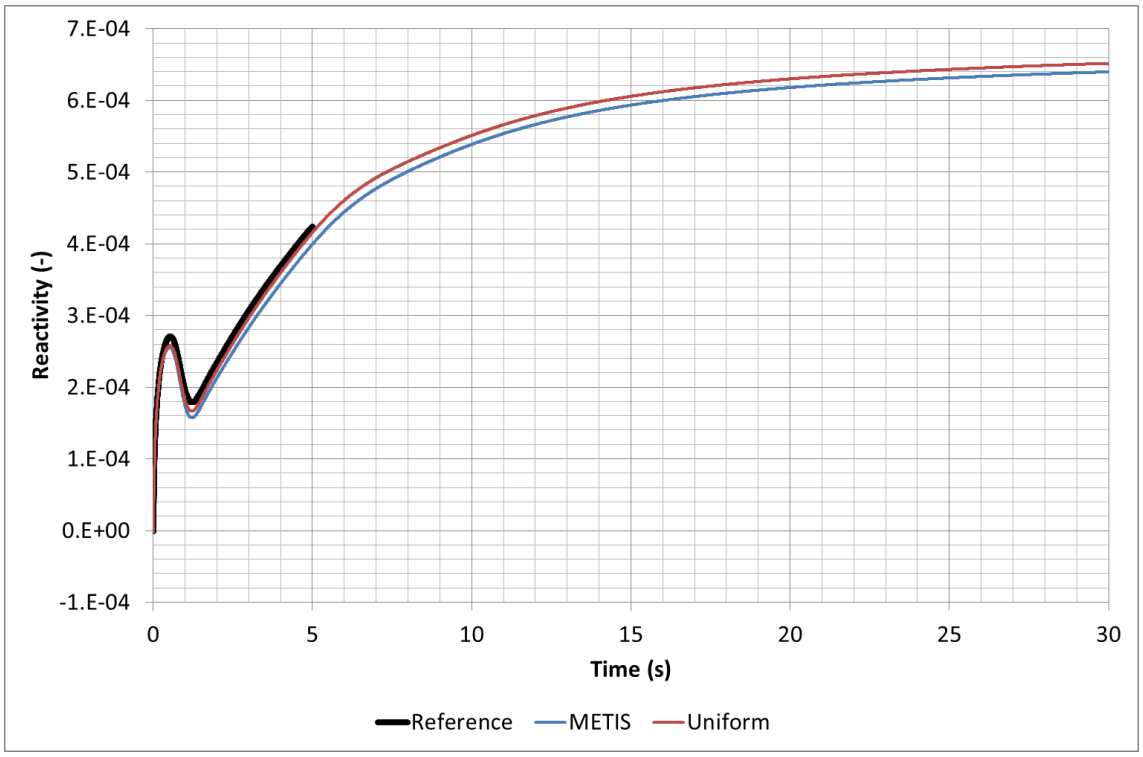

Figure 5.5: Reactivity trend along the Phénix case with different XS libraries.

As the computational effort is already very intense, the use of a profiling tool for the measurement of the time allocation has been avoided. However, an approximate estimate of the employed resources is provided by the computational system ForHLR I, which informs the user of the wall time employed for the program executions. Considering that the processors used for the calculations are not shared with other processes, the wall time should be very close to the actual computation time; nevertheless, one cannot exclude overhead due to, for example, read/write operations.

Table 5.4: Computational time required for the Phénix cases.

	Execution time (wall time)	**Simulated time**	**Speed (per simulated second)**
Reference (72 groups)	5 d 12 h 18 min	7.1 s	18 h 38 min
METIS (8 groups)	3 d 20 h 57 min	30.0 s	3 h 6 min
Uniform (8 groups)	5 d 1 h 37 min	30.0 s	4 h 3 min

Despite the measurement uncertainty, the time consumption results in Table 5.4, show that the XS condensation is very effective in computational time reduction: in fact it can be reduced by a factor between 4.5 and 6. It is important observing that this factor takes into account the time spent in the thermal-hydraulics computation, which is not affected by the XS condensation; hence, the time reduction obtained in the neutronic solver only is larger.

Considering that many transients require more than 3 minutes of simulated time, the computational time with the reference libraries would require months. Instead, the results shown above show that, using the tools introduced in this thesis, such calculations can be completed within few weeks. This can provide a strong contribution to the progressive replacement of 2D calculations with 3D ones.

5.4 REACTION RATES

The results shown in the previous section prove the advantages of including the XS condensation in the transient calculations, but, with the exception of the multiplication factor, do not offer any basis for supporting the adoption of one energy structure over the other.

Also comparing the neutron flux spectrum obtained with the 72-groups libraries and the ones calculated with the condensation tool (Figure 5.6), one sees that the uniform meshing can replicate the profile quite accurately, although the energy structure suggested by METIS offers a better representation of the fast region, more important for this reactor type.

However, the comparison of the reaction rates estimated in the three cases (reference, uniform meshing and METIS energy structure) shows the validity and the strength of the method proposed for the generation of the cross-sections.

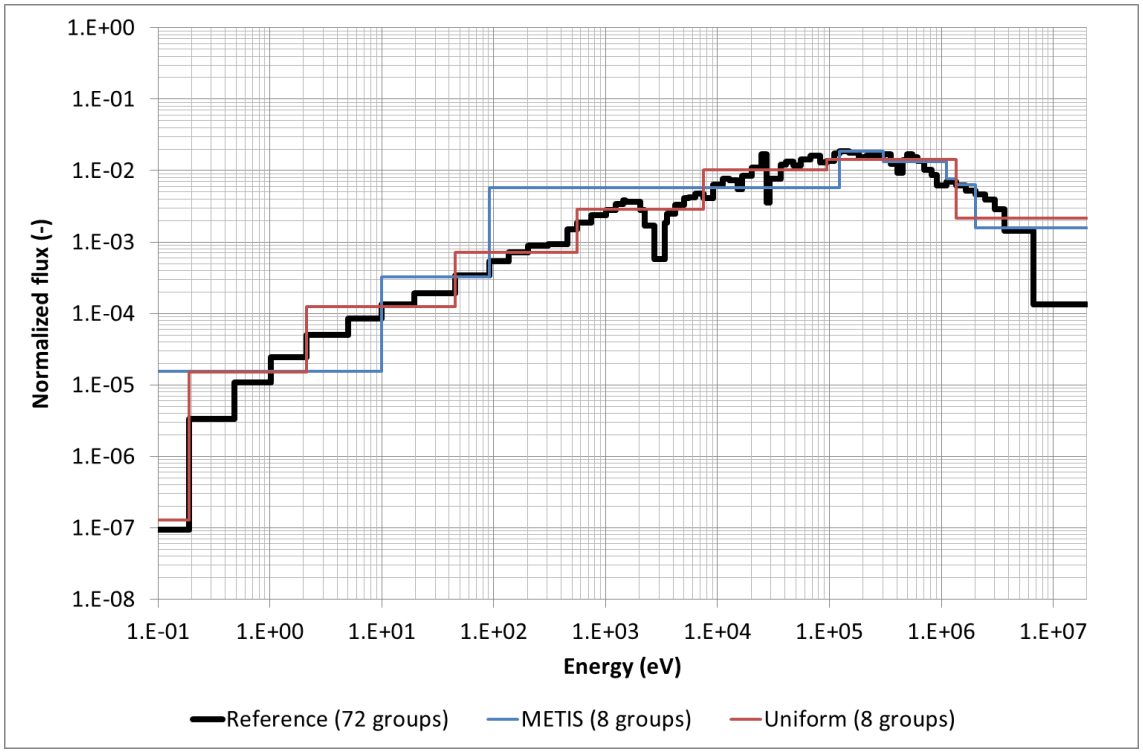

Figure 5.6: Normalized neutron flux for the Phénix case with different energy structures.

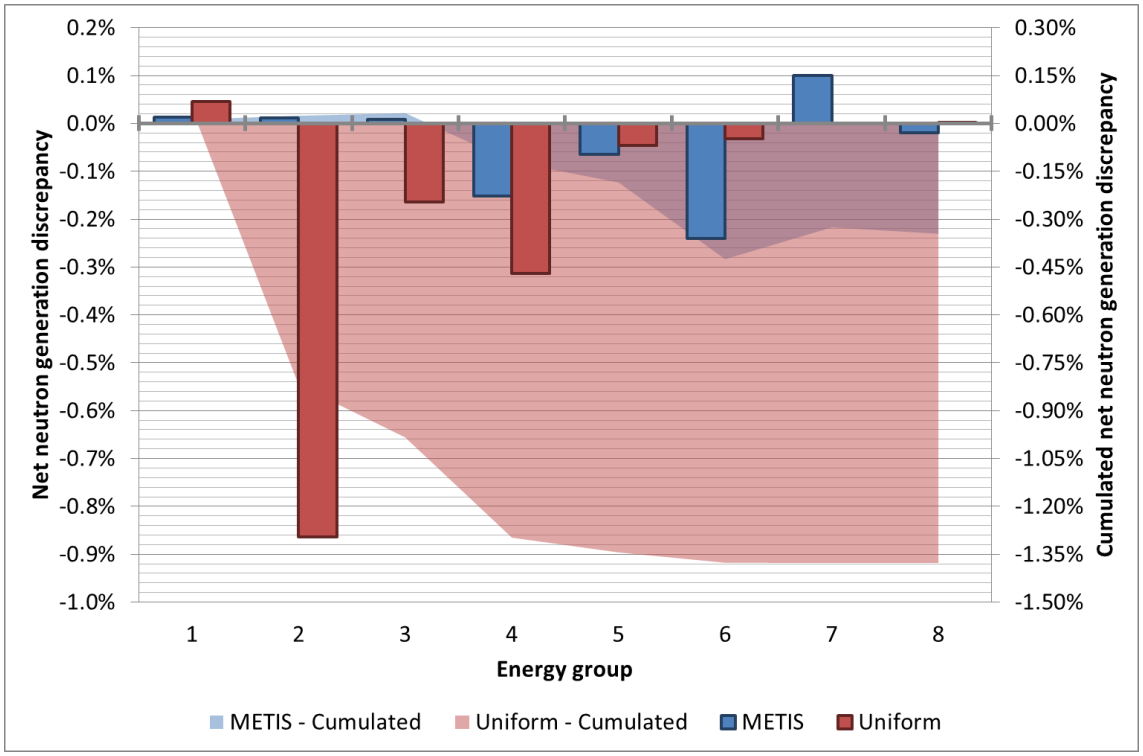

Figure 5.7: Discrepancy of the net neutron generation in each group with respect to the reference case for the Phénix core with different energy structures. The values are normalized over the integral fission reaction rate.

Figure 5.7 shows the discrepancy with respect to the reference of the net neutron generation per group; it is given by the difference between fission and absorption reaction rates (as the multigroup fission XS includes the average neutrons per fission in it). It can be observed that the uniform energy discretization presents higher discrepancies than the meshing suggested by METIS; the error in group 2 is more than 0.8% of the average number of neutrons generated in the core. The cumulated curve (also in Figure 5.7) shows that these errors do not compensate among the groups, but add up to an absorption rate in excess by 1.4% of the fission generation. Such unbalance can easily justify the 483 pcm discrepancy in the multiplication factor.

On the contrary, the energy structure originated by the GA produces discrepancies which are always lower than 0.4% and result in an overall absorption excess of only 0.3%.

CHAPTER 6. CONCLUSIONS AND PERSPECTIVES

A critical issue when dealing with reactor physics calculations based on multigroup transport theory is the determination of the correct discretization of the energy space. The discretization procedures described in literature are vague and leave many issues open to arbitrary or intuitive decisions; moreover, many studies and comparison with benchmarks are required to obtain a good energy structure, making this step particularly complex and expensive. This encourages the use of "general-purpose" cross-section libraries, even if the discretization is *per se* system-specific; such behaviour can reduce the results accuracy or even undermine the reliability of the results.

At the same time, available computational power is, at present, still insufficient for transient Monte Carlo calculations, especially for 3D cases, making multigroup approximation the main route to deal with the energy dependency of the neutron flux.

In this work, I presented a new procedure based on evolutionary computation which is able to determine automatically the optimal energy structure for the studied core. The algorithm, called METIS, has then been coupled with the accidental transient analysis code SIMMER.

A first approach has been attempted with greedy algorithms, but the problem does not have the properties required for such an algorithm to converge to the optimal solution and might even return the worst possible option. I have then studied the opportunity of using metaheuristics, which do not ensure convergence to the global optimal solution but can easily provide reasonably good options. In particular, I have chosen the genetic algorithm paradigm.

The devised algorithm starts with the generation of a group of random chromosomes, the initial population; each chromosome codes for a specific possible solution of the problem. Each member of the population is graded based on its suitability in solving the problem with a fitness function. Once the whole population has been evaluated, a new population is generated from the components of the old ones: the chromosomes swap parts of their information with each other and undergo mutations, so exploring other possible solutions. The key to the evolution however is the fitness, as better graded options have higher chances of being used to breed the next generation, passing over their good features, while bad options are likely to be lost, together

with their genetic pool. Generation after generation, the population fitness improves and the solution space is explored, until the termination criteria are met.

The fitness function plays a central role in this procedure, as it constitutes the basis for comparison of the different options. It is specific of the problem to be solved and usually many options are available; however, one should take into account that it must be evaluated many times during the algorithm run, and CPU time consumption should be considered. Three different options have been included in this work: the discrepancy between the multiplication factors of the considered solution and the reference case; the difference in the flux distribution among the groups; a combination of the two previous options. The tests I performed on the 2D model of the ESNII+ ASTRID show that, while the groups distribution function cannot discriminate between solutions but tend to return degenerate cases, the other two options are very effective. The combined fitness function, in particular can provide even better results than the one based on the multiplication factor only.

The effectiveness of the GA approach has been verified with a 72-groups library on three different test systems: the ESNII+ ASTRID, the ESFR and the MSFR. The tests show that the best solutions found can actually reproduce the multiplication factor, the reaction rates, the void feedback coefficients and the Doppler coefficients of the cases with the uncollapsed XS libraries. I applied the algorithm also to a 3D transient analysis of the Phénix reactor yielding, also in this case, clear advantages in terms of results quality and a reduction of the computational time higher than 75%.

Despite tests have been performed only on fast reactor systems, the approach is general and can be applied unchanged to any other core. Actually, the use of the algorithm on light water reactor systems is considered an interesting activity for future studies.

The observation of the patterns characterizing the best solutions at 11 groups offers interesting hints for the study of the important neutron phenomena in the reactors. In both SFR cases the best energy structures have a high concentration of groups in the fast region, a single group covering most of the resonance region between 30 keV and 500 eV and a few groups allocated in the lower energy region below 500 eV. These features can be explained looking at the neutron flux spectrum and to the relevant cross-sections; some of them, like the need to carefully discretize the low energy range, can be unexpected and prove even more how an automatic system can help preventing that important effects are overlooked.

The cases of the MSFR and of three modified versions of the ESNII+ show the effects of the core heterogeneity: as the neutron spectrum is different depending on the cell type, the resulting

energy structure must be a compromise taking into account the needs of all cells, with an appropriate weighting depending on importance and flux of the cell itself. Such parameters are automatically taken into account by METIS, as they are implicitly included in the fitness function, and the additional complications make the fitness difference between adequate and inadequate energy structures larger. In homogenous systems, on the contrary, the constraints are too soft, and the number of solutions acceptable for the system becomes very large.

I have performed other tests to observe the applicability of the energy structures to systems which are not the ones used for their generation. As expected, the discretization is proper of the system and, when used for other ones, could end up in large discrepancies in the results. However, the differences can be small if the two systems are similar, as for ESNII+ ASTRID and ESFR, which are both SFRs. This means that during a transient one can keep using the energy structure calculated at the beginning, provided that the conditions do not change too much. An interesting topic for future research is considered the effect of the energy structure on the reliability of the transients and the possible advantages of updating it periodically. In fact, attention should be paid when changing the energy structure during a calculation, as the uncertainties introduced when redistributing the neutrons among the energy groups at the moment of the structure change could be more relevant than the benefits of a correct structure.

Different actions have been taken to optimize the algorithm, with particular attention to the fitness function evaluation, which takes most of the algorithm computational time: a dynamic storage system avoids that the fitness of already examined individuals is calculated twice; the fitness calculation, which includes the solution of the eigenvalue problem, is also accelerated using the objective neutron flux, known in advance, as an educated guess. Thank to these measures the cross-section collapsing is a convenient operation even including the optimization of the energy structure, as the time required for the latter can be largely covered by the former operation in normal transient cases.

Even better results could be obtained by introducing adaptive parameter control into the genetic algorithm: this would mean having crossing-over and mutation probability adjusted at each generation to maintain a high genetic variability and so better explore the search space, resulting in better solutions and lower computational time. Such an improvement could prove particularly useful in the previously presented case of a changing energy structure: in fact, that would require interrupting the transient and running the genetic algorithm to update the discretization. And clearly, when the algorithm has to be run more than once for each calculation, the computational time becomes a much more relevant issue. Hence, this activity is considered particularly important for the future.

The algorithm addresses a need that in the past, except for a few authors, has been considered mostly from the empirical point of view, and I consider of interest further upgrading it in future works. In addition to the already cited adaptivity and variable energy structures, further studies should consider different fitness functions, e.g. based on reaction rates, and more advanced genetic operators (like niching and speciation), to improve the search efficiency. In addition, it would be interesting studying the structure of the optimal discretization of other different systems, including thermal spectrum ones.

The topic of the energy structure optimization could also profit from the advances in the field of machine learning. An artificial neural network could be designed to take as input the composition and the geometry of a system and return its specific energy structure without testing thousands of cases. In fact, once trained with many different cases, the neural network would learn to associate to each input parameter mix the corresponding needed discretization, not only for the cases that it has already encountered, but also, by similarity, for completely new cases. In this work, the genetic algorithm could be used for the training of the network.

APPENDIX A DERIVATION OF THE TRANSPORT EQUATION P_1 APPROXIMATION

The basis of this thesis work on XS condensation lies in the P_1 approximation of the multigroup transport theory. Although these topics are present in literature (Coppa et al., 2010) and are often explained in reactor physics textbooks (Bell and Glasstone, 1970; Cacuci, 2010; Duderstadt and Hamilton, 1976; Stacey, 2001; Weinberg and Wigner, 1958), a clear and organic derivation of the approximation, considering from the beginning all neutron flux parameters (space, energy, direction and time), could not be found. Such complete formulation highlights the interconnection arising between the parameters during the XS collapsing (as in the case of directional cross-sections).

Starting from the neutron transport equation, the spherical harmonics formulation of the equation is derived in this appendix. The P_1 approximation is then obtained, as a special case of the general formulation.

A.1 SPHERICAL HARMONICS FORMULATION

By the spherical harmonics method the transport equation is expanded into functions, so obtaining a system of an infinite number of equations. The expansion can be then truncated.

The starting point is the energy-dependent neutron transport equation:

$$\begin{aligned}\frac{1}{v(E)}\frac{\partial\varphi(\boldsymbol{r},E,\widehat{\boldsymbol{\Omega}},t)}{\partial t}+\widehat{\boldsymbol{\Omega}}\cdot\boldsymbol{\nabla}\varphi(\boldsymbol{r},E,\widehat{\boldsymbol{\Omega}},t)+\Sigma_{\mathrm{t}}(\boldsymbol{r},E)\varphi(\boldsymbol{r},E,\widehat{\boldsymbol{\Omega}},t)=\\ =\oint\int_0^{+\infty}\Sigma_{\mathrm{s}}(\boldsymbol{r},E')\varphi(\boldsymbol{r},E',\widehat{\boldsymbol{\Omega}}',t)f_{\mathrm{s}}(\boldsymbol{r},E'\to E,\widehat{\boldsymbol{\Omega}}'\cdot\widehat{\boldsymbol{\Omega}})\,\mathrm{d}E'\,\mathrm{d}\widehat{\boldsymbol{\Omega}}'+\\ +\frac{\chi(\boldsymbol{r},E)}{4\pi}\oint\int_0^{+\infty}\nu(\boldsymbol{r},E')\Sigma_{\mathrm{f}}(\boldsymbol{r},E')\varphi(\boldsymbol{r},E',\widehat{\boldsymbol{\Omega}}',t)\,\mathrm{d}E'\,\mathrm{d}\widehat{\boldsymbol{\Omega}}'+\\ +S(\boldsymbol{r},E,\widehat{\boldsymbol{\Omega}},t)\end{aligned}\qquad\textbf{(A.1)}$$

One can notice that the XSs do not depend on direction: this constitutes the isotropic medium hypothesis. In other words, the atomic nuclei can be modelled as mono-dimensional spheres,

making all collision directions equal in the coordinate system of the nucleus. On the contrary, the scattering angle

$$\mu_0 = \widehat{\boldsymbol{\Omega}}' \cdot \widehat{\boldsymbol{\Omega}}, \tag{A.2}$$

i.e the angle between the trajectories of the incoming and outgoing neutron, is important for the scattering term, which hence depends on it. In fact, in a three-dimensional collision model with spheres, the scattering angle characterizes the distance between the colliding particle trajectory and the target centre, and so the momentum and energy transferred in the collision.

The Legendre polynomials P_n represent an orthogonal and complete set of functions on the interval $[-1, +1]$, i.e.

$$\int_{-1}^{1} \mathrm{P}_n(x)\mathrm{P}_m(x)\,\mathrm{d}x = \frac{2\delta_{nm}}{2n+1}, \tag{A.3}$$

making them very suitable for expanding continuous functions on the said interval.

The scattering term f_s can be expressed as

$$f_\mathrm{s}(\boldsymbol{r}, E' \to E, \mu_0) = \frac{1}{2\pi}\sum_{n=0}^{\infty}\frac{2n+1}{2} f_n(\boldsymbol{r}, E' \to E)\mathrm{P}_n(\mu_0)\,; \tag{A.4}$$

integration of (A.4) multiplied on both sides by $\mathrm{P}_m(\mu_0)$, using the orthogonality property (A.3), yields the formula to calculate the moments f_n of f_s

$$f_n(\boldsymbol{r}, E' \to E) = 2\pi \int_{-1}^{1} f_\mathrm{s}(\boldsymbol{r}, E' \to E, \mu_0) \cdot \mathrm{P}_n(\mu_0)\,\mathrm{d}\mu_0. \tag{A.5}$$

It is important specifying that, as in a scattering interaction all incoming neutrons are also outgoing neutrons, f_s must respect

$$\begin{aligned} \oint f_\mathrm{s}(\boldsymbol{r}, E' \to E, \mu_0)\,\mathrm{d}\widehat{\boldsymbol{\Omega}} &= \oint f_\mathrm{s}(\boldsymbol{r}, E' \to E, \mu_0)\mathrm{P}_0(\mu_0)\,\mathrm{d}\widehat{\boldsymbol{\Omega}} = \\ &= \int_{-1}^{1} f_\mathrm{s}(\boldsymbol{r}, E' \to E, \mu_0) \cdot \mathrm{P}_0(\mu_0)\,\mathrm{d}\mu_0 \int_0^{2\pi} d\eta = f_0(\boldsymbol{r}, E' \to E) \\ &\equiv f_\mathrm{s}(\boldsymbol{r}, E' \to E), \end{aligned} \tag{A.6}$$

with

$$\int_0^{+\infty} f_0(\boldsymbol{r}, E' \to E)\,\mathrm{d}E = 1; \tag{A.7}$$

(A.6) implies that

$$\bar{f}_\mathrm{s}(\boldsymbol{r}, E' \to E, \mu_0) = \frac{\oint f_\mathrm{s}(\boldsymbol{r}, E' \to E, \mu_0)\,\mathrm{d}\widehat{\boldsymbol{\Omega}}}{\oint \mathrm{d}\widehat{\boldsymbol{\Omega}}} = \frac{1}{2\pi} f_\mathrm{s}(\boldsymbol{r}, E' \to E), \tag{A.8}$$

hence the 2π term in (A.4).

It is possible to separate the 2 variables $\widehat{\boldsymbol{\Omega}}$ and $\widehat{\boldsymbol{\Omega}}'$ in the Legendre polynomial by using the associated Legendre functions P_n^β

$$\mathrm{P}_n(\mu_0) = \mathrm{P}_n\left(\widehat{\boldsymbol{\Omega}}' \cdot \widehat{\boldsymbol{\Omega}}\right) = \sum_{\beta=-n}^{n} \frac{(n-\beta)!}{(n+\beta)!} \mathrm{P}_n^\beta(\mu)\mathrm{P}_n^\beta(\mu')\mathrm{e}^{i\beta(\eta-\eta')}, \tag{A.9}$$

where one considers the angle $\widehat{\boldsymbol{\Omega}}$ expressed in spherical components ϑ and η

$$\widehat{\boldsymbol{\Omega}} \triangleq \sin\vartheta\cos\eta\,\mathbf{u_x} + \sin\vartheta\sin\eta\,\mathbf{u_y} + \cos\vartheta\,\mathbf{u_z} \tag{A.10}$$

and

$$\mu \triangleq \cos\vartheta. \tag{A.11}$$

With (A.9) and by introducing the spherical harmonics

$$\mathrm{Y}_n^\beta\left(\widehat{\boldsymbol{\Omega}}\right) = \sqrt{\frac{(2n+1)(n-\beta)!}{4\pi(n+\beta)!}}\,\mathrm{P}_n^\beta(\mu)\mathrm{e}^{i\beta\eta} \tag{A.12}$$

the scattering term can be reformulated into

$$f_{\mathrm{s}}(\boldsymbol{r}, E' \to E, \mu_0) = \sum_{n=0}^{\infty} \frac{2n+1}{4\pi} f_n(\boldsymbol{r}, E' \to E) \sum_{\beta=-n}^{n} \frac{(n-\beta)!}{(n+\beta)!} \mathrm{P}_n^{\beta}(\mu) \mathrm{P}_n^{\beta}(\mu') \mathrm{e}^{i\beta(\eta-\eta')} =$$
$$= \sum_{n=0}^{\infty} f_n(\boldsymbol{r}, E' \to E) \sum_{\beta=-n}^{n} \mathrm{Y}_n^{\beta}(\widehat{\boldsymbol{\Omega}}) \cdot \overline{\mathrm{Y}_n^{\beta}}(\widehat{\boldsymbol{\Omega}}'), \tag{A.13}$$

being

$$\overline{\mathrm{Y}_n^{\beta}}(\widehat{\boldsymbol{\Omega}}) = \sqrt{\frac{(2n+1)(n-\beta)!}{4\pi(n+\beta)!}} \mathrm{P}_n^{\beta}(\mu) \mathrm{e}^{-i\beta\eta} \tag{A.14}$$

i.e. the complex conjugate of the spherical harmonic Y_n^{β}.

The spherical harmonics are orthonormal, i.e.

$$\oint \mathrm{Y}_n^{\beta}(\widehat{\boldsymbol{\Omega}}) \overline{\mathrm{Y}_m^{\alpha}}(\widehat{\boldsymbol{\Omega}}) \, \mathrm{d}\widehat{\boldsymbol{\Omega}} = \delta_{nm} \delta_{\alpha\beta}. \tag{A.15}$$

With (A.13), the scattering term of (A.1) becomes

$$\oint \int_0^{+\infty} \Sigma_{\mathrm{s}}(\boldsymbol{r}, E') \varphi(\boldsymbol{r}, E', \widehat{\boldsymbol{\Omega}}', t) f_{\mathrm{s}}(\boldsymbol{r}, E' \to E, \widehat{\boldsymbol{\Omega}}' \cdot \widehat{\boldsymbol{\Omega}}) \, \mathrm{d}E' \, \mathrm{d}\widehat{\boldsymbol{\Omega}}' =$$
$$= \oint \int_0^{+\infty} \Sigma_{\mathrm{s}}(\boldsymbol{r}, E') \varphi(\boldsymbol{r}, E', \widehat{\boldsymbol{\Omega}}', t) \sum_{n=0}^{\infty} f_n(\boldsymbol{r}, E' \to E) \sum_{\beta=-n}^{n} \mathrm{Y}_n^{\beta}(\widehat{\boldsymbol{\Omega}}) \cdot \overline{\mathrm{Y}_n^{\beta}}(\widehat{\boldsymbol{\Omega}}') \, \mathrm{d}E' \, \mathrm{d}\widehat{\boldsymbol{\Omega}}'. \tag{A.16}$$

Moving out of the integral the variables not depending on $\widehat{\boldsymbol{\Omega}}'$, with the assumption that the series converge, one obtains the final expression for the scattering term

$$\oint \int_0^{+\infty} \Sigma_{\mathrm{s}}(\boldsymbol{r}, E') \varphi(\boldsymbol{r}, E', \widehat{\boldsymbol{\Omega}}', t) f_{\mathrm{s}}(\boldsymbol{r}, E' \to E, \widehat{\boldsymbol{\Omega}}' \cdot \widehat{\boldsymbol{\Omega}}) \, \mathrm{d}E' \, \mathrm{d}\widehat{\boldsymbol{\Omega}}' =$$
$$= \int_0^{+\infty} \Sigma_{\mathrm{s}}(\boldsymbol{r}, E') \sum_{n=0}^{\infty} f_n(\boldsymbol{r}, E' \to E) \sum_{\beta=-n}^{n} \mathrm{Y}_n^{\beta}(\widehat{\boldsymbol{\Omega}}) \oint \varphi(\boldsymbol{r}, E', \widehat{\boldsymbol{\Omega}}', t) \cdot \overline{\mathrm{Y}_n^{\beta}}(\widehat{\boldsymbol{\Omega}}') \, \mathrm{d}\widehat{\boldsymbol{\Omega}}' \, \mathrm{d}E' =$$
$$= \int_0^{+\infty} \Sigma_{\mathrm{s}}(\boldsymbol{r}, E') \sum_{n=0}^{\infty} f_n(\boldsymbol{r}, E' \to E) \sum_{\beta=-n}^{n} \mathrm{Y}_n^{\beta}(\widehat{\boldsymbol{\Omega}}) \varphi_n^{\beta}(\boldsymbol{r}, E', t) \, \mathrm{d}E', \tag{A.17}$$

with φ_n^β being the moments of the angular distributions

$$\varphi_n^\beta(\boldsymbol{r},E,t)=\oint \varphi\left(\boldsymbol{r},E,\widehat{\boldsymbol{\Omega}},t\right)\cdot\overline{\mathrm{Y}_n^\beta}\left(\widehat{\boldsymbol{\Omega}}\right)\mathrm{d}\widehat{\boldsymbol{\Omega}}. \tag{A.18}$$

The neutron flux (and similarly the source term) can be expanded into a series of spherical harmonics

$$\varphi\left(\boldsymbol{r},E,\widehat{\boldsymbol{\Omega}},t\right)=\sum_{n=0}^{\infty}\sum_{\beta=-n}^{n}\varphi_n^\beta(\boldsymbol{r},E,t)\cdot\mathrm{Y}_n^\beta\left(\widehat{\boldsymbol{\Omega}}\right); \tag{A.19}$$

as the spherical harmonics are orthonormal, based on (A.15),

$$\begin{aligned}\oint \varphi\left(\boldsymbol{r},E,\widehat{\boldsymbol{\Omega}},t\right)\overline{\mathrm{Y}_m^\alpha}\left(\widehat{\boldsymbol{\Omega}}\right)\mathrm{d}\widehat{\boldsymbol{\Omega}}&=\sum_{n=0}^{\infty}\sum_{\beta=-n}^{n}\varphi_n^\beta(\boldsymbol{r},E,t)\oint \mathrm{Y}_n^\beta\left(\widehat{\boldsymbol{\Omega}}\right)\overline{\mathrm{Y}_m^\alpha}\left(\widehat{\boldsymbol{\Omega}}\right)\mathrm{d}\widehat{\boldsymbol{\Omega}}=\\&=\sum_{n=0}^{\infty}\sum_{\beta=-n}^{n}\varphi_n^\beta(\boldsymbol{r},E,t)\delta_{nm}\delta_{\alpha\beta}=\varphi_m^\alpha(\boldsymbol{r},E,t).\end{aligned} \tag{A.20}$$

The same procedure used for the scattering term can be employed with the fission term, here considering the scattering function constant (as the fission is usually assumed to be isotropic),

$$\begin{aligned}\oint\int_0^{+\infty}\nu(\boldsymbol{r},E')\Sigma_{\mathrm{f}}(\boldsymbol{r},E')\varphi\left(\boldsymbol{r},E',\widehat{\boldsymbol{\Omega}}',t\right)\mathrm{d}E'\,\mathrm{d}\widehat{\boldsymbol{\Omega}}'&=\\&=\int_0^{+\infty}\nu(\boldsymbol{r},E')\Sigma_{\mathrm{f}}(\boldsymbol{r},E')\sum_{n=0}^{\infty}h_n\sum_{\beta=-n}^{n}\mathrm{Y}_n^\beta\left(\widehat{\boldsymbol{\Omega}}\right)\varphi_n^\beta(\boldsymbol{r},E',t)\,\mathrm{d}E'\end{aligned} \tag{A.21}$$

with the moments of the fission emission function

$$h_n=2\pi\int_{-1}^{1}1\cdot\mathrm{P}_n(\mu_0)\,\mathrm{d}\mu_0; \tag{A.22}$$

however, as

$$\int_{-1}^{1}\mathrm{P}_n(x)\,\mathrm{d}x=2\delta_{n,0}, \tag{A.23}$$

then (A.21) reduces to

$$\oint \int_0^{+\infty} \nu(\boldsymbol{r},E')\Sigma_{\mathrm{f}}(\boldsymbol{r},E')\varphi\left(\boldsymbol{r},E',\widehat{\boldsymbol{\Omega}}',t\right)\mathrm{d}E'\,\mathrm{d}\widehat{\boldsymbol{\Omega}}' = \\ = 4\pi\int_0^{+\infty} \nu(\boldsymbol{r},E')\Sigma_{\mathrm{f}}(\boldsymbol{r},E')\mathrm{Y}_0^0\left(\widehat{\boldsymbol{\Omega}}\right)\varphi_0^0(\boldsymbol{r},E',t)\,\mathrm{d}E'. \tag{A.24}$$

Finally, the transport equation (A.1) can be written as

$$\frac{1}{v(E)}\frac{\partial}{\partial t}\left[\sum_{n=0}^{\infty}\sum_{\beta=-n}^{n}\varphi_n^\beta(\boldsymbol{r},E,t)\cdot\mathrm{Y}_n^\beta\left(\widehat{\boldsymbol{\Omega}}\right)\right]+\widehat{\boldsymbol{\Omega}}\cdot\boldsymbol{\nabla}\left[\sum_{n=0}^{\infty}\sum_{\beta=-n}^{n}\varphi_n^\beta(\boldsymbol{r},E,t)\cdot\mathrm{Y}_n^\beta\left(\widehat{\boldsymbol{\Omega}}\right)\right]+ \\ +\Sigma_{\mathrm{t}}(\boldsymbol{r},E)\sum_{n=0}^{\infty}\sum_{\beta=-n}^{n}\varphi_n^\beta(\boldsymbol{r},E,t)\cdot\mathrm{Y}_n^\beta\left(\widehat{\boldsymbol{\Omega}}\right)= \\ =\int_0^{+\infty}\Sigma_{\mathrm{s}}(\boldsymbol{r},E')\sum_{n=0}^{\infty}f_n(\boldsymbol{r},E'\to E)\sum_{\beta=-n}^{n}\mathrm{Y}_n^\beta\left(\widehat{\boldsymbol{\Omega}}\right)\varphi_n^\beta(\boldsymbol{r},E',t)\,\mathrm{d}E'+ \\ +\frac{\chi(\boldsymbol{r},E)}{4\pi}\int_0^{+\infty}\nu(\boldsymbol{r},E')\Sigma_{\mathrm{f}}(\boldsymbol{r},E')\mathrm{Y}_0^0\left(\widehat{\boldsymbol{\Omega}}\right)\varphi_0^0(\boldsymbol{r},E',t)\,\mathrm{d}E'+ \\ +\sum_{n=0}^{\infty}\sum_{\beta=-n}^{n}S_n^\beta(\boldsymbol{r},E,t)\cdot\mathrm{Y}_n^\beta\left(\widehat{\boldsymbol{\Omega}}\right). \tag{A.25}$$

By multiplying each term by $\overline{\mathrm{Y}_m^\alpha}\left(\widehat{\boldsymbol{\Omega}}\right)$ and integrating over $\widehat{\boldsymbol{\Omega}}$, using the orthogonality property as formulated in (A.20), the transport equation (A.25) is expressed in the form of a system of equations

$$\frac{1}{v(E)}\frac{\partial\varphi_m^\alpha(\boldsymbol{r},E,t)}{\partial t}+\oint\sum_{n=0}^{\infty}\sum_{\beta=-n}^{n}\widehat{\boldsymbol{\Omega}}\cdot\boldsymbol{\nabla}\varphi_n^\beta(\boldsymbol{r},E,t)\cdot\mathrm{Y}_n^\beta\left(\widehat{\boldsymbol{\Omega}}\right)\overline{\mathrm{Y}_m^\alpha}\left(\widehat{\boldsymbol{\Omega}}\right)\,\mathrm{d}\widehat{\boldsymbol{\Omega}}+ \\ +\Sigma_{\mathrm{t}}(\boldsymbol{r},E)\varphi_m^\alpha(\boldsymbol{r},E,t)= \\ =\int_0^{+\infty}\Sigma_{\mathrm{s}}(\boldsymbol{r},E')f_m(\boldsymbol{r},E'\to E)\varphi_m^\alpha(\boldsymbol{r},E',t)\,\mathrm{d}E'+ \\ +\delta_{m,0}\delta_{\alpha,0}\chi(\boldsymbol{r},E)\int_0^{+\infty}\nu(\boldsymbol{r},E')\Sigma_{\mathrm{f}}(\boldsymbol{r},E')\Phi(\boldsymbol{r},E',t)\,\mathrm{d}E'+S_m^\alpha(\boldsymbol{r},E,t). \tag{A.26}$$

A.2 P_1 APPROXIMATION

Let the truncation of (A.19) to $n = 1$ be

$$\varphi(\boldsymbol{r}, E, \hat{\boldsymbol{\Omega}}, t) \cong \sum_{n=0}^{1} \sum_{\beta=-n}^{n} \varphi_n^{\beta}(\boldsymbol{r}, E, t) \cdot \mathrm{Y}_n^{\beta}(\hat{\boldsymbol{\Omega}}) = \frac{1}{4\pi}\left[\Phi(\boldsymbol{r}, E, t) + 3\hat{\boldsymbol{\Omega}} \cdot \boldsymbol{J}(\boldsymbol{r}, E, t)\right], \tag{A.27}$$

being $\boldsymbol{J}$ the neutron current, defined as

$$\boldsymbol{J}(\boldsymbol{r}, E, t) = \oint \hat{\boldsymbol{\Omega}} \cdot \varphi(\boldsymbol{r}, E, \hat{\boldsymbol{\Omega}}, t)\, \mathrm{d}\hat{\boldsymbol{\Omega}}. \tag{A.28}$$

The equations (A.27) and (A.28) are valid as by integrating the former on the angle

$$\oint \varphi(\boldsymbol{r}, E, \hat{\boldsymbol{\Omega}}, t)\, \mathrm{d}\hat{\boldsymbol{\Omega}} = \oint \frac{1}{4\pi}\left[\Phi(\boldsymbol{r}, E, t) + 3\hat{\boldsymbol{\Omega}} \cdot \boldsymbol{J}(\boldsymbol{r}, E, t)\right] \mathrm{d}\hat{\boldsymbol{\Omega}}. \tag{A.29}$$

hence

$$\Phi(\boldsymbol{r}, E, t) = \frac{1}{4\pi}\Phi(\boldsymbol{r}, E, t) \underbrace{\oint \mathrm{d}\hat{\boldsymbol{\Omega}}}_{4\pi} + 3\boldsymbol{J}(\boldsymbol{r}, E, t) \underbrace{\oint \hat{\boldsymbol{\Omega}}\, \mathrm{d}\hat{\boldsymbol{\Omega}}}_{0} = \Phi(\boldsymbol{r}, E, t) \tag{A.30}$$

which is an identity, and by multiplying (A.27) by $\hat{\boldsymbol{\Omega}}$ and integrating

$$\oint \hat{\boldsymbol{\Omega}} \cdot \varphi(\boldsymbol{r}, E, \hat{\boldsymbol{\Omega}}, t)\, \mathrm{d}\hat{\boldsymbol{\Omega}} = \oint \frac{1}{4\pi}\hat{\boldsymbol{\Omega}} \cdot \left[\Phi(\boldsymbol{r}, E, t) + 3\hat{\boldsymbol{\Omega}} \cdot \boldsymbol{J}(\boldsymbol{r}, E, t)\right] \mathrm{d}\hat{\boldsymbol{\Omega}}. \tag{A.31}$$

hence, using (A.28),

$$\boldsymbol{J}(\boldsymbol{r}, E, t) = \frac{1}{4\pi}\Phi(\boldsymbol{r}, E, t) \underbrace{\oint \hat{\boldsymbol{\Omega}}\, \mathrm{d}\hat{\boldsymbol{\Omega}}}_{0} + 3\boldsymbol{J}(\boldsymbol{r}, E, t) \underbrace{\oint \hat{\boldsymbol{\Omega}} \cdot \hat{\boldsymbol{\Omega}}\, \mathrm{d}\hat{\boldsymbol{\Omega}}}_{\frac{4\pi}{3}} = \boldsymbol{J}(\boldsymbol{r}, E, t) \tag{A.32}$$

one obtains another identity.

Substituting into (A.4) the reformulation of (A.9)

$$\mathrm{P}_n\left(\widehat{\boldsymbol{\Omega}}'\cdot\widehat{\boldsymbol{\Omega}}\right)=\mathrm{P}_n(\mu)\mathrm{P}_n(\mu')+2\sum_{\beta=1}^{n}\frac{(n-\beta)!}{(n+\beta)!}\mathrm{P}_n^{\beta}(\mu)\mathrm{P}_n^{\beta}(\mu')\cos[\beta(\eta-\eta')] \tag{A.33}$$

known as addition theorem of the spherical harmonics (Arfken, 1985, pp. 693–695), where $\widehat{\boldsymbol{\Omega}}$ is expressed as in (A.10) and (A.11). One can express the transport equation scattering term from (A.1), as

$$\begin{aligned}&\oint\int_0^{+\infty}\Sigma_{\mathrm{s}}(\boldsymbol{r},E')\varphi\left(\boldsymbol{r},E',\widehat{\boldsymbol{\Omega}}',t\right)f_{\mathrm{s}}\left(\boldsymbol{r},E'\to E,\widehat{\boldsymbol{\Omega}}'\cdot\widehat{\boldsymbol{\Omega}}\right)\mathrm{d}E'\,\mathrm{d}\widehat{\boldsymbol{\Omega}}'=\\&=\int_0^{+\infty}\Sigma_{\mathrm{s}}(\boldsymbol{r},E')\sum_{n=0}^{\infty}\frac{2n+1}{4\pi}f_n(\boldsymbol{r},E'\to E)\cdot\\&\cdot\oint\left\{\mathrm{P}_n(\mu)\mathrm{P}_n(\mu')+2\sum_{\beta=1}^{n}\frac{(n-\beta)!}{(n+\beta)!}\mathrm{P}_n^{\beta}(\mu)\mathrm{P}_n^{\beta}(\mu')\cos[\beta(\eta-\eta')]\right\}\varphi\left(\boldsymbol{r},E',\widehat{\boldsymbol{\Omega}}',t\right)\mathrm{d}\widehat{\boldsymbol{\Omega}}'\,\mathrm{d}E'.\end{aligned} \tag{A.34}$$

By substituting (A.27) into (A.34) one obtains

$$\begin{aligned}&\oint\int_0^{+\infty}\Sigma_{\mathrm{s}}(\boldsymbol{r},E')\varphi\left(\boldsymbol{r},E',\widehat{\boldsymbol{\Omega}}',t\right)f_{\mathrm{s}}\left(\boldsymbol{r},E'\to E,\widehat{\boldsymbol{\Omega}}'\cdot\widehat{\boldsymbol{\Omega}}\right)\mathrm{d}E'\,\mathrm{d}\widehat{\boldsymbol{\Omega}}'=\\&=\int_0^{+\infty}\left[\frac{1}{4\pi}\Sigma_{\mathrm{s}}(\boldsymbol{r},E')f_0(\boldsymbol{r},E'\to E)\Phi(\boldsymbol{r},E',t)+\frac{3}{4\pi}f_1(\boldsymbol{r},E'\to E)\widehat{\boldsymbol{\Omega}}\cdot\boldsymbol{J}(\boldsymbol{r},E',t)\right]\mathrm{d}E'.\end{aligned} \tag{A.35}$$

In fact, all terms of the integral on $\widehat{\boldsymbol{\Omega}}'$ reduce to one of the following kind

$$\oint\mathrm{P}_n(\mu)\,\mathrm{d}\widehat{\boldsymbol{\Omega}}=\oint\mathrm{P}_0(\mu)\mathrm{P}_n(\mu)\,\mathrm{d}\widehat{\boldsymbol{\Omega}}'=\frac{2\delta_{n,0}}{2n+1}, \tag{A.36}$$

$$\begin{aligned}\oint\widehat{\boldsymbol{\Omega}}\mathrm{P}_n(\mu)\,\mathrm{d}\widehat{\boldsymbol{\Omega}}=\int_{-1}^{1}\sqrt{1-\mu^2}\mathrm{P}_n(\mu)\,\mathrm{d}\mu\underbrace{\int_0^{2\pi}\left(\cos\eta\,\widehat{\mathbf{u}}_{\mathrm{x}}+\sin\eta\,\widehat{\mathbf{u}}_{\mathrm{y}}\right)\mathrm{d}\eta}_{0}+\\+\widehat{\mathbf{u}}_{\mathrm{z}}\int_{-1}^{1}\mu\mathrm{P}_n(\mu)\,\mathrm{d}\mu\int_0^{2\pi}\mathrm{d}\eta=\frac{4\pi}{3}\delta_{n,1}\widehat{\mathbf{u}}_{\mathrm{z}},\end{aligned} \tag{A.37}$$

$$\oint\mathrm{P}_n^{\beta}(\mu')\cos[\beta(\eta-\eta')]\,\mathrm{d}\widehat{\boldsymbol{\Omega}}'=0,\qquad\forall\beta\neq0, \tag{A.38}$$

$$\oint \widehat{\boldsymbol{\Omega}}' \mathrm{P}_n^{\beta}(\mu') \cos[\beta(\eta-\eta')]\, \mathrm{d}\widehat{\boldsymbol{\Omega}}' = \frac{4\pi}{3}\sqrt{1-\mu^2}\left(\cos\eta\, \hat{\mathbf{u}}_{\mathrm{x}} + \sin\eta\, \hat{\mathbf{u}}_{\mathrm{y}}\right)\delta_{n,1}, \tag{A.39}$$

which have been calculated according to (A.3).

Hence, for $n = 0$ the integral on $\widehat{\boldsymbol{\Omega}}'$ becomes

$$\begin{aligned}
&\oint \left\{ \underbrace{\mathrm{P}_0(\mu)\mathrm{P}_0(\mu')}_{1} + 2\underbrace{\sum_{\beta=1}^{0} \frac{(n-\beta)!}{(n+\beta)!} \mathrm{P}_0^{\beta}(\mu)\mathrm{P}_0^{\beta}(\mu') \cos[\beta(\eta-\eta')]}_{0} \right\} \varphi\left(\boldsymbol{r}, E', \widehat{\boldsymbol{\Omega}}', t\right) \mathrm{d}\widehat{\boldsymbol{\Omega}}' = \\
&\qquad = \oint \frac{1}{4\pi}\left[\Phi(\boldsymbol{r}, E, t) + 3\widehat{\boldsymbol{\Omega}} \cdot \boldsymbol{J}(\boldsymbol{r}, E, t)\right] \mathrm{d}\widehat{\boldsymbol{\Omega}}' = \\
&\qquad = \frac{1}{4\pi}\Phi(\boldsymbol{r}, E, t) \underbrace{\oint \mathrm{d}\widehat{\boldsymbol{\Omega}}'}_{4\pi} + \frac{3}{4\pi}\boldsymbol{J}(\boldsymbol{r}, E, t) \underbrace{\oint \widehat{\boldsymbol{\Omega}}\, \mathrm{d}\widehat{\boldsymbol{\Omega}}'}_{0} = \Phi(\boldsymbol{r}, E, t),
\end{aligned} \tag{A.40}$$

and for $n = 1$ the integral on $\widehat{\boldsymbol{\Omega}}'$ becomes

$$\begin{aligned}
&\oint \left\{ \mathrm{P}_1(\mu)\mathrm{P}_1(\mu') + 2\sum_{\beta=1}^{n} \frac{(n-\beta)!}{(n+\beta)!} \mathrm{P}_1^{\beta}(\mu)\mathrm{P}_1^{\beta}(\mu') \cos[\beta(\eta-\eta')] \right\} \varphi\left(\boldsymbol{r}, E', \widehat{\boldsymbol{\Omega}}', t\right) \mathrm{d}\widehat{\boldsymbol{\Omega}}' = \\
&\qquad = \mu\frac{\Phi(\boldsymbol{r}, E, t)}{4\pi} \underbrace{\oint \mu'\, \mathrm{d}\widehat{\boldsymbol{\Omega}}'}_{0} + \mu\frac{3\boldsymbol{J}(\boldsymbol{r}, E, t)}{4\pi} \oint \mu' \widehat{\boldsymbol{\Omega}}'\, \mathrm{d}\widehat{\boldsymbol{\Omega}}' + \\
&\qquad + \sqrt{1-\mu^2}\frac{\Phi(\boldsymbol{r}, E, t)}{4\pi} \underbrace{\oint \sqrt{1-\mu'^2}\cos(\eta-\eta')\, \mathrm{d}\widehat{\boldsymbol{\Omega}}'}_{0} + \\
&\qquad + \frac{3\boldsymbol{J}(\boldsymbol{r}, E, t)}{4\pi}\sqrt{1-\mu^2} \oint \sqrt{1-\mu'^2}\cos(\eta-\eta')\, \widehat{\boldsymbol{\Omega}}'\, \mathrm{d}\widehat{\boldsymbol{\Omega}}' = \\
&= \frac{3\boldsymbol{J}(\boldsymbol{r}, E, t)}{4\pi}\left[\mu \oint \mu' \widehat{\boldsymbol{\Omega}}'\, \mathrm{d}\widehat{\boldsymbol{\Omega}}' + \sqrt{1-\mu^2} \oint \sqrt{1-\mu'^2}\cos(\eta-\eta')\, \widehat{\boldsymbol{\Omega}}'\, \mathrm{d}\widehat{\boldsymbol{\Omega}}'\right] = \\
&= \frac{3\boldsymbol{J}(\boldsymbol{r}, E, t)}{4\pi}\left(\frac{4\pi}{3}\mu\hat{\mathbf{u}}_{\mathrm{z}} + \frac{4\pi}{3}\sqrt{1-\mu^2}\cos\eta\, \hat{\mathbf{u}}_{\mathrm{x}} + \frac{4\pi}{3}\sqrt{1-\mu^2}\sin\eta\, \hat{\mathbf{u}}_{\mathrm{y}}\right) = \widehat{\boldsymbol{\Omega}} \cdot \boldsymbol{J},
\end{aligned} \tag{A.41}$$

By substituting (A.27) and (A.35) into the transport equation (A.1) one gets

$$\begin{aligned}
&\frac{1}{v(E)}\frac{\partial}{\partial t}\left[\Phi(\boldsymbol{r},E,t)+3\widehat{\boldsymbol{\Omega}}\cdot\boldsymbol{J}(\boldsymbol{r},E,t)\right]+\widehat{\boldsymbol{\Omega}}\cdot\boldsymbol{\nabla}\left[\Phi(\boldsymbol{r},E,t)+3\widehat{\boldsymbol{\Omega}}\cdot\boldsymbol{J}(\boldsymbol{r},E,t)\right]+\\
&\qquad+\Sigma_{\mathrm{t}}(\boldsymbol{r},E)\left[\Phi(\boldsymbol{r},E,t)+3\widehat{\boldsymbol{\Omega}}\cdot\boldsymbol{J}(\boldsymbol{r},E,t)\right]=\\
&=\int_0^{+\infty}\left[\Sigma_{\mathrm{s}}(\boldsymbol{r},E')f_0(\boldsymbol{r},E'\to E)\Phi(\boldsymbol{r},E',t)+\right.\\
&\left.+3\Sigma_{\mathrm{s}}(\boldsymbol{r},E')f_1(\boldsymbol{r},E'\to E)\widehat{\boldsymbol{\Omega}}\cdot\boldsymbol{J}(\boldsymbol{r},E',t)\right]\mathrm{d}E'+\\
&+\chi(\boldsymbol{r},E)\int_0^{+\infty}\nu(\boldsymbol{r},E')\Sigma_{\mathrm{f}}(\boldsymbol{r},E')\Phi(\boldsymbol{r},E',t)\mathrm{d}E'+4\pi\cdot S\left(\boldsymbol{r},E,\widehat{\boldsymbol{\Omega}},t\right).
\end{aligned}\tag{A.42}$$

The first moment of the scattering functions can be calculated based on (A.5)

$$f_1(\boldsymbol{r},E'\to E)=2\pi\int_{-1}^{1}f_{\mathrm{s}}\left(\boldsymbol{r},E'\to E,\widehat{\boldsymbol{\Omega}}'\cdot\widehat{\boldsymbol{\Omega}}\right)\cdot\left(\widehat{\boldsymbol{\Omega}}'\cdot\widehat{\boldsymbol{\Omega}}\right)\mathrm{d}\left(\widehat{\boldsymbol{\Omega}}'\cdot\widehat{\boldsymbol{\Omega}}\right)=\overline{\mu_0}(\boldsymbol{r},E'\to E),\tag{A.43}$$

while the 0-th moment can be included into the scattering term, obtaining a scattering matrix:

$$\Sigma_{\mathrm{s}}(\boldsymbol{r},E')f_0(\boldsymbol{r},E'\to E)=\Sigma_{\mathrm{s}}(\boldsymbol{r},E')f_{\mathrm{s}}(\boldsymbol{r},E'\to E)\triangleq\Sigma_{\mathrm{s}}(\boldsymbol{r},E'\to E).\tag{A.44}$$

After substitution of (A.43) and (A.44), the P_1 approximation of the transport equation is described by the equation (continuity equation) obtained by integrating (A.42) over $\widehat{\boldsymbol{\Omega}}$

$$\begin{aligned}
&\frac{1}{v(E)}\frac{\partial\Phi(\boldsymbol{r},E,t)}{\partial t}+\boldsymbol{\nabla}\cdot\boldsymbol{J}(\boldsymbol{r},E,t)+\Sigma_{\mathrm{t}}(\boldsymbol{r},E)\Phi(\boldsymbol{r},E,t)=\\
&\qquad=\int_0^{+\infty}\Sigma_{\mathrm{s}}(\boldsymbol{r},E'\to E)\Phi(\boldsymbol{r},E',t)\,\mathrm{d}E'+\\
&\qquad+\chi(\boldsymbol{r},E)\int_0^{+\infty}\nu(\boldsymbol{r},E')\Sigma_{\mathrm{f}}(\boldsymbol{r},E')\Phi(\boldsymbol{r},E',t)\mathrm{d}E'+\oint S\left(\boldsymbol{r},E,\widehat{\boldsymbol{\Omega}},t\right)\mathrm{d}\widehat{\boldsymbol{\Omega}}
\end{aligned}\tag{A.45}$$

and by the equation (current equation) obtained by multiplication by $\widehat{\boldsymbol{\Omega}}$ of (A.42) followed by integration over the same variable

$$\begin{aligned}\frac{1}{v(E)}\frac{\partial \boldsymbol{J}(\boldsymbol{r},E,t)}{\partial t}+\frac{1}{3}\boldsymbol{\nabla}\Phi(\boldsymbol{r},E,t)+\Sigma_{\mathrm{t}}(\boldsymbol{r},E)\boldsymbol{J}(\boldsymbol{r},E,t)=\\ =\int_0^{+\infty}\overline{\mu_0}(\boldsymbol{r},E'\to E)\Sigma_{\mathrm{s}}(\boldsymbol{r},E')\boldsymbol{J}(\boldsymbol{r},E',t)\,\mathrm{d}E'+\\ +\oint\widehat{\boldsymbol{\Omega}}\cdot S\big(\boldsymbol{r},E,\widehat{\boldsymbol{\Omega}},t\big)\,\mathrm{d}\widehat{\boldsymbol{\Omega}}.\end{aligned} \tag{A.46}$$

The source term of the current equation vanishes if the source is isotropic.

APPENDIX B CONSISTENT P APPROXIMATION

Based on a rigorous formulation of the multigroup XSs, these are direction-dependent quantities. Such dependence does not originates from the nuclear data, but is a consequence of the averaging with the directional neutron flux. An usual formulation of the multigroup theory drops such XS directionality with the introduction of an assumption: direction and energy components of the neutron flux are separable. A multigroup P formulation (Appendix A) featuring such assumption is called "inconsistent P approximation", opposed to the "consistent P approximation" (Bell and Glasstone, 1970, pp. 239–242) which does not require it and described in this appendix.

As a first step, one writes the neutron transport equation (2.5) with the scattering term expanded into spherical harmonics, as in (A.17):

$$\begin{aligned}\frac{1}{v(E)}\frac{\partial\varphi\left(\boldsymbol{r},E,\widehat{\boldsymbol{\Omega}},t\right)}{\partial t}+\widehat{\boldsymbol{\Omega}}\cdot\boldsymbol{\nabla}\varphi\left(\boldsymbol{r},E,\widehat{\boldsymbol{\Omega}},t\right)+\Sigma_{\mathrm{t}}(\boldsymbol{r},E)\varphi\left(\boldsymbol{r},E,\widehat{\boldsymbol{\Omega}},t\right)=\\ =\int_0^{+\infty}\Sigma_{\mathrm{s}}(\boldsymbol{r},E')\sum_{n=0}^{\infty}f_n(\boldsymbol{r},E'\to E)\sum_{\beta=-n}^{n}\mathrm{Y}_n^{\beta}\left(\widehat{\boldsymbol{\Omega}}\right)\varphi_n^{\beta}(\boldsymbol{r},E',t)\,\mathrm{d}E'+\\ +\frac{\chi(\boldsymbol{r},E)}{4\pi}\oint\int_0^{+\infty}\nu(\boldsymbol{r},E')\Sigma_{\mathrm{f}}(\boldsymbol{r},E')\varphi\left(\boldsymbol{r},E',\widehat{\boldsymbol{\Omega}}',t\right)\mathrm{d}E'\,\mathrm{d}\widehat{\boldsymbol{\Omega}}'\\ +S\left(\boldsymbol{r},E,\widehat{\boldsymbol{\Omega}},t\right).\end{aligned}\tag{B.1}$$

The multigroup version of (B.1) is obtained by integrating over each group

$$\begin{aligned}\int_{E_{g-1}}^{E_g}\frac{1}{v(E)}\frac{\partial\varphi\left(\boldsymbol{r},E,\widehat{\boldsymbol{\Omega}},t\right)}{\partial t}\,\mathrm{d}E+\widehat{\boldsymbol{\Omega}}\cdot\boldsymbol{\nabla}\varphi^{(g)}\left(\boldsymbol{r},\widehat{\boldsymbol{\Omega}},t\right)+\int_{E_{g-1}}^{E_g}\Sigma_{\mathrm{t}}(\boldsymbol{r},E)\varphi\left(\boldsymbol{r},E,\widehat{\boldsymbol{\Omega}},t\right)\mathrm{d}E=\\ =\int_{E_{g-1}}^{E_g}\int_0^{+\infty}\Sigma_{\mathrm{s}}(\boldsymbol{r},E')\sum_{n=0}^{\infty}f_n(\boldsymbol{r},E'\to E)\sum_{\beta=-n}^{n}\mathrm{Y}_n^{\beta}\left(\widehat{\boldsymbol{\Omega}}\right)\varphi_n^{\beta}(\boldsymbol{r},E',t)\,\mathrm{d}E'\,\mathrm{d}E+\\ +\frac{\chi^{(g)}(\boldsymbol{r})}{4\pi}\int_0^{+\infty}\nu(\boldsymbol{r},E')\Sigma_{\mathrm{f}}(\boldsymbol{r},E')\Phi(\boldsymbol{r},E',t)\,\mathrm{d}E'+S^{(g)}\left(\boldsymbol{r},\widehat{\boldsymbol{\Omega}},t\right)\end{aligned}\tag{B.2}$$

with

$$\varphi^{(g)}\left(\boldsymbol{r},\widehat{\boldsymbol{\Omega}},t\right) \triangleq \int_{E_{g-1}}^{E_g} \varphi\left(\boldsymbol{r},E,\widehat{\boldsymbol{\Omega}},t\right)\mathrm{d}E, \tag{B.3}$$

$$S^{(g)}\left(\boldsymbol{r},\widehat{\boldsymbol{\Omega}},t\right) \triangleq \int_{E_{g-1}}^{E_g} S\left(\boldsymbol{r},E,\widehat{\boldsymbol{\Omega}},t\right)\mathrm{d}E. \tag{B.4}$$

One can observe that direction dependence in XSs appears only for the total and the scattering ones; in fact, as the fission XS is associated to the scalar neutron flux, whose directionality has already been removed, it is sufficient defining

$$\nu\Sigma_{\mathrm{f}}^{(g)}(\boldsymbol{r},t) \triangleq \frac{\int_{E_{g-1}}^{E_g} \nu(\boldsymbol{r},E')\Sigma_{\mathrm{f}}(\boldsymbol{r},E')\Phi(\boldsymbol{r},E',t)\,\mathrm{d}E'}{\int_{E_{g-1}}^{E_g} \Phi(\boldsymbol{r},E',t)\,\mathrm{d}E'}. \tag{B.5}$$

in order not to have the direction dependence in the multigroup fission XS.

In addition, direction dependence appears for the neutron velocity, but also in this consistent formulation is better applying (2.17) rather than having a time-dependent neutron velocity.

By expanding with (A.19) the neutron flux of the collision term, (B.2) hence becomes

$$\begin{aligned}\frac{1}{v^{(g)}}\frac{\partial\varphi^{(g)}\left(\boldsymbol{r},\widehat{\boldsymbol{\Omega}},t\right)}{\partial t} &+ \widehat{\boldsymbol{\Omega}}\cdot\boldsymbol{\nabla}\varphi^{(g)}\left(\boldsymbol{r},\widehat{\boldsymbol{\Omega}},t\right) + \int_{E_{g-1}}^{E_g}\Sigma_{\mathrm{t}}(\boldsymbol{r},E)\sum_{n=0}^{\infty}\sum_{\beta=-n}^{n}\varphi_n^{\beta}(\boldsymbol{r},E,t)\mathrm{Y}_n^{\beta}\left(\widehat{\boldsymbol{\Omega}}\right)\mathrm{d}E = \\ &= \int_{E_{g-1}}^{E_g}\int_{0}^{+\infty}\Sigma_{\mathrm{s}}(\boldsymbol{r},E')\sum_{n=0}^{\infty}f_n(\boldsymbol{r},E'\to E)\sum_{\beta=-n}^{n}\mathrm{Y}_n^{\beta}\left(\widehat{\boldsymbol{\Omega}}\right)\varphi_n^{\beta}(\boldsymbol{r},E',t)\,\mathrm{d}E'\,\mathrm{d}E + \\ &+ \frac{\chi^{(g)}(\boldsymbol{r})}{4\pi}\sum_{g'}\nu\Sigma_{\mathrm{f}}^{(g)}(\boldsymbol{r},t)\Phi^{(g)}(\boldsymbol{r},t) + S^{(g)}\left(\boldsymbol{r},\widehat{\boldsymbol{\Omega}},t\right).\end{aligned} \tag{B.6}$$

With the definitions

$$\varphi_n^{\beta,(g)}(\boldsymbol{r},t) \triangleq \int_{E_{g-1}}^{E_g} \varphi_n^{\beta}(\boldsymbol{r},E,t)\,\mathrm{d}E, \tag{B.7}$$

$$\Sigma_{\mathrm{t},n}^{\beta,(g)}(\boldsymbol{r},t) \triangleq \frac{\int_{E_{g-1}}^{E_g} \Sigma_{\mathrm{t}}(\boldsymbol{r},E)\varphi_n^{\beta}(\boldsymbol{r},E,t)\,\mathrm{d}E}{\varphi_n^{\beta,(g)}(\boldsymbol{r},t)}, \tag{B.8}$$

$$\Sigma_{\mathrm{s},n}^{\beta,(g'\to g)}(\boldsymbol{r},t) \triangleq \frac{\int_{E_{g'-1}}^{E_{g'}} \Sigma_{\mathrm{s}}(\boldsymbol{r},E')\varphi_n^{\beta}(\boldsymbol{r},E',t)\int_{E_{g-1}}^{E_g} f_n(\boldsymbol{r},E'\to E)\,\mathrm{d}E\;\mathrm{d}E'}{\varphi_n^{\beta,(g')}(\boldsymbol{r},t)}, \tag{B.9}$$

which keep the directionality of the XSs, as there is now a different multigroup XS for each spherical harmonic, and moving the absorption term from the left to the right hand side, (B.6) can be rewritten as

$$\begin{aligned}\frac{1}{v^{(g)}}\frac{\partial\varphi^{(g)}(\boldsymbol{r},\widehat{\boldsymbol{\Omega}},t)}{\partial t} &+ \widehat{\boldsymbol{\Omega}}\cdot\boldsymbol{\nabla}\varphi^{(g)}(\boldsymbol{r},\widehat{\boldsymbol{\Omega}},t) = \\ &= \sum_{n=0}^{\infty}\sum_{\beta=-n}^{n} \mathrm{Y}_n^{\beta}(\widehat{\boldsymbol{\Omega}})\sum_{g'}\left[\Sigma_{\mathrm{s},n}^{\beta,(g'\to g)}(\boldsymbol{r},t) - \Sigma_{\mathrm{t},n}^{\beta,(g)}(\boldsymbol{r},E)\right]\varphi_n^{\beta,(g)}(\boldsymbol{r},t) + \\ &+ \frac{\chi^{(g)}(\boldsymbol{r})}{4\pi}\sum_{g'}\nu\Sigma_{\mathrm{f}}^{(g)}(\boldsymbol{r},t)\Phi^{(g)}(\boldsymbol{r},t) + S^{(g)}(\boldsymbol{r},\widehat{\boldsymbol{\Omega}},t).\end{aligned} \tag{B.10}$$

The final expression for the multigroup transport equation is obtained by adding and subtracting the same term on both sides

$$\begin{aligned}&\frac{1}{v^{(g)}}\frac{\partial\varphi^{(g)}(\boldsymbol{r},\widehat{\boldsymbol{\Omega}},t)}{\partial t} + \widehat{\boldsymbol{\Omega}}\cdot\boldsymbol{\nabla}\varphi^{(g)}(\boldsymbol{r},\widehat{\boldsymbol{\Omega}},t) + \Sigma_{\mathrm{t}}^{(g)}(\boldsymbol{r},E)\varphi^{(g)}(\boldsymbol{r},\widehat{\boldsymbol{\Omega}},t) = \\ &= \sum_{n=0}^{\infty}\sum_{\beta=-n}^{n} \mathrm{Y}_n^{\beta}(\widehat{\boldsymbol{\Omega}})\sum_{g'}\left\{\Sigma_{\mathrm{s},n}^{\beta,(g'\to g)}(\boldsymbol{r},t) + \left[\Sigma_{\mathrm{t}}(\boldsymbol{r},E) - \Sigma_{\mathrm{t},n}^{\beta,(g)}(\boldsymbol{r},E)\right]\right\}\varphi_n^{\beta,(g)}(\boldsymbol{r},t) + \\ &+ \frac{\chi^{(g)}(\boldsymbol{r})}{4\pi}\sum_{g'}\nu\Sigma_{\mathrm{f}}^{(g)}(\boldsymbol{r},t)\Phi^{(g)}(\boldsymbol{r},t) + S^{(g)}(\boldsymbol{r},\widehat{\boldsymbol{\Omega}},t).\end{aligned} \tag{B.11}$$

The form of the equation (B.11) is the same of the inconsistent P approximation of the multigroup transport equation, but the value of the scattering XS is different. With the flux moments calculated with (A.18) one easily calculates the multigroup flux moments appearing in (B.11). The latter can then be used to determine the multigroup XSs for each n and β.

It is interesting observing that, up to this point, the equation is correct (except for the neutron velocity approximation introduced), i.e. it is equivalent to the neutron transport equation. Nevertheless, $\Sigma_{\mathrm{t}}^{(g)}$ has not been defined yet.

The consistent P approximation assumes, for all n and β

$$\Sigma_{\mathrm{t}}^{(g)} = \Sigma_{\mathrm{t},0}^{0,(g)} = \frac{\int_{E_{g-1}}^{E_g} \Sigma_{\mathrm{t}}(\boldsymbol{r},E)\varphi_0^0(\boldsymbol{r},E,t)\,\mathrm{d}E}{\varphi_0^{0,(g)}(\boldsymbol{r},t)}; \tag{B.12}$$

however, according to (A.18), it is

$$\varphi_0^0(\boldsymbol{r},E,t) = \oint \varphi\left(\boldsymbol{r},E,\widehat{\boldsymbol{\Omega}},t\right)\cdot\overline{\mathrm{Y}_0^0}\left(\widehat{\boldsymbol{\Omega}}\right)\mathrm{d}\widehat{\boldsymbol{\Omega}} = \sqrt{\frac{1}{4\pi}}\oint \varphi\left(\boldsymbol{r},E,\widehat{\boldsymbol{\Omega}},t\right)\mathrm{d}\widehat{\boldsymbol{\Omega}} = \sqrt{\frac{1}{4\pi}}\Phi(\boldsymbol{r},E,t), \tag{B.13}$$

which leads to

$$\Sigma_{\mathrm{t}}^{(g)} = \frac{\int_{E_{g-1}}^{E_g} \Sigma_{\mathrm{t}}(\boldsymbol{r},E)\Phi(\boldsymbol{r},E,t)\,\mathrm{d}E}{\Phi^{(g)}(\boldsymbol{r},t)}. \tag{B.14}$$

It is possible setting $\Sigma_{\mathrm{t}}^{(g)}$ to other values, obtaining different approximations, as the “extended transport approximation” (Bell and Glasstone, 1970, pp. 241–242).

BIBLIOGRAPHY

Akbari, M., Minuchehr, A., Zolfaghari, A., Khoshahval, F., 2012. An investigation for an optimized neutron energy-group structure in thermal lattices using Particle Swarm Optimization. Annals of Nuclear Energy 47, 53–61. 10.1016/j.anucene.2012.02.016.

Alcouffe, R.E., Baker, R.S., 2009. PARTISN: A Time-Dependent, Parallel Neutral Particle Transport Code System. LA-UR-08-07258.

Alcouffe, R.E., Baker, R.S., Brinkley, F.W., Marr, D.R., O'Dell, R.D., Walters, W.F., 1995. DANTSYS: A Diffusion Accelerated Neutral Particle Transport Code System. LANL Report LA-12969-M. Los Alamos National Laboratory.

Andriolo, L., 2015. Impact of innovative sphere-pac fuels on safety performances of sodium cooled fast reactors. PhD thesis, Grenoble, France.

Arfken, G.B., 1985. Mathematical Methods for Physicists. Elsevier Science, Orlando, FL, USA.

Askew, J.R., Fayers, F.J., Kemshell, P.B., 1966. A general description of the lattice code WIMS. J. Brit. Nucl. En. Soc. (5), 564.

Bäck, T., Schwefel, H.-P., 1993. An Overview of Evolutionary Algorithms for Parameter Optimization. Evolutionary Computation 1 (1), 1–23. 10.1162/evco.1993.1.1.1.

Bang-Jensen, J., Gutin, G., Yeo, A., 2004. When the greedy algorithm fails. Discrete Optimization 1 (2), 121–127. 10.1016/j.disopt.2004.03.007.

Bell, G.I., Glasstone, S., 1970. Nuclear reactor theory. Van Nostrand Reinhold, New York, London.

Bianchi, L., Dorigo, M., Gambardella, L.M., Gutjahr, W.J., 2009. A survey on metaheuristics for stochastic combinatorial optimization. Nat. Comput. 8 (2), 239–287. 10.1007/s11047-008-9098-4.

Blickle, T., Thiele, L., 1996. A comparison of selection schemes used in evolutionary algorithms. Evolutionary Computation 4 (4), 361–394.

Blum, C., Roli, A., 2003. Metaheuristics in combinatorial optimization. ACM Comput. Surv. 35 (3), 268–308. 10.1145/937503.937505.

Bohl, W.R., Luck, L.B., 1990. SIMMER-II: A Computer Program for LMFBR Disrupted Core Analysis. LANL Report LA-11415-MS. Los Alamos National Laboratory.

Bondarenko, I.I. (Ed.), 1964. Group constants for nuclear reactor calculations. Consultants Bureau, New York.

Bortot, S., Alvarez y Velarde, F., Fridman, E., Cruzado, I.G., Herranz, N.G., López, D., Mikityuk, K., Panadero, A.-L., Pelloni, S., Ponomarev, A., Sciora, P., Seubert, A., Tsige-Tamirat, H., Vasile, A., 2015. European benchmark on the ASTRID-like low-void-effect core characterization: Neutronic parameters and safety coefficients, in: Proc. ICAPP 2015, Nice, France. May 3-6, 2015. American Nuclear Society, pp. 3–6.

Buiron, L., Vasile, A., Sunderland, R., Glinatsis, G., Krepel, J., Mikityuk, K., Rineiski, A., Vezzoni, B., Gabrielli, F., Garcia Herranz, N., Ochoa, R., Martin Fuertes, F., Polidoro, F., Tsige-Tamirat, H., Massara, S., 2013. CP ESFR: Collaborative Project for a European Sodium Fast Reactor. Presentation. http://www.iaea.org/inis/collection/NCLCollectionStore/_Public/45/089/45089484.pdf?r=1.

Cacuci, D.G. (Ed.), 2010. Handbook of nuclear engineering. Springer, New York, London.

Chadwick, M.B., Obložinský, P., Herman, M., Greene, N.M., McKnight, R.D., Smith, D.L., Young, P.G., MacFarlane, R.E., Hale, G.M., Frankle, S.C., Kahler, A.C., Kawano, T., Little, R.C., Madland, D.G., Moller, P., Mosteller, R.D., Page, P.R., Talou, P., Trellue, H., White, M.C., Wilson, W.B., Arcilla, R., Dunford, C.L., Mughabghab, S.F., Pritychenko, B., Rochman, D., Sonzogni, A.A., Lubitz, C.R., Trumbull, T.H., Weinman, J.P., Brown, D.A., Cullen, D.E., Heinrichs, D.P., McNabb, D.P., Derrien, H., Dunn, M.E., Larson, N.M., Leal, L.C., Carlson, A.D., Block, R.C., Briggs, J.B., Cheng, E.T., Huria, H.C., Zerkle, M.L., Kozier, K.S., Courcelle, A., Pronyaev, V., van der Marck, S.C., 2006. ENDF/B-VII.0: Next Generation Evaluated Nuclear Data Library for Nuclear Science and Technology. Nuclear Data Sheets 107 (12), 2931–3060. 10.1016/j.nds.2006.11.001.

Coppa, G.G.M., Dulla, S., Ravetto, P., 2010. The time-dependent P1 model for the neutronics of multiplying systems: a review. Kerntechnik 75 (4), 200–205. 10.3139/124.110084.

Cormen, T.H., 2001. Introduction to algorithms, 2nd ed. MIT Press, Cambridge, Mass., London.

Davis, L.E., 1991. Handbook of genetic algorithms. Van Nostrand Reinhold, New York.

Doriath, J.Y., McCallien, C.W., Kiefhaber, E., Wehmann, U., Rieunier, J.M., 1993. ERANOS 1: The advanced European system of codes for reactor physics calculations, in: Proc. Int. Conf. on Mathematical methods and supercomputing in nuclear applications, Karlsruhe. April 19-23.

Douglass, S., Rahnema, F., 2012. Consistent generalized energy condensation theory. Annals of Nuclear Energy 40 (1), 200–214. 10.1016/j.anucene.2011.09.001.

Duderstadt, J.J., Hamilton, L.J., 1976. Nuclear reactor analysis. Wiley, New York, London.

Dulla, S., 2017. Differences between direct and adjoint problem solution. Personal communication.

European Commission, 2017. HORIZON 2020: The EU Framework Programme for Research and Innovation. https://ec.europa.eu/programmes/horizon2020/.

European Commission - CORDIS, 2017. SAMOFAR: A Paradigm Shift in Reactor Safety with the Molten Salt Fast Reactor. European Commission. http://cordis.europa.eu/project/rcn/196909_en.html.

EVOL project, 2011. Molten Salt Fast Reactor: Reference configuration.

Fiorini, G.L., 2009. European Commission - 7th Framework programme The Collaborative Project on European Sodium Fast Reactor (CP ESFR), in: Proc. FISA 2009. 7th European Commission conference on EURATOM research and training in reactor systems, Prague, Czech Republic. June 22-24, 2009.

Fiorini, G.L., Vasile, A., 2011. European Commission - 7th Framework Programme: The Collaborative Project on European Sodium Fast Reactor (CP ESFR). Nuclear Engineering and Design 241 (9), 3461–3469. 10.1016/j.nucengdes.2011.01.052.

Fleming, P.J., Wallace, J.J., 1986. How not to lie with statistics: The correct way to summarize benchmark results. Commun. ACM 29 (3), 218–221. 10.1145/5666.5673.

Fraser, A., Burnell, D., 1970. Computer models in genetics, McGraw-Hill, New York.

Gabrielli, F., Rineiski, A., Marchetti, M., Massone, M., Kriventsev, V., 2014. Study of the effect of heterogeneity of the control rods in the Phénix reactor, in: Proc. Int. Conf. PHYSOR 2014, Kyoto, Japan. September 28 - October 3, 2014.

Goldberg, D.E., 1989. Genetic algorithms in search, optimization, and machine learning. Addison-Wesley, Reading, Mass., Wokingham.

Goldberg, D.E., Deb, K., 1991. A Comparative Analysis of Selection Schemes Used in Genetic Algorithms, in: Foundations of Genetic Algorithms, pp. 69–93.

Hébert, A., Santamarina, A., 2008. Refinement of the Santamarina-Hfaiedh energy mesh between 22.5 eV and 11.4 keV, in: Proc. Int. Conf. PHYSOR 2008, Interlaken, Switzerland. September 14-19, 2008. Paul Scherrer Institut, Villigen, Switzerland.

Hfaiedh, N., Santamarina, A., 2005. Determination of the optimized SHEM mesh for neutron transport calculations, in: Proc. Int. Conf. M&C 2005, Avignon, France. September 12-15, 2005.

Holland, J.H., 1962. Outline for a Logical Theory of Adaptive Systems. Journal of the ACM 9 (3), 297–314. 10.1145/321127.321128.

Holland, J.H., 1975. Adaptation in natural and artificial systems: An introductory analysis with applications to biology, control, and artificial intelligence. University of Michigan Press, Ann Arbor, Mich.

International Atomic Energy Agency, 2014. Benchmark analyses on the control rod withdrawal tests performed during the Phénix end-of-life experiments. IAEA TECDOCS 1742, Vienna, Austria.

Kidman, R.B., Schenter, R.E., Hardie, R.W., Little, W.W., 1972. The Shielding Factor Method of Generating Multigroup Cross Sections for Fast Reactor Analysis. Nuclear Science and Engineering 48 (2), 189–201. 10.13182/NSE72-A22470.

Kiefhaber, E., 2000. Updating of an 11-groups nuclear cross section set for transmutation applications, in: Mühl, B. (Ed.), Projekt Nukleare Sicherheitsfoschung. Jahresbericht 1999, FZKA-6480, Karlsruhe.

Kim, K.S., Williams, M.L., Wiarda, D., Clarno, K.T., Liu, Y., 2017. Development of the CASL-VERA V4.2m5 MPACT 51-group Libraries with ENDF/B-VII.0 and VII.1, in: Proc. Int. Conf. M&C 2017, Jeju, Korea. April 16-20, 2017. Korean Nuclear Society (KNS) / American Nuclear Society (ANS).

Knott, D., Yamamoto, A., 2010. Lattice Physics Computations, in: Cacuci, D.G. (Ed.), Handbook of nuclear engineering, II. Springer, New York, London, pp. 913–1239.

Knuth, D.E., 1997-2011. The art of computer programming. Volumes 1-4a. Addison-Wesley, Upper Saddle River.

Kondo, Sa., Yamano, H., Suzuki, T., Tobita, Y., Fujita, S., Cao, X., Kamiyama, K., Morita, K., Fischer, E.A., Brear, D.J., Shirakawa, N., Mizuno, M., Hosono, S., Kondo, T., Maschek, W., Kiefhaber, E., Buckel, G., Rineiski, A., Flad, M., Coste, P., Pigny, S., Louvet, J., Cadiou, T., 2000. SIMMER-III: A Computer Program for LMFR Core Disruptive Accident Analysis, Version 2.H Model Summary and Program Description. TN9400 2001-002. Japan Nuclear Cycle Development Institute.

Koning, A., Forrest, R., Kellet, M., Mills, R., Henriksson, H., Rugama, Y., 2006. The JEFF-3.1 Nuclear Data Library. JEFF Report 21. Nuclear Energy Agency.

Kramer, O., 2017. Genetic algorithm essentials. Springer, Cham.

Krepel, J., Pelloni, S., Bortot, S., Panadero, A.-L., Mikityuk, K., 2015. Mapping of Sodium Void Worth and Doppler Effect for Sodium-cooled Fast Reactor, in: Proc. ICAPP 2015, Nice, France. May 3-6, 2015. American Nuclear Society, pp. 677–684.

Kriventsev, V., Gabrielli, F., Rineiski, A., 2014. Simulation of Phénix control rod withdrawal experiments with SIMMER-IV, in: Proc. Int. Conf. PHYSOR 2014, Kyoto, Japan. September 28 - October 3, 2014.

Larsen, E.W., Morel, J.E., Lou, J., 2017. "Nonlocal" Diffusion Coefficients for Neutronic Systems Containing Voided Subregions, in: Proc. Int. Conf. M&C 2017, Jeju, Korea. April 16-20, 2017. Korean Nuclear Society (KNS) / American Nuclear Society (ANS).

Marchetti, M., Gabrielli, F., Rineiski, A., Maschek, W., 2014. The SIMMER/PARTISN Capability for Transient Analysis, in: Proc. Int. Conf. PHYSOR 2014, Kyoto, Japan. September 28 - October 3, 2014.

Maschek, W., Rineiski, A., Flad, M., Liu, P., Chen, X.-N., Tobita, Y., Yamano, H., Suzuki, T., Fujita, S., Kamiyama, K., Pigny, S., Cadiou, T., Morita, K., Bandini, G., 2008. The SIMMER safety code system and its validation efforts for fast reactor application, in: Proc. Int. Conf. PHYSOR 2008, Interlaken, Switzerland. September 14-19, 2008. Paul Scherrer Institut, Villigen, Switzerland.

Massone, M., Gabrielli, F., Rineiski, A., 2014. SIMMER extension for cross-section collapsing introduction, in: Proc. IYNC 2014, Burgos, Spain. July 6-12, 2014.

Massone, M., Gabrielli, F., Rineiski, A., 2017a. A genetic algorithm for multigroup energy structure search. Annals of Nuclear Energy 105, 369–387. 10.1016/j.anucene.2017.03.022.

Massone, M., Gabrielli, F., Rineiski, A., 2017b. SIMMER Extension for Multigroup Energy Structure Search using Genetic Algorithm, in: Proc. Int. Conf. M&C 2017, Jeju, Korea. April 16-20, 2017. Korean Nuclear Society (KNS) / American Nuclear Society (ANS).

Massone, M., Gabrielli, F., Rineiski, A., 2017c. SIMMER Extension for Multigroup Energy Structure Search using Genetic Algorithm with different fitness functions. Nuclear Engineering and Technology (49), 1250–1258. 10.1016/j.net.2017.07.012.

Mc Ginley, B., Morgan, F., O'Riordan, C., 2008. Maintaining diversity through adaptive selection, crossover and mutation, in: Proceedings of the 10th annual conference on Genetic and evolutionary computation. Genetic and Evolutionary Computation Conference 2008, Atlanta, GA, USA. ACM, New York, NY, p. 1127.

Miller, B.L., Goldberg, D.E., 1995. Genetic algorithms, tournament selection, and the effects of noise. Complex systems 9, 193–212.

Miller, B.L., Goldberg, D.E., 1996. Genetic algorithms, selection schemes, and the varying effects of noise. Evolutionary Computation 4 (2), 113–131.

Monti, S. (Ed.), 2015. Proceedings of an International Conference on Fast Reactors and Related Fuel Cycles (FR13). International Atomic Energy Agency, Vienna.

Mosca, P., 2009. Conception et développement d'un mailleur énergétique adaptatif pour la génération des bibliothèques multigroupes des codes de transport. Ph. D. Thesis, Paris, France.

Mosca, P., Mounier, C., 2008. Adaptive energy mesh constructor for multigroup libraries of the deterministic transport code APOLLO2, in: Proc. Int. Conf. PHYSOR 2008, Interlaken, Switzerland. September 14-19, 2008. Paul Scherrer Institut, Villigen, Switzerland, pp. 241–248.

Mosca, P., Mounier, C., Sanchez, R., Arnaud, G., 2011a. An adaptive energy mesh constructor for multigroup library generation for transport codes. Nuclear Science and Engineering 167 (1), 40–60.

Mosca, P., Taofiki, A., Bellier, P., Prévost, A., 2011b. Energy Mesh Optimisation For Multi-level Calculation Scheme, in: Proc. Int. Conf. M&C 2011, Rio de Janeiro, Brazil. May 8-12, 2011. Latin American Section (LAS) / American Nuclear Society (ANS).

Mühlenbein, H., 1995. The Science of Breeding and its Application to Genetic Algorithms, in: Winter, G., Périaux, J., Galán, M., Cuesta, P. (Eds.), Genetic algorithms in engineering and computer science. Wiley, Chichester.

Osman, I.H., Laporte, G., 1996. Metaheuristics: A bibliography. Ann Oper Res 63 (5), 511–623. 10.1007/BF02125421.

Rimpault, G., 1995. Algorithmic features of the ECCO Cell Code for treating heterogeneous fast reactor subassemblies, in: Int. Conf. Mathematics and computations, reactor physics, and environmental analyses, Portland, OR, USA. May 1-5, 1995.

Rimpault, G., Grimstone, M.J., 1987. Validation of New Subgroup Algorithms for Resonance Self-Shielding in Heterogeneous Structures, in: Proc. Int. Top. Meet. on Advances in Nuclear Engineering Computation and Radiation Shielding, Santa Fe, NM, USA. April 9-13, 1989.

Rimpault, G., Plisson, D., Tommasi, J., Jacqmin, R., Rieunier, J.M., 2002. The ERANOS code and data system for fast reactor neutronic analyses, in: Proc. Int. Conf. PHYSOR 2002, Seoul. October, 7-10. American Nuclear Society, La Grange Park, Ill.

Rineiski, A., Sinitsa, V., Gabrielli, F., Maschek, W., 2011. C4P Cross-section Libraries for Safety Analyses with SIMMER and related studies, in: Proc. Int. Conf. M&C 2011, Rio de Janeiro, Brazil. May 8-12, 2011. Latin American Section (LAS) / American Nuclear Society (ANS).

Santamarina, A., Collignon, C., Garat, A., 2004. French calculation schemes for light water reactor analysis, in: Proc. Int. Conf. PHYSOR 2004. The physics of fuel cycles and advanced nuclear systems, Chicago, IL, USA. April 25-29, 2004. American Nuclear Society.

Sciora, P., Blanchet, D., Buiron, L., Fontaine, B., Vanier, M., Varaine, F., Venard, C., Massara, S., Scholer, A.-C., Verrier, D., 2011. Low void effect core design applied on 2400 MWth SFR reactor, in: Proc. ICAPP 2011, Nice, France. May 2-5, 2011. American Nuclear Society, pp. 487–495.

Sedgewick, R., Wayne, K.D., 2011. Algorithms, 4th ed. Addison-Wesley, Boston, Mass., London.

Shi, Y., Eberhart, R., Chen, Y., 1999. Implementation of evolutionary fuzzy systems. IEEE Trans. Fuzzy Syst. 7 (2), 109–119. 10.1109/91.755393.

Shibata, K., Iwamoto, O., Nakagawa, T., Iwamoto, N., Ichihara, A., Kunieda, S., Chiba, S., Furutaka, K., Otuka, N., Ohasawa, T., Murata, T., Matsunobu, H., Zukeran, A., Kamada, S., Katakura, J.-i., 2011. JENDL-4.0: A New Library for Nuclear Science and Engineering. Journal of Nuclear Science and Technology 48 (1), 1–30. 10.1080/18811248.2011.9711675.

Siddique, N.H. Intelligent control: A hybrid approach based on fuzzy logic, neural networks and genetic algorithms.

Smith, A.E., Coit, D.W., 1997. Penalty functions, in: Bäck, T., Fogel, D.B., Michalewicz, Z. (Eds.), Handbook of evolutionary computation. Institute of Physics, Bristol, C5.2.

Soppera, N., Bossant, M., Dupont, E., 2014. JANIS 4: An Improved Version of the NEA Java-based Nuclear Data Information System. Nuclear Data Sheets 120, 294–296. 10.1016/j.nds.2014.07.071.

Stacey, W.M., 2001. Nuclear reactor physics. Wiley, New York, Chichester.

Steinbuch Centre for Computing, 2017a. Forschungshochleistungsrechner ForHLR I. https://www.scc.kit.edu/dienste/forhlr1.php.

Steinbuch Centre for Computing, 2017b. InstitutsCluster II. https://www.scc.kit.edu/dienste/ic2.php.

Tobita, Y., Kondo, Sa., Yamano, H., Fujita, S., Morita, K., Maschek, W., Coste, P., Pigny, S., Louvet, J., Cadiou, T., 2002. The Development of SIMMER-III, An Advanced Computer Program for LMFR Safety Analysis, in: Proc. of the IAEA/NEA Technical Meeting on Use of Computational

Fluid Dynamics (CFD) Codes for Safety Analysis of Reactor Systems Including Containment, Pisa, Italy. November 11-14, 2002.

Turing, A.M., 1950. Computing Machinery and Intelligence. Mind LIX (236), 433–460. 10.1093/mind/LIX.236.433.

Varaine, F., Marsault, P., Chenaud Marie-Sophie, Bernardin, B., Conti, A., Sciora, P., Venard, C., Fontaine, B., Devictor, N., Martin, L., Scholer, A.-C., Verrier, D., 2012. Pre-conceptual Design Study of ASTRID Core, in: Proc. ICAPP 2012, Chicago, USA. June 24-28, 2012.

Vasile, A., Fiorini, G.L., Dufour, P., Bonnerot, J.M., Latge, C., Riou, B., Stainsby, R., Rini, M., Verwaerde, D., Struwe, D., Stieglitz, R., Badea, F., 2011a. The collaborative project for a European sodium fast reactor - CP ESFR, in: Proc. ICAPP 2011, Nice, France. May 2-5, 2011. American Nuclear Society.

Vasile, A., Fontaine, B., Vanier, M., Gauthe, P., Pascal, V., Prulhiere, G., Jaecki, P., Martin, L., Tenchine, D., Rochwerger, D., Barret, P., Verwaerde, D., Dupraz, R., 2011b. The Phenix final tests, in: Proc. ICAPP 2011, Nice, France. May 2-5, 2011. American Nuclear Society.

Vezzoni, B., Marchetti, M., Andriolo, L., Gabrielli, F., Chen, X.N., Matzerath Boccaccini, C., Rineiski, A., Maschek, W., Morita, K., Arima, T., 2016a. SIMMER/PARTISN analyses of EBR-II shutdown heat removal tests, in: Proc. Int. Conf. PHYSOR 2016, Sun Valley, ID, USA. May 1-5, 2016, pp. 3973–3982.

Vezzoni, B., Marchetti, M., Gabrielli, F., Rineiski, A., 2016b. IAEA EBR-II neutronics benchmark: Impact of modeling options on KIT results, in: Proc. Int. Conf. PHYSOR 2016, Sun Valley, ID, USA. May 1-5, 2016, pp. 719–728.

Vose, M.D., 1991. A linear algorithm for generating random numbers with a given distribution. IIEEE Trans. Software Eng. 17 (9), 972–975. 10.1109/32.92917.

Voß, S., 2001. Meta-heuristics: The State of the Art, in: Nareyek, A. (Ed.), Local search for planning and scheduling. ECAI 2000 Workshop, Berlin, Germany, August 21, 2000 : revised papers / Alexander Nareyek (ed.), vol. 2148. Springer, Berlin, London, pp. 1–23.

Walker, A.J., 1977. An Efficient Method for Generating Discrete Random Variables with General Distributions. ACM Trans. Math. Softw. 3 (3), 253–256. 10.1145/355744.355749.

Waltar, A.E., Reynolds, A.B., 1981. Fast breeder reactors. Pergamon, New York, Oxford.

Wang, S., Rineiski, A., Maschek, W., 2006. Molten salt related extensions of the SIMMER-III code and its application for a burner reactor. Nuclear Engineering and Design 236 (14-16), 1580–1588. 10.1016/j.nucengdes.2006.04.022.

Wang, S., Rineiski, A., Zhang, D., 2013. Molten salt fast reactor analyses with SIMMER-III. Transactions of the American Nuclear Society 108, 931–932.

Weinberg, A.M., Wigner, E.P., 1958. The physical theory of neutron chain reactors. University Press; London : Cambridge University Press, Chicago.

Won, J.H., Cho, N.Z., 2011. Discrete ordinates method-like transport computation with equivalent group condensation and angle-collapsing for local/global iteration. Annals of Nuclear Energy 38 (4), 846–852. 10.1016/j.anucene.2010.11.012.

Yamano, H., Fujita, S., Tobita, Y., Kamiyama, K., Kondo, Sa., Morita, K., Fischer, E.A., Brear, D.J., Shirakawa, N., Cao, X., Sugaya, M., Mizuno, M., Hosono, S., Kondo, T., Maschek, W., Kiefhaber, E., Buckel, G., Rineiski, A., Flad, M., Suzuki, T., Coste, P., Pigny, S., Louvet, J., Cadiou, T., 2003. SIMMER-III: A Computer Program for LMFR Core Disruptive Accident Analysis. TN9400 2003-071. Japan Nuclear Cycle Development Institute.

Yamano, H., Fujita, S., Tobita, Y., Sato, I., Niwa, H., 2008. Development of a three-dimensional CDA analysis code: SIMMER-IV and its first application to reactor case. Nuclear Engineering and Design 238 (1), 66–73. 10.1016/j.nucengdes.2007.04.015.

Yi, C., Sjoden, G., 2013. Energy group structure determination using particle swarm optimization. Annals of Nuclear Energy 56, 53–56. 10.1016/j.anucene.2012.12.020.

This work was performed on the computational resource ForHLR I funded by the Ministry of Science, Research and the Arts Baden-Württemberg and DFG ("Deutsche Forschungsgemeinschaft".